UNIVERSIDAD COMPLUTENSE DE MADRID

FACULTAD DE CIENCIAS FÍSICAS

DEPARTAMENTO DE FÍSICA DE LA TIERRA Y ASTROFÍSICA

TESIS DOCTORAL

ANÁLISIS DE OLAS DE CALOR DESDE UNA PERSPECTIVA LAGRANGIANA/HEAT WAVE ANALYSIS FROM A LAGRANGIAN PERSPECTIVE

MEMORIA PARA OPTAR AL GRADO DE DOCTOR
PRESENTADA POR:

ANTONIO SÁNCHEZ BENÍTEZ

DIRECTORES:

RICARDO GARCÍA HERRERA

DAVID BARRIOPEDRO CEPERO

Madrid

Agradecimientos (Acnowledgements)

Me dicen unos años atrás que estaría escribiendo estas líneas y me entraría la risa floja, pero la vida da muchas vueltas, tantas que a veces llega a marear. Sin duda hay mucha gente que ha hecho todo esto posible. Posiblemente me deje alguna sin mencionar en estas líneas pero que no dude que se encuentra en mi corazón.

Como no, en primer lugar, agradecer a Ricardo García Herrera por su infinita paciencia conmigo, sin duda, aunque no intencionadamente, no se lo he puesto nada fácil, pero ha sabido sacar lo mejor de mí. Al igual que David Barriopedro Cepero que tantas veces ha aportado sus grandes conocimientos y la confianza que desprende una de las mejores personas que he conocido. Agradecer también por tantas enseñanzas y esas amenas comidas hablando de cualquier cosa al resto de doctores del grupo STREAM: Natalia, Carlos, Álvaro, Marta y Leo. Aquí me dejo a Blanca que, aunque también es doctora, ha sido especialmente importante para mí en estos últimos meses.

Thanks so much Pascal Yiou and all the LSCE staff for the warm host during the best three months of this thesis.

Esta tesis doctoral ha sido financiada con una Ayuda para contratos predoctorales de personal investigador en formación (Convocatoria CT45/15-CT46/15) en el periodo entre el 9 de mayo de 2016 y el 19 de septiembre de 2016 y con una ayuda para la formación de profesorado universitario (Convocatoria FPU2015) entre el 20 de septiembre de 2016 el 31 de diciembre de 2019. Así como la estancia en el Laboratoire des Sciences du Climat et de l'Environnement por una Ayuda a la movilidad para estancias breves y traslados temporales (Convocatoria 2017) del Ministerio de Educación, Formación Profesional y Universidades.

Agradecer también al doctor Pedro Mendes Sousa por proporcionarnos su catálogo de dorsales subtropical que ha sido empleado en algunos capítulos de la tesis.

Merecen una mención aparte mis queridos compañeros de despacho. Sinceramente pienso que no se puede ser más afortunado con los que me han tocado. Primero Maddalen y Froila que me hicieron todo lo agradable que pudieron la primera parte de este viaje y luego cómo no a mis queridos José, Javi Mellado, Fernando, Adrián y Samu. Durante este periodo siempre que os he planteado mis problemas me habéis devuelto una solución, sosteniéndome en los momentos más duros.

Pero como digo esto no es solo cosa de los últimos años, si no que ha habido muchísima gente que ha hecho posible que hoy me encuentre escribiendo esto. Sin duda mi familia siempre ha hecho todo y más para que no me falte de nada, proporcionándome los mejores valores en la vida.

Aunque sin duda gran parte de lo que soy hoy en día la tiene una persona muy especial que fue la que empezó a enderezar mi camino, la seño Manoli. Sin ti esto no hubiera sido posible.

Tampoco me quiero olvidar de alguien, que en paz descanse, que hizo que se despertara la chispa en mí hace ya unos cuantos años.

Algo curioso es que todas mis etapas investigadoras han sido saltos al vacío, hablando con alguien que no conocía que luego ha dado todo por mí. Este trabajo también tiene dos contribuciones que lo han hecho posible. En primer lugar, tengo que dar las gracias a María Dolores Calzada Canalejo por confiar en mí, Rocio Rincón Liévana como mi primera compi de despacho, facilitándome la vida todo lo posible, y sobre todo a José Muñoz Espadero que tan bien me acogieron en mi primera etapa en investigación donde me hicieron ver que este sería mi futuro. Demostrándome que con ambición nunca se es pequeño en este mundo.

El master sin duda fue una época oscura, por lo que afronté con muchas dudas mis dos meses en Zaragoza. Sin embargo, el cálido recibimiento que recibí por parte de Sergio Vicente Serrano y todo el equipo del IPE hicieron estos dos meses un tiempo maravilloso, que me dio fuerza para lanzarme a hacer la tesis. Sinceramente en los dos momentos dude mucho con quién hacer la tesis y sin duda el trabajo hubiera sido excepcional con cualquier decisión.

Por ultimo en el plano académico agradecer lo fácil que me hizo Marisa Montoya mi primera experiencia como docente que tanto me gusto. Así como a todos los integrantes del departamento que tantas facilidades me han dado en todo momento.

Pero no solo de ciencia vive el hombre. Quien me conozca sabe lo importante que es el atletismo en mi vida y que colaborar en la gestión de un club mientras se hace la tesis no es fácil. Sin embargo, también ha sido uno de los principales pilares de desahogo durante la tesis y antes de ella. Aquí fundamentalmente tengo tres pilares: mi gente del atletismo de Córdoba (donde incluyo a mis Califas no cordobeses) y mis dos grupos de entrenamiento madrileños.

Y algo hay que hacer en los fines de semana que no se compite (o en los días de antes/horas de después), por ejemplo, quedar con mis cordobeses madrileños. Pasar el tiempo con mis muchos compañeros de piso y en especial con Nico. O durante mi estancia en la región parisina, muchísimas gracias a esos grandes españoles que encontré por hacer de estos 3 meses una de las mejores etapas de mi vida.

Y algo que he aprendido en la tesis es que hay que cerrar con lo más fuerte que tengas, por eso quiero cerrar con mis amigos de siempre de Córdoba, que han logrado distraer mi mente en los momentos más duros, especialmente esos dos agostos trabajando a tiempo completo.

Gracias a todos y a los, que cómo dije, seguro que me dejo.

Contents

Summary

Introduction

The global mean temperature has increased by ~1ºC since the preindustrial period (Allen et al., 2018). Global warming is spatially and temporally inhomogeneous, with larger increases for land and specific regions (so-called hot-spots) and seasons, such as the summer warming in the Mediterranean (García-Herrera and Barriopedro, 2018). The increasing trend of mean temperatures has been accompanied by changes in the tails of the distribution, including an increase in the frequency/duration and intensity of heat waves (Acero et al., 2018; Chapman et al., 2019) , as well as the occurrence of new emerging events, also called mega-heat waves. These extreme events, cause severe impacts in socio-economic sectors and population, like extensive crop failures (Fahad et al., 2017), devastating wildfires (Parente et al., 2018), poor air quality (Ordóñez et al., 2010; Rasilla et al., 2019), increased mortality (Kovats and Hajat, 2008), and peaks in energy demand (Newsham and Bowker, 2010).

Because of their conspicuous impacts, heat waves are often defined according to the specific target sector (e.g. health-related indices, Díaz et al., 2018). From a meteorological point of view, a commonly accepted heat wave definition is still lacking. All definitions used so far share a common "Eulerian" perspective, whereby heat waves are treated as local phenomena, independent from those occurring in neighbouring regions. This approach emphasizes the local aspect of heat waves and misses the spatial coherence of these events and their links with the atmospheric circulation, which are especially relevant in the case of mega-heat waves.

Objectives

This Thesis presents a novel "Lagrangian" detection algorithm that focuses on the heat wave pattern and its spatio-temporal evolution. As a pioneering application, a catalogue of Iberian heat wave events and their characteristics is provided, using reanalysis data for the 1979-2017 period. The versatility of the algorithm, and its ability to characterize European mega-heat waves is also explored, using the June 2017 event as a case study. The resulting catalogues allow us to address the following open questions:

1. ¿Which are the main characteristics of Iberian heat waves?
2. Can Iberian heat waves be classified in regional events with distinctive spatial signatures and characteristics?
3. Which are the dominant atmospheric circulation conditions associated with Iberian heat waves through their life-cycle?
4. How have recent changes contributed to the characteristics of Iberian heat waves?
5. Is the algorithm suitable to diagnose mega-heat waves? Can their outstanding impacts be attributed to thermodynamical and dynamical changes?

Results

These questions build upon the design of a new “Lagragian” heat wave detection algorithm, which can be applied to any region and climate realm. It identifies spatially coherent daily heat wave patterns on synoptic scales and their spatio-temporal evolution, using percentiles of the local temperature distribution only, as well as additional criteria for spatial extension and temporal persistence. The algorithm provides a full description of heat wave events and their characteristics (i.e. areal extent, location, intensity, persistence) through the entire life-cycle, as well as daily maps with the associated heat wave patterns. The results inferred from the derived catalogues of Iberian heat waves and European mega-heat waves are robust to changes in the adopted thresholds, reanalysis product and its horizontal resolution, and can be summarized as follows:

1. For the extended summers (June-to-September) of the 1979-2017 period, a mean frequency of five Iberian heat wave events is reported, which means 16 summer days with heat wave conditions over Iberia. The analysis of the life-cycle reveals that more than half of the heat wave events correspond to events that originated over Iberia. Although Iberian heat wave events last more than one week on average, they tend to be transient, persisting for about three days over Iberia (Iberian phase), where they reach maximum intensity and extension, and evolving later to other areas.

2. Four recurrent types of regional Iberian events have been identified from a clustering analysis of the mean anomalous temperature fields. They are referred to as Atlantic, Subtropical, European and Mediterranean events and display distinctive regional signatures, with heat wave conditions affecting western, southern, northern and eastern Iberia, respectively. These regional events also show some differences in their characteristics and spatio-temporal evolution. For example, subtropical events display the largest areal extent, although European events are those with the largest affected area over Iberia, on average. Differently, Mediterranean heat waves are the most transient, smallest and weakest regional events of all groups.
3. During the Iberian phase, heat wave events are preferentially associated with a weather regime characterized by positive geopotential height anomalies over western Europe. Small variations in this weather regime determine the different types of regional events. However, the four types of regional heat waves tend to occur under different weather regimes during their pre- and post-Iberian phases, and show different relationships with weather regimes on seasonal scales.
4. Significant positive trends are found for Iberian heat wave events and days in all summer months (exception made for September), with the largest trends occurring in early (June) and high (August) summer. Mediterranean events largely explain the overall Iberian trends, although the most outstanding Iberian heat waves are preferably Atlantic or European, including the recent episode of June 2017. An analysis of flow analogues for the most outstanding events reveal that the warming of the last decades has contributed to double their extension and intensity, making them more exceptional than they would have been in the past.
5. A more detailed assessment of the June 2017 event demonstrates the good performance of the algorithm to diagnose European mega-heat waves. Its extension, intensity and persistence were comparable to those of other European mega-heat waves but it occurred earlier in the summer. A record-breaking subtropical ridge with signatures closer to those of July and August, was responsible of the unprecedented warm air intrusion over Iberia. Thermodynamical changes of the last decades made a substantial contribution to the event, by increasing the likelihood of surpassing high-temperature thresholds. Nevertheless, dynamical changes are not negligible, and increase the odd of occurrence of moderately warm temperature anomalies.

Resumen

Introducción

La temperatura media global ha aumentado ~1ºC desde la época preindustrial (Allen et al., 2018). Este calentamiento es desigual en el espacio y en el tiempo, con un mayor aumento sobre tierra y en determinadas regiones (llamadas “puntos calientes”) y estaciones de año, como en el Mediterráneo en verano (García-Herrera and Barriopedro, 2018). El aumento de la temperatura media ha venido acompañado por cambios en las colas de la distribución, provocando un incremento en la frecuencia, duración e intensidad de las olas de calor (Acero et al., 2018; Chapman et al., 2019), así como en la ocurrencia de nuevos eventos conocidos como mega-olas de calor. Éstas conllevan grandes impactos socio-económicos como pérdidas de cosechas (Fahad et al., 2017), incendios forestales (Parente et al., 2018), baja calidad del aire (Ordóñez et al., 2010; Rasilla et al., 2019), aumentos en mortalidad (Kovats and Hajat, 2008) o picos en la demanda eléctrica (Newsham and Bowker, 2010).

Existen numerosas definiciones de ola de calor, en función del sector afectado (p. ej. impactos en salud, Díaz et al., 2018). Desde un punto de vista meteorológico no existe una definición comúnmente aceptada, pero todas ellas emplean una perspectiva “euleriana”, en la que las olas de calor se estudian punto a punto y por tanto de forma independiente, sin tener en cuenta las condiciones en regiones contiguas. Esta aproximación no tiene en cuenta la coherencia espacial de los eventos y dificulta el estudio de sus relaciones con la circulación atmosférica.

Objetivos

Esta Tesis presenta un nuevo algoritmo de detección “lagrangiano” que se centra en el patrón espacial de ola de calor y su evolución espacio-temporal. Como aplicación pionera, se ha obtenido un catálogo de olas de calor en Iberia usando datos de reanálisis para el periodo 1979-2017. También se ha explorado la capacidad del algoritmo para caracterizar mega-olas de calor europeas, usando el evento de junio de 2017 como un caso de estudio. Estos catálogos permiten abordar las siguientes preguntas:

1. ¿Cuáles son las principales características de las olas de calor ibéricas?
2. ¿Pueden distinguirse eventos regionales con impactos y características diferenciadas?
3. ¿Cuáles son las condiciones sinópticas dominantes asociadas con la ocurrencia de olas de calor en Iberia a lo largo de su ciclo de vida?
4. ¿Cómo han contribuido los cambios recientes a las características de las olas de calor en Iberia?
5. ¿El algoritmo permite diagnosticar mega-olas de calor? ¿Pueden atribuirse sus impactos a cambios termodinámicos y dinámicos?

Resultados

Estas preguntas se analizan con un nuevo algoritmo de detección de olas de calor, que puede ser aplicado a cualquier región y climatología. Éste identifica patrones espaciales a escala sinóptica con condiciones simultáneas de ola de calor, así como su evolución espacio-temporal. Para ello, se usan percentiles de la distribución de temperatura local, con criterios adicionales para la extensión espacial y persistencia. El algoritmo proporciona una descripción completa de los eventos y sus características (extensión espacial, localización, intensidad, persistencia) a lo largo del ciclo de vida, así como mapas diarios con los patrones de ola de calor asociados. Los resultados de esta Tesis son robustos respecto a cambios en los umbrales adoptados, el producto de reanálisis y su resolución horizontal, y pueden resumirse como sigue:

1. Para el periodo 1979-2017, la frecuencia media de olas de calor en Iberia durante el verano extendido (junio-septiembre) es de cinco episodios, lo que equivale a un promedio de 16 días de ola de calor. El análisis de su ciclo de vida revela que más de la mitad de los eventos se genera en la Península ibérica. Aunque en media duran más de una semana, tienden a desplazarse durante su ciclo de vida, afectando a Iberia solo tres días (fase ibérica), donde alcanzan su máxima intensidad y extensión, y evolucionando después a otras zonas.
2. A partir del patrón medio de anomalías de temperatura se han identificado cuatro tipos de eventos regionales: atlánticos, subtropicales, europeos y mediterráneos. Estos muestran impactos regionales diferenciados, afectando al oeste, sur, norte y este de Iberia, respectivamente, así como características específicas. Por ejemplo,

los eventos subtropicales son los de mayor extensión espacial, si bien son los eventos europeos los que afectan a una mayor parte de Iberia. Por otro lado, los eventos mediterráneos se caracterizan por su menor estacionareidad, extensión e intensidad.

3. Durante su fase ibérica, las olas de calor se asocian con un mismo tipo de tiempo, caracterizado por anomalías positivas de altura geopotencial sobre el oeste de Europa. Pequeñas diferencias en la localización de este patrón determinan los distintos tipos de evento regional. Sin embargo, los cuatro grupos tienden a ocurrir bajo distintos tipos de tiempo durante sus fases pre- y post-ibérica, y muestran diferentes relaciones con los tipos de tiempo a escala estacional.
4. Se han encontrado tendencias significativas en la frecuencia de eventos y días de ola de calor en Iberia para todos los meses, excepto septiembre. Las mayores tendencias se detectan al inicio (junio) y mitad (agosto) del verano. Los eventos mediterráneos explican gran parte de las tendencias de Iberia, aunque las olas de calor de mayor impacto suelen ser atlánticas o europeas, incluyendo el reciente episodio de junio de 2017. Un análisis de análogos de circulación revela que el calentamiento de las últimas décadas ha contribuido a doblar la extensión e intensidad de los eventos de mayor impacto, haciéndolos más excepcionales de lo que hubieran sido en el pasado.
5. Un análisis detallado de la ola de calor de junio de 2017 confirma la capacidad del algoritmo para diagnosticar mega-olas de calor. Su extensión, intensidad y persistencia fueron comparables a las de otras mega-olas de calor europeas, pero fue más temprana. Una dorsal subtropical récord, con características más parecidas a las de julio y agosto, fue responsable de una intrusión de aire cálido sin precedentes. Los cambios termodinámicos de las últimas décadas han contribuido a exacerbar la intensidad del evento, aumentando la probabilidad de ocurrencia de temperaturas extremadamente elevadas. Sin embargo, los cambios dinámicos no son despreciables, y han aumentado la probabilidad en el rango de temperaturas cálidas moderadas.

1. Introduction

1.1. Meteorological heat waves: indices and definitions

Heat waves (HWs afterwards) are extreme events of major concern due to their dramatic consequences in numerous sectors. They are associated, among others, with extensive crop failures (Fahad et al., 2017; Lesk et al., 2016) and devastating wildfires (Gouveia et al., 2016; Hodzic et al., 2007; Parente et al., 2018). These events are also important for human health and wellbeing since, combined with poor air quality (Konovalov et al., 2011; Ordóñez et al., 2010; Rasilla et al., 2019; Vautard et al., 2005), they can lead to increased mortality (Garcia-Herrera et al., 2010; Haines et al., 2006; Kovats and Hajat, 2008), especially in the elderly people (Fouillet et al., 2006). However, in the last years, the efficient implementation of early warning systems (Carmona et al., 2017) and the increase in the use of air conditioning (Kalvelage et al., 2014) have decreased the exposure and hence fatalities (Díaz et al., 2018; Toloo et al., 2013). Consequently, an increase in energy demand during HWs (Newsham and Bowker, 2010) has been reported.

Among HWs there are some new emerging events, typically called mega-heat waves (Bador et al., 2017; Barriopedro et al., 2011; Fischer, 2014; Miralles et al., 2014) which stand out due to their large spatial extension, intensity and persistence, causing extensive impacts over large areas. In Europe the most documented events are the August 2003 event that mostly affected western Europe (e.g. Bador et al., 2017; Garcia-Herrera et al., 2010; Trigo et al., 2005) causing 70,000 heat-related fatalities and US$10 billions of economic losses, and the July-August 2010 episode of eastern Europe and Russia (e.g. Barriopedro et al., 2011; Dole et al., 2011; Grumm, 2011; Russo et al., 2015) with similar impacts (50,000 fatalities and US$15 billions). In the rest of the world some outstanding events have also occurred, for example the July 2018 mega-heat wave in Japan (Imada et al., 2019) or the May-June 2015 mega-heat wave in India (Ratnam et al., 2016), with 1,032 and 2,248 deaths, respectively.

As consequence of these conspicuous impacts in society, the study of HWs is one of the main research topics in climate sciences. Nevertheless, from a meteorological point of view, there is not a homogenously-used HW definition. The World Meteorological Organization (WMO) defines a HW event as "a marked warming of the air, or the invasion of very warm air, over a large area; it usually lasts from a few days to a few weeks" (WMO, 1992). This definition seems ambiguous as it illustrates the HW social perception and disregards objective criteria on temperature, extension or duration. On the other hand, the Intergovernmental Panel on Climate Change (IPCC) also provides a vague HW definition: "A period of abnormally and uncomfortably hot weather" (IPCC, 2013). As consequence of this ambiguity, there are different HW definitions depending on the author, the study area and the scope of the study. As there is not a universally accepted HW definition, there are not generally accepted thresholds to consider a HW as a mega-heat wave. Based on the characteristics of these events, Barriopedro et al. (2011) defined mega-heat waves as regional ($\geq$1,000,000 km^2) mean temperature anomalies of extraordinary amplitude ($\geq$3 standard deviations) at subseasonal scales ($\geq$ 7 days)

The most employed HW definitions come from the Expert Team on Climate Change Detection and Indices (ETCCDI) from the World Climate Research Programme (WCRP). They define a set of indices to examine hot spells: SU (TR) counts the number of days whose maximum (minimum) temperature exceeds 25 ºC (20 ºC); TX90p (TN90p) accumulates the number of daily exceedances of the local 90th percentile of maximum (minimum) temperature. The WSDI is similar to TX90p, but only accounts for spells of at least 6 consecutive days. Finally, TXx (TNx) only considers the highest daily maximum (minimum) temperature of the month.

In addition to these indices, some authors use their own HW definitions (Table 1.1). The main differences among them are:

- The target variable: daily maximum, mean or minimum temperature, or a combination of them are utilized. For example, Russo et al., 2015 introduce the Heat Wave Magnitude Index daily (HWMId) to take into account the accumulated amplitude and persistence of local HWs during each summer.
- The temperature threshold. Some studies employ a constant value for the entire domain. Nevertheless, most definitions utilize values based on a percentile (from 80th to 95th) of the local temperature distribution of each grid point. These percentile-based definitions provide a threshold adapted to the different climatologies.

- Within the percentile-based definitions there are also discrepancies in the calendar period used to compute the threshold. Some of them use time invariant thresholds derived from a fixed calendar period (e.g. July and August in the AEMET, 2018 definition). Consequently, the HW frequency would be higher (lower) in the hotter (colder) subperiods. To avoid this, other definitions use time-varying thresholds by means of moving windows of up to 31-day width, centred at each calendar day. Therefore, the threshold accommodates to the seasonal cycle, which allows to study hot periods throughout the year (typically called "hot spells" when they are detected outside the extended summer).
- The reference period (climatological baseline) to compute the temperature threshold also varies. Studies use either a 30-year period (following the WMO standards, i.e. 1961-1990, 1971-2000 or 1981-2010) or the full available period of the dataset. The use of different temporal periods leads to changes in the percentile values. These differences are highlighted in Figure 1.1, which represents the difference between the 95th local percentiles of the temperature at 850 hPa (T850) for 1971-2000 and 1981-2010 periods (This pressure level is selected as it is less affected by local processes like orography or sea-atmosphere contrast than the surface, see section 3.2 for more details). An increase of up to ~0.7ºC is observed in the Mediterranean. Therefore, in this region the 95th percentile for the 1971-2000 period is equivalent to the 92th-93th percentile of the 1981-2010 period (Figure 1.2)
- The duration threshold to consider a hot period as a HW, which ranges from two to six days.

All definitions shown in Table 1.1 share a common issue. They study HWs from a local perspective, checking for each point separately if the conditions of HW events (HWEs hereafter) are satisfied (which, by analogy with the fluid mechanics, can be considered as an Eulerian description). Hence the events detected in a given point are treated separately (and somehow assumed independent) from those occurring in neighbour areas. For example, the August 2003 HW affected different regions at different times, following the evolution of the anomalous synoptic scale atmospheric circulation (Figure 1.3 a-c). As such, the list of local HW events derived from the classical Eulerian description would be erroneously diagnosed as different and apparently unconnected warm spells (Figure 1.3, panel d). Therefore, this description misses the spatial coherence and structure of HWs, leading to a HW misperception.

Authors	Temperature index	Temperature threshold	Temporal window	Reference period	Duration threshold (days)
AEMET, 2018	Maximum	Percentile 95	July and August	1971-2000	3
Anderson and Bell, 2011	Mean	Percentile 95	Warm season	1987-2005	2
Della-Marta et al., 2007	Maximum	Percentile 80	5 days	1906-2003	3
Fischer and Schär, 2010	Maximum	Percentile 90	15 days	1961-1990	6
Huth et al., 2000	Maximum	30 ºC	None	None	3
Mishra et al., 2017	Maximum	Percentile 90	31 days	1971-2000	3
Pezza et al., 2012	Maximum and Minimum	Percentile 90	Month	1979-2008	3
Russo et al., 2015	Maximum	Percentile 90	31 days	1981-2010	3
Stefanon et al., 2012	Maximum	Percentile 95	21 days	1950-2009	4
Steul et al., 2018	Maximum	32 ºC	None	None	5
Tomcyzk et al., 2017	Maximum	Percentile 95	Annual	Non-defined	5
Unkašević and Tošić, 2009	Maximum	Mean temperature+5ºC	Daily	1961-1990	5

Table 1.1 Main characteristics of some HW definitions.

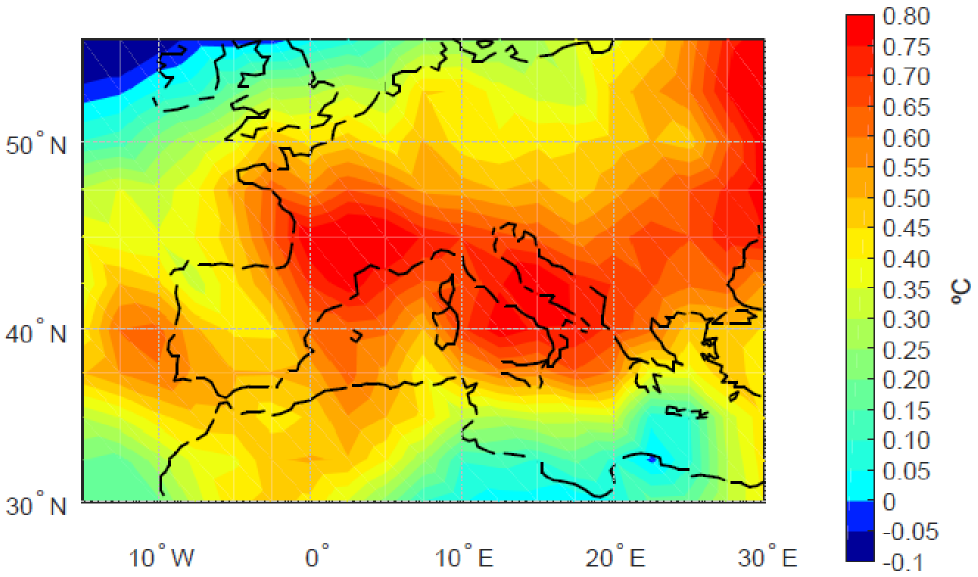

Figure 1.1. Differences of the 95th percentile of T850 for the 1981-2010 and 1971-2000 periods. Data were extracted from ERA-Interim reanalysis (see further details in section 2.1).

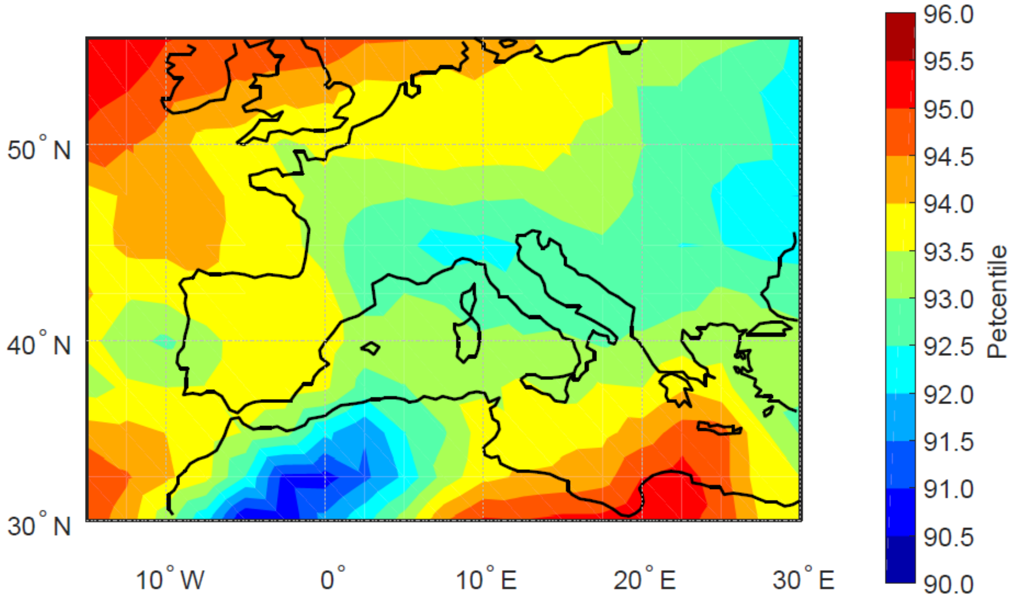

Figure 1.2. Equivalence of the 95th T850 percentile for the 1971-2000 period to the percentile of the 1981-2010 period. Data were extracted from NCEP/NCAR reanalysis (see further details in section 2.1).

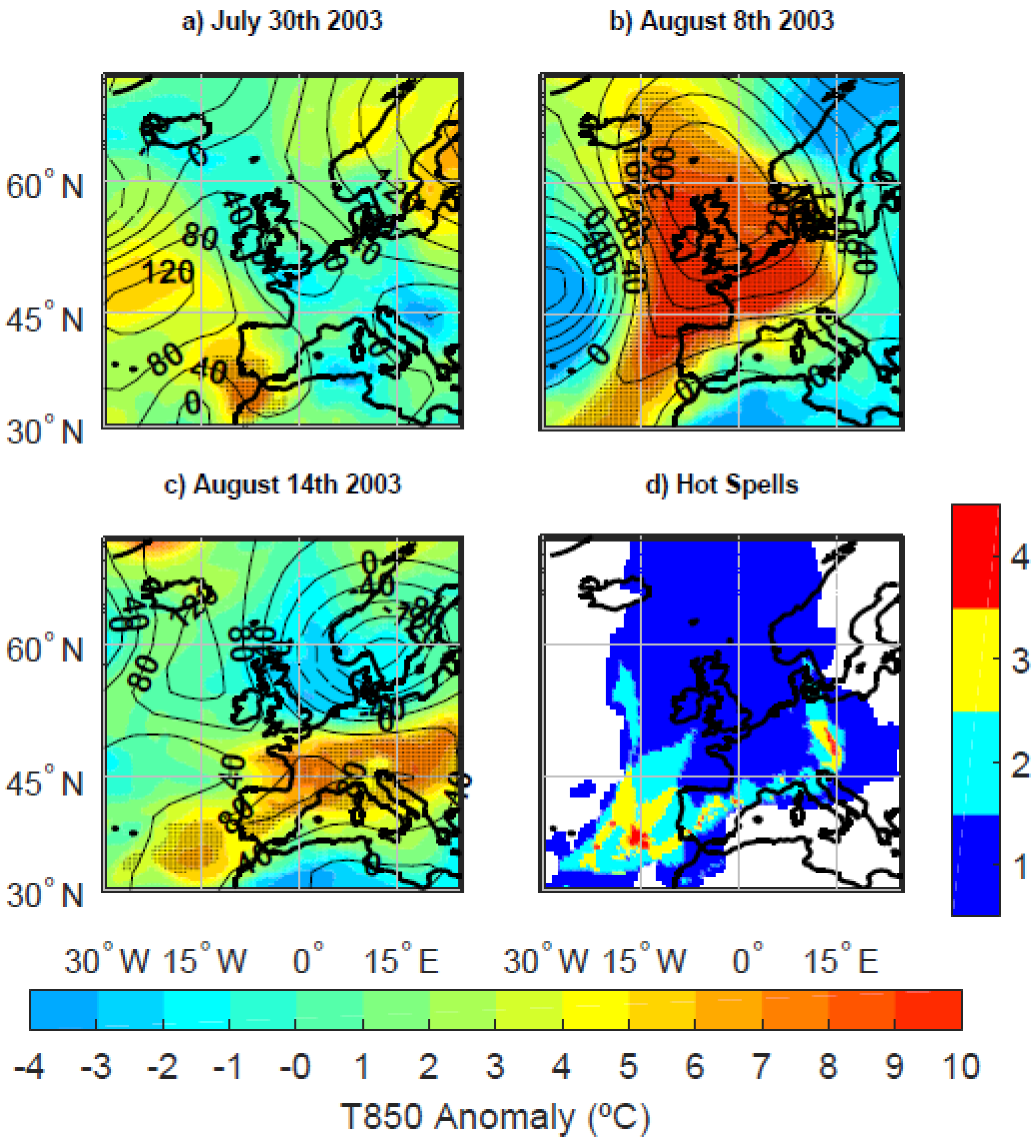

Figure 1.3. a-c) Temperature (shading, in ºC), and Z500 (contours, in m) anomalies for snapshots of the August 2003 HWE. Grid points under local HW conditions are shown with dots; d) Number of hot spells (i.e. HW periods separated by at least one non-HW day) in each grid point for the July-August 2003 HWE. Data were extracted from NCEP/NCAR reanalysis.

1.2. Trends in Mediterranean heat waves: Iberian Peninsula

The HW occurrence is conditioned by the ongoing global warming. For the last decade, the average global temperature is ~1ºC higher than in the pre-industrial period (Allen et al., 2018), with a faster warming rate since the mid-1970 (~0.2ºC decade^{-1}). Human influence on climate has been the dominant cause of the observed warming since the mid-20th century (Allen et al., 2018) with the natural forcings (i.e. due to changes in solar and volcanic activity) with a negligible impact in this period. This anthropogenic warming is due to greenhouse gases (GHG) emissions since the pre-industrial era (IPCC, 2014) as they have led to large increases in the atmospheric concentrations of carbon dioxide (CO_2), methane (CH_4) and nitrous oxide (N_2O) (IPCC, 2014). This upward trend was reinforced in the mid-1970s, when the highest temperature trend is also found, with dramatic consequences: shifting rainfall patterns (Putnam and Broecker, 2017; Trenberth, 2011), which affect the hydrological cycle and water availability (Dayon et al., 2018; Haddeland et al., 2014; Schewe et al., 2014); changes in plants productivity (Tito et al., 2018); ocean acidification (Gaylord et al., 2015; Hoegh-Guldberg et al., 2007; Sunday et al., 2017); destabilization of coastal ice sheets (Hulbe, 2017; Willis et al., 2018); sea level rise (Meehl and Tebaldi, 2004; Nerem et al., 2018); and the increase of extreme events such as droughts (Naumann et al., 2018; Samaniego et al., 2018), heavy precipitation events (Allan and Soden, 2008; Fischer and Knutti, 2015) and heat waves (Meehl and Tebaldi, 2004; Perkins-Kirkpatrick et al., 2016). As a consequence of the observed temperature trends, HWs are becoming more frequent, intense, and longer (Acero et al., 2018; Barriopedro et al., 2011; Chapman et al., 2019; Meehl and Tebaldi, 2004; Russo et al., 2015; Schoetter et al., 2015), and these trends are expected to continue in the future (Dosio et al., 2018; IPCC, 2012; Perkins-Kirkpatrick and Gibson, 2017).

Global warming is not spatially homogenous. The largest temperature change is found over land, where it is higher than 1.5 ºC relative to the preindustrial period, and is more notorious for different vulnerable areas as the Arctic or the Mediterranean, where warming trends exceed the average over land (e.g. Diffenbaugh et al., 2007; Diffenbaugh and Giorgi, 2012; García-Herrera and Barriopedro, 2018). In particular, the Mediterranean is located in a transition area between the tropics and mid-latitudes and therefore is affected by the synoptic systems that are characteristic of both regions. Thus, small changes in the Atlantic storm track or the Hadley cell may cause a large impact in regional climates that are strongly affected by them, such as the Iberian Peninsula (CLIVAR, 2017). The mean Iberian T850 trend for the extended summer (June 1st to September 30th) and the 1979-2017 period is 0.24ºC decade^{-1} ($p<0.05$, Figure 1.4, top panel). Nevertheless, this warming is not homogeneous through the summer months, being only significant for June (0.5ºC decade^{-1}, $p<0.01$, Figure 1.4, middle left panel). These trends have triggered a change in the seasonal cycle. In fact, an earlier onset of the summer season in Europe and specially western Europe has been reported in observations (ranging between -5 to -10 days decade^{-1} from 1979 to 2012; Peña-Ortiz et al., 2015). This trend is largely due to increasing greenhouse gases concentrations (Park et al., 2018) and it is expected to continue in the future (Cassou and Cattiaux, 2016). This would involve an extension of mega-heat waves occurrence towards unusual dates, when compared to the historical record. Morabito et al., (2017) have already found a significant ($p<0.05$) advance in the timing of these events for the recent past.

Figure 1.5 shows the daily evolution of the Iberian mean T850 over the extended summer for two subperiods (1948-1978 and 1979-2017, hereafter referred to as the recent past and present respectively). There is a pronounced intraseasonal variability, with an increase from 12ºC in early June to 18ºC in late July/early August, and a faster decay afterwards. When both subperiods are compared, a change in the seasonal cycle can be observed. The temperature differences tend to be lower in late summer, in agreement with Figure 1.4, and increase in early-mid summer (~1.5ºC warmer in the present than in the recent past).

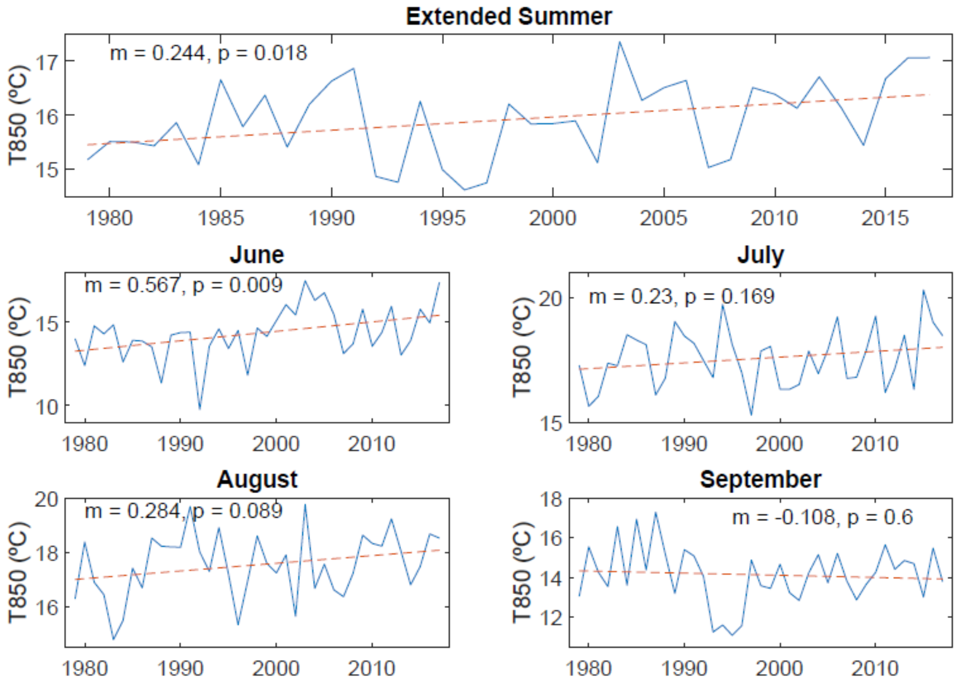

Figure 1.4. Time series of Iberian mean T850 for 1979-2017 and: (top) the extended summer, (middle left) June, (middle right) July, (bottom left) August, (bottom right) September. Data were extracted from ERA-Interim reanalysis (see further details in section 2.1).

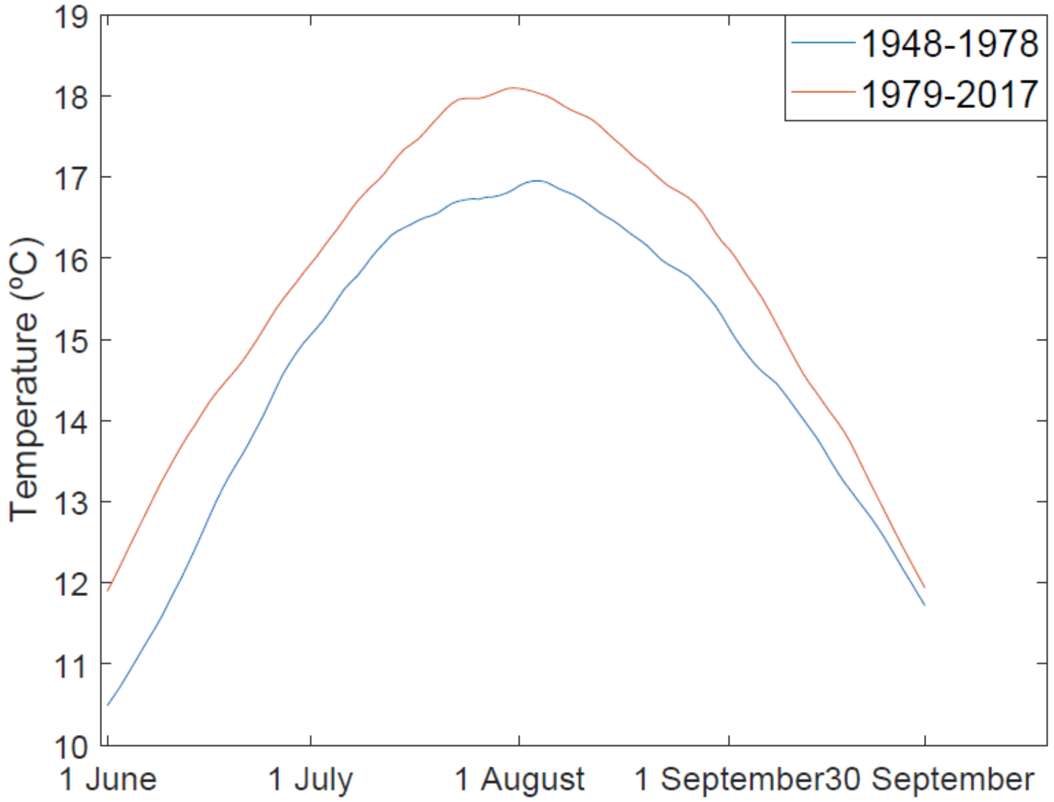

Figure 1.5. Seasonal cycle of Iberian mean T850 for the extended summer and two subperiods (1948-1978 in blue and 1979-2017 in red). A 31-day smoothing is applied. Data were extracted from NCEP/NCAR reanalysis (see further details in section 2.1).

The spatial distribution of the summer T850 trend also reveals large diversity across Iberia (Figure 1.6, top panel) There are positive non-significant trends in northwestern Iberia and significant positive trends ($p<0.05$) in southern and eastern Iberia, where trends are locally higher than 0.5ºC decade^{-1}. They change through the season, following the seasonal march of the trends for the Iberian mean T850 (Figure 1.5): the highest and most extensive warming ($p<0.05$) is found in June (Figure 1.6, middle left panel), with values higher than 0.6ºC decade^{-1} in the central eastern area. Warming trends are smaller for July and August (Figure 1.7 middle right and bottom left panels respectively) and are only significant ($p<0.05$) in the southern area. Meanwhile September trends (Figure 1.6 bottom right panel) are negative (non-significant) in most of Iberia.

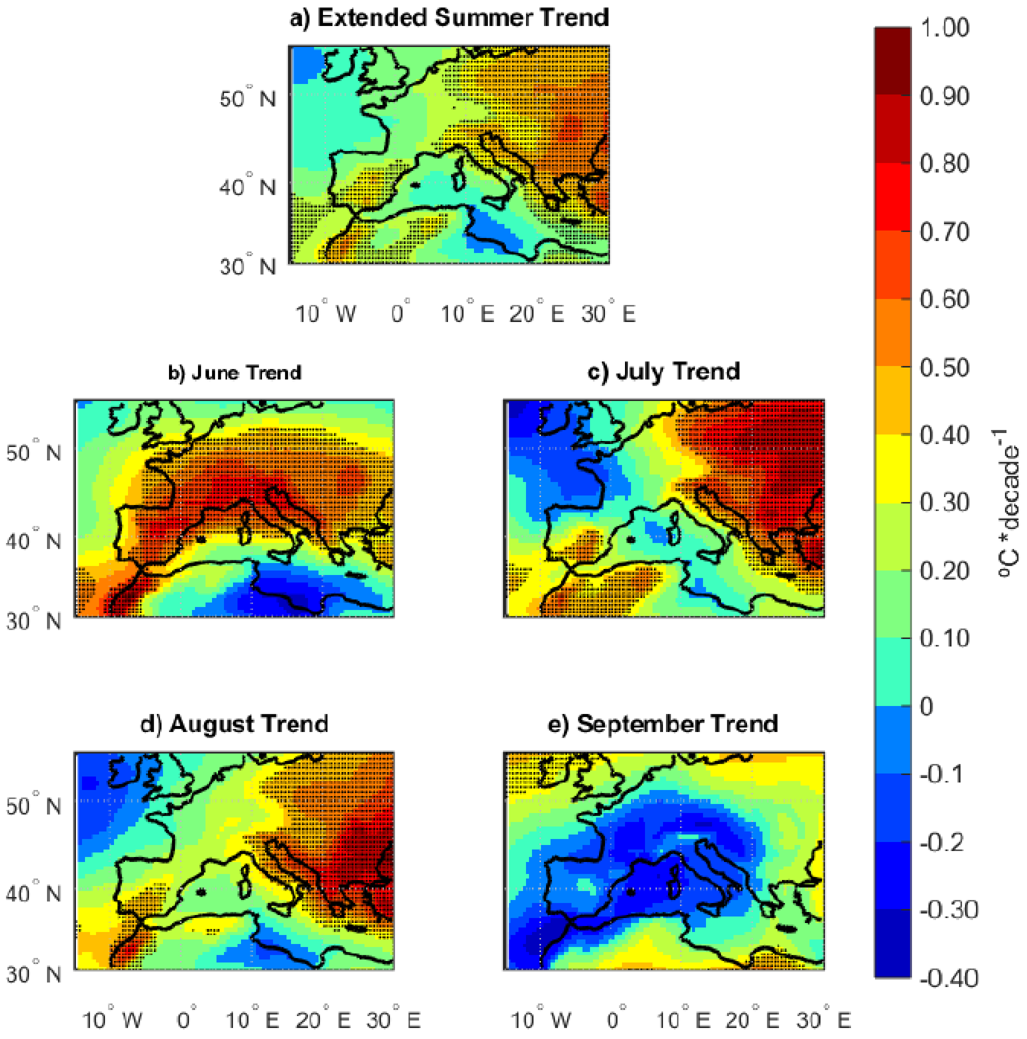

Figure 1.6. T850 trends for the extended summer (top panel); June (middle left); July (middle right); August (bottom left); September (bottom right). Dots indicate where trends are significant at $p<0.05$. See section 2.2.1 for more details of how these trends and their significance are computed. Data were extracted from ERA-Interim reanalysis (see further details in section 2.1).

Previous studies on Iberian HWs have mostly focused on trends in observed or simulated extreme temperature indices at local scales following different Eulerian-based definitions For example, Rodríguez-Puebla et al., (2010) found that the Iberian trend in warm days (defined as TX90p) is significantly higher (1.6% ± 0.3 days decade^{-1}) than the global trend (0.71% ± 0.35 days decade^{-1}). Ramos et al., (2011) reported a significant increase in HW days (HWDs afterward) in numerous weather stations of Portugal using different ETCCDI definitions. Tomczyk et al., (2017) also found a significant increasing trend in HWDs for 72 % of the stations of western and southwestern Europe. Changes in other relevant HW parameters remain less explored. In this sense, a recent study reported significant ($p<0.01$) decreases of HW intensity in Madrid from 1980-1997 to 1998-2015, as well as non-significant changes in HWDs, HW duration or both for Lisbon (Morabito et al., (2017)). Therefore, there are changes in some HW characteristics that are not so obvious and remain more controversial. In addition, none of these works have addressed the climatological characteristics and morphology of synoptic HWs.

On the other hand, and in the context of the ongoing climate change, recent studies have also focused on attributing the occurrence and/or intensity of recent HWs to anthropogenic forcings. However, the detection/attribution mainly concerned thermodynamic aspects of climate change, with dynamical changes remaining more controversial (Shepherd, 2016). In addition, there are no detection / attribution exercises focusing on the characteristics of the HW itself (spatial extension, persistence, etc.), which would allow a simpler interpretation of the dynamical influence.

1.3. Atmospheric circulation associated with Mediterranean heat waves

Many studies have stressed the important contribution of land-atmosphere feedbacks during dry periods (Miralles et al., 2019 and references therein) or sea surface temperature (SST) anomalies (Della-Marta et al., 2007; Duchez et al., 2016; Perkins, 2015) to HW occurrence or intensification. However, there are no many studies addressing the role of the dynamics. Recent efforts have been made to quantify the dynamical influence in HW development. Using the analogue method (Yiou et al., 2014) (Yiou et al., 2014), Jézéquel et al. (2018) found that in most cases dynamics is the main contributing factor to the monthly temperature anomaly recorded during recent mega-heat waves, with the only exception of August 2003. However, in this study the monthly temperature anomalies were reconstructed over a fixed domain. Nevertheless, the August 2003 HWE ended by the mid of the month and affected different areas during its life-cycle (Figure 1.3). Consequently, the assessment of the dynamical contribution was not restricted to the timing and regions under HW conditions.

According to previous works, the atmospheric circulation during HWs is typically characterized by anomalous high pressure systems (Álvarez-Castro et al., 2018; Sousa et al., 2018). To characterize the atmospheric circulation, the most employed variables are the Sea Level Pressure (hereafter, SLP) and the geopotential height at 500 hPa (Z500 afterwards) (Bador et al., 2017; Cassano et al., 2017; Della-Marta et al., 2007; Jézéquel et al., 2018). In some areas like Iberia the enhanced land warming in summer promotes the convective elevation of warm air masses and induces a surface-level baroclinic depression, typically called thermal low (Hoinka and De Castro, 2003). Therefore, SLP is not the best option to diagnose the atmospheric circulation associated with Iberian HWs.

Two main synoptic patterns have been related to European HWs: blocking and subtropical ridges (Figure 1.7). According to Sousa et al., (2018), the most relevant weather system for HWs depends on the considered area. Blockings are high-latitude, persistent (more than 5 days) and slow-moving positive Z500 anomalies that interrupt the westerly jet stream (Barriopedro et al., 2006; Pfahl, 2014). These systems often display a reversal of the meridional Z500 gradient around the typical latitudes of the extra-tropical jet stream (~50ºN) and have been associated with European HWs in summer (Álvarez-Castro et al., 2018; Dong et al., 2018; Schaller et al., 2018; Sousa et al., 2018). However, recent studies (Garcia-Herrera et al., 2010; Sousa et al., 2018) have pointed to a certain overstatement when attributing southern European HWs to blocking. Indeed, blocking is associated with colder than average conditions in this area (Figure 1.8). Different to blocking, subtropical ridges represent relatively narrow extensions of the subtropical belt towards mid latitudes. In addition, they tend to be more transient than blockings, often moving eastward with the mean flow. Unlike blockings, subtropical ridges do not tend to reverse the zonal flow, and so the horizontal advection associated with the warm intrusion is associated with warming in mid-latitudes (Figure 1.8). Therefore, they tend to be an important factor for the occurrence of HWs in southern Europe (e.g. the June 2019 HW, Sousa et al., 2019).

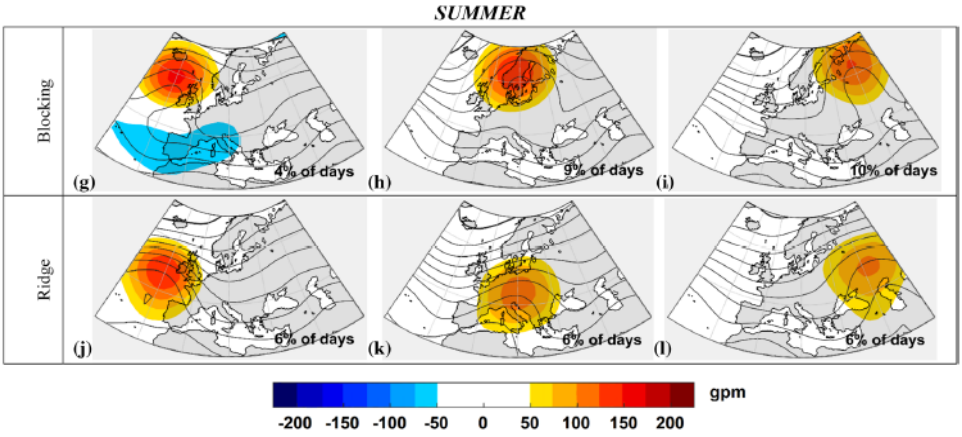

Figure 1.7. Composites of the daily anomalies (shading) and absolute values (contours) of the 500 hPa geopotential height for blocking centres and ridges in each sector during summer. All values are in gpm and the tick line represents the 5500 isohypse (the thinner contours are separated by 50 gpm). The seasonal occurrence for each regime is shown in percentage. Figure extracted from (Sousa et al., 2018).

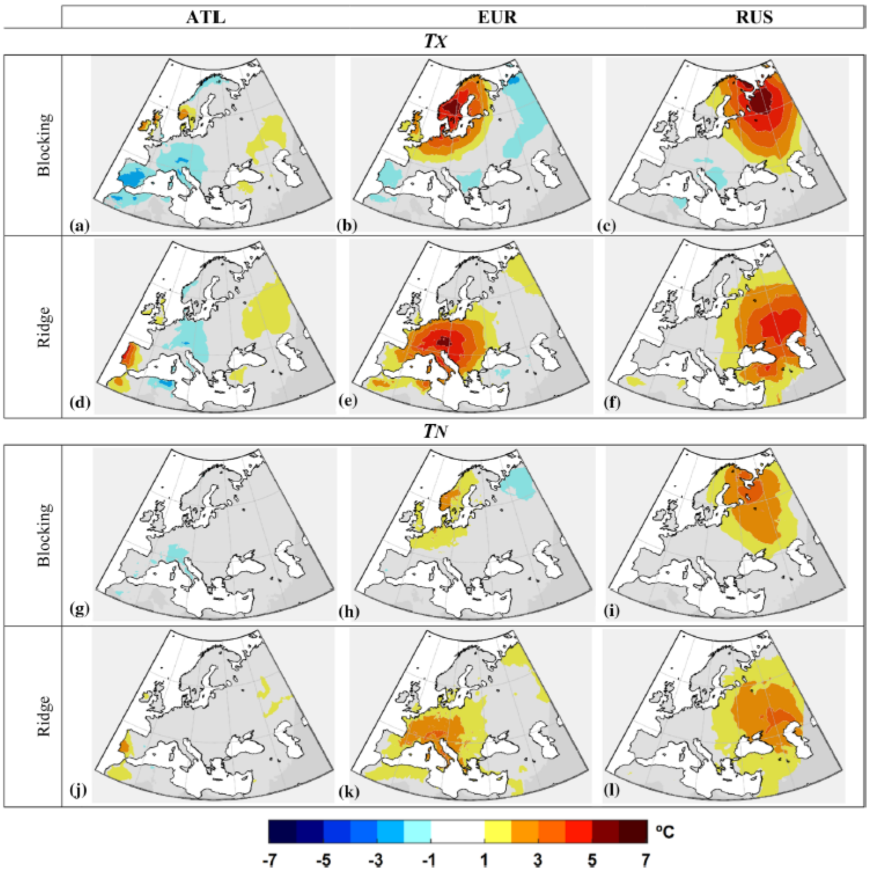

Figure 1.8. Composites for blocking and ridge days occurring in each sector (ATL, EUR and RUS) of summer 2 m above ground maximum (panels a-f) and minimum temperature (panels g-i) anomalies (in ºC). Only statically significant anomalies at 5% significance level are depicted. Figure extracted from (Sousa et al., 2018).

Attending to the temperature tendency equation, there are three processes whereby the atmospheric circulation can induce warming trends and exceed the temperature threshold adopted for the HW definition. Their relative contributions have recently been assessed for blocking and subtropical ridges (Sousa et al. 2018), as well as for specific HWEs (Sousa et al. 2019):

a) Horizontal advection. The horizontal wind induces a temperature advection in the presence of latitudinal and longitudinal temperature gradients. Consequently, the temperature rate at a given point with coordinates (λ, ϕ) that can be ascribed to the horizontal wind ($\vec{v}$) action is given by:

$$\left(\frac{\Delta T}{\Delta t}\right)_h (\lambda, \phi, t) = -\vec{v} \cdot \nabla_p T \qquad (1)$$

where $\left(\frac{\Delta T}{\Delta t}\right)_h$ is the temperature advection by the horizontal wind. This term acquires particular relevance for Iberian HWs under atmospheric conditions associated with a strong meridional circulation that promotes warm air intrusions from northern Africa (e.g. subtropical ridges). The June 2019 HW event (Sousa et al., 2019) is a good example.

b) Vertical advection. Vertical movements can also bring hotter or colder conditions to one point according to the equation:

$$\left(\frac{\Delta T}{\Delta t}\right)_v (\lambda, \phi, t) = -\omega \frac{T}{\theta} \frac{\partial \theta}{\partial p} \qquad (2)$$

where the term $\left(\frac{\Delta T}{\Delta t}\right)_v$ is the temperature rate by the vertical motion, ω is the vertical wind velocity and θ is the potential temperature. A warming trend occurs during situations of subsidence ($\omega > 0$) and potential temperature increases with height, which are typically associated with anticyclonic conditions. For example, this mechanism played a key role in sustaining the August 2018 HW (Sousa et al., 2019).

c) Diabatic term. This term includes non-adiabatic processes such as latent and sensible heat fluxes or radiative effects, and hence it is often estimated as a residual of the temperature tendency (3), after accounting for horizontal and vertical terms (Chan and Nigam 2009; Wright and Fueglistaler 2013):

$$\left(\frac{\Delta T}{\Delta t}\right)_d (\lambda, \phi, t) = \frac{\Delta T}{\Delta t} - \left(\frac{\Delta T}{\Delta t}\right)_h - \left(\frac{\Delta T}{\Delta t}\right)_v \qquad (3)$$

where $\frac{\Delta T}{\Delta t}$ is the total temperature tendency and $\left(\frac{\Delta T}{\Delta t}\right)_d$ is the temperature rate due to diabatic processes. This term is also modulated by the atmospheric circulation on synoptic scales and gains in importance during summer HWs. For example, high pressure systems are associated with clear sky conditions, which increase short-wave radiative fluxes at surface, particularly in summer.

1.4. Objectives

As explained in the introduction, previous studies have used Eulerian approaches to characterize HWs, which ignore the spatial structure and temporal coherence of the events and do not allow an interpretation of the dynamical influence. To overcome this problem, the objective of this work is advancing in the description of HWs by designing an improved “Lagrangian” HW detection algorithm. This new description changes the focus from the local perspective to the HW pattern itself, following its spatio-temporal evolution. This change of paradigm is particularly relevant in the context of the ongoing climate change and the recent emergence of mega-heat waves. As a pilot study, the algorithm will be applied to characterize Iberian HWs for the 1979-2017 period, which was further motivated by the lack of catalogues with a full description of the events (e.g. areal extent, persistence, intensity, tracks, etc.) at the time of starting this PhD. The performance of the algorithm to capture European mega-heat waves is also tested, and potential applications are illustrated using the 2017 June HW as a case study. This catalogue allows us to answer some open questions: a) Which are the main characteristics of Iberian HWs? b) Are there classes (or types) of Iberian HW events with distinctive characteristics?; c) What are the synoptic conditions associated with Iberian HWs through their life-cycle?; d) How have recent changes contributed to the characteristics of Iberian HWs?; e) How does the algorithm diagnose mega-heat waves? Can the outstanding impacts of these emerging events be attributed to thermodynamical and dynamical changes?

The above questions are addressed in the following chapters. In chapter 3, the new Lagrangian algorithm is fully described and tested. An independent list of Spanish HWs provided by AEMET during the development of this Thesis is used to test the suitability of the algorithm and to calibrate thresholds, which are required to detect synoptic scale Iberian HWs.

In chapter 4, this algorithm is applied to derive a catalogue of Iberian HWs. It aims to provide a full description of events, that can be useful for potential users and applications. In particular, it allows answering questions a-d) posed above.

Finally, in chapter 5, the June 2017 mega-heat wave that affected Iberia is described, and used as a case study to test the performance of the algorithm to diagnose European mega-heat waves (question e). We show how the new approach provides a complete description of this type of HW events, making easier to establish causal links with the atmospheric circulation and detection/attribution studies.

2. Data and Methods

2.1. Data

To address the objectives of this work, different reanalysis datasets have been employed. Reanalyses were initially developed in the 1990s (Kalnay and Jenne, 1991) and nowadays they are an indispensable tool in climate research studies. They are based on a forecast model and an scheme that assimilates observational datasets for every time step in the model (Dee et al., 2011; Kalnay et al., 1996). These include several sources: weather stations, radiosondes, ships, buoys, aircrafts and satellites (from 1979 onwards). The derived data are provided in a grid for the full period of the reanalysis (i.e. complete time series), being consistent in time with the available observations and the physics of the model. The completeness of the reanalysis products does not guarantee homogeneity, due to the imperfection of the model and the limited coverage and quality of observations (Chiodo and Haimberger, 2010; Ferguson and Villarini, 2014; Hanna et al., 2016). As such, variability at different time scales is not always reproduced correctly and there are some biases (e.g. artificial trends), as well as differences among the available reanalysis products (e.g. Angélil et al., 2016; Bromwich et al., 2016; Fujiwara et al., 2017; Lader et al., 2016; Torralba et al., 2017). Due to these differences, in this work two different reanalysis have been used to evaluate the robustness of the results and their sensitivity to different reanalyses and spatial resolutions.

ERA-Interim (Dee et al., 2011) is the third-generation reanalysis of the European Centre for Medium-Range Weather Forecasts (ECMWF). It provides data from January 1979 onwards, with a ~3-month delay (i.e. data for June 2017 were ready to use by ~September 2017). The resolution of the model is T255 in horizontal and L137 vertical levels, and reanalysis data are provided every 6 hours (00, 06, 12, 18 UTC), at 60 pressure levels (from 0.1 hPa to surface) and different horizontal resolutions. In this work, regular grids of 0.5ºx0.5º and 2.5ºx2.5º resolution are employed. Figure 2.1 shows the representation of Iberia using the land-sea mask at 0.5ºx0.5º and 2.5ºx2.5º resolution, respectively. More details can be retrieved from: https://confluence.ecmwf.int/display/CKB/Copernicus+Knowledge+Base.

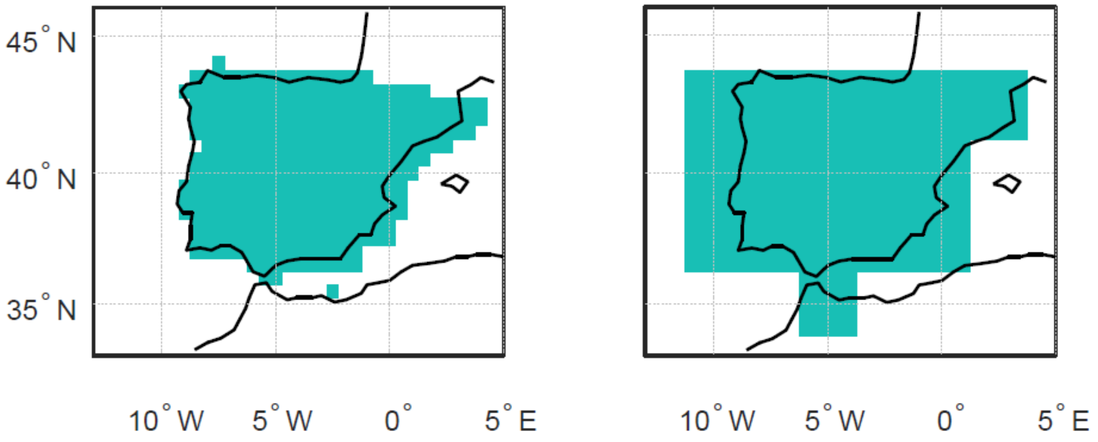

Figure 2.1. Iberian land-sea mask using (left) 0.5ºx0.5º resolution, and (right) 2.5ºx2.5º resolution.

NCEP/NCAR reanalysis (Kalnay et al., 1996) has been developed by the joint of the National Centers for Environmental Prediction and the National Center for Atmospheric Research. It provides data from January 1948 onwards, with a ~3-day delay. The resolution of the model is T62 and L28. Data are supplied in 6-hour time steps (00, 06, 12, 18 UTC) and a daily-mean basis, 17 pressure levels (up to 10 hPa) and on a 2.5ºx2.5º grid. Some derived products are also available at higher horizontal resolution over a Gaussian grid (192x94 grid points).

As compared to ERA-Interim, NCEP/NCAR reanalysis extends further back in time, and provides data faster (shorter delays in data availability). Consequently, it is especially suitable for near real-time analysis and to compare relatively long periods (~30 years) within the present and the recent past. On the other hand, ERA-Interim provides data at higher spatial resolution than NCEP/NCAR and for a variety of grids, including the 2.5ºx2.5º grid of NCEP/NCAR. This allows us to test the sensitivity of the results (e.g. the identification and characteristics of HWEs) to changes in: 1) horizontal resolution, by comparing the results from ERA-Interim data at different horizontal resolutions (0.5ºx0.5º vs 2.5ºx2.5º); 2) the reanalysis product, by comparing the results from ERA-Interim and NCEP/NCAR data at the same (2.5ºx2.5º) resolution.

ERA-Interim reanalysis at 0.5º x 0.5 resolution is employed to derive the catalogue of Iberian HWs (Chapter 4). For those exercises that required longer series (e.g. comparison of past and present periods, section 4.4 and 4.5) and faster accessibility (the assessment of the June 2017 mega-heat wave, Chapter 5) data from NCEP/NCAR reanalysis at 2.5ºx2.5º were used instead. The variables employed include T850 for the entire globe and Z500, and T2m for specific domains of the Euro-Atlantic sector.

2.2. *Methods*

2.2.1. Hypothesis testing

Different techniques have been employed in this Thesis for the hypothesis testing. Long-term trends are computed as the slope of the linear regression. Their statistical significance is assessed with the Spearman-rho test (Ahmad et al., 2015; Jaiswal et al., 2015; Lanzante, 1996; Yue et al., 2002). This is a non-parametric test, and hence it is less affected by the presence of outliers than parametric tests (Lanzante, 1996). The null hypothesis (H_0) is that all the data in the corresponding time series are independent and identically distributed, consequently without trend; whilst the alternative hypothesis (H_1) is that there is a decreasing or increasing trend. The test statistics R_{sp} and the standardized statistics Z_{sp} are defined as:

$$R_{sp} = 1 - \frac{6\sum_{i=1}^{n}(D_i - i)^2}{n(n^2-1)} \qquad (1)$$

$$Z_{sp} = R_{sp}\sqrt{\frac{n-2}{1-R_{sp}^2}} \qquad (2)$$

Where D_i is the rank of the ith observation, n is the total length of the time series. Z_{sp} follows a Student's t-distribution with (n-2) degree of freedom. Therefore if $|Z_{sp}| > t_{(n-2,1-\frac{\alpha}{2})}$, H_0 is rejected and the trend is significant at (1-α) level.

To assess the significance of hypothesis testing, e.g. difference of means for a given sampled population and the full sample (climatology), a bootstrap test of 100,000 iterations has been used. In each iteration, we selected a random subset (from the entire pool of available data) with the same size as the number of cases included in the sampled population. This method provides a random distribution of the tested parameter (e.g. the mean), against which the observed value is compared. The latter is significant at the 95 (99) % confidence level if it lies above the 97.5th (99.5th) or below the 2.5th (0.5th) percentile of the random distribution.

To compare the average value of two independent distribution ($\overline{\mu_1}$ and$\overline{\mu_2}$), the Mann-Whitney U test has be applied (Gibbons and Chakraborti, 2014; Reeves et al., 2007). This test is the non-parametric version of the t-test and therefore it has the advantage that it does not assume a normal distribution. In this test the null hypothesis and the alternative hypothesis are:

$$\begin{cases} H_0: \overline{\mu_1} \leq \overline{\mu_2} \\ H_1: \overline{\mu_1} > \overline{\mu_2} \end{cases} \tag{3}$$

To test this hypothesis the procedures is as follows:

1. Assign numeric ranks to all the observations (D_{i1}, D_{i2}), to do so, all the observations from both groups are put together.
2. The ranks of the second sample are summed:

   $$W = \sum_{i=1}^{n_2} D_{i2} \tag{4}$$

3. The following statistic is computed:

   $$U = W - \frac{n_2(n_2+1)}{2} \tag{5}$$

4. If $U < C_{n1,n2,\alpha}$, where $C_{n1,n2,\alpha}$ is a tabulated value (e.g Walpole et al., 2011), the null hypothesis is discarded and $\overline{\mu_2}$ is significant higher than $\overline{\mu_1}$ at (1-α) level.

2.2.2. Self-Organizing Maps

The Self-Organizing Maps technique (SOM hereafter, Crane and Hewitson, 2003; Kohonen, 2001) is a clustering algorithm which uses a neural network and an unsupervised and iterative learning process to identify recurrent spatial patterns by grouping observations (days in this work) with similar 2D data distribution into a user-selected number of clusters. Unlike other clustering methods, like the k-means, SOM avoids assumptions on data distribution and it is trained during the data processing depending on the input data. First, the clusters are randomly initialized. An input data vector is then compared to each of these clusters, assigning it to the closest one (as measured by the Euclidean distance). The selected cluster is then modified to reduce the difference with the input vector. Different to other clustering algorithms, the closer clusters are also modified. Thus, each input sample contributes to the characterization of more than one cluster. In the final product, all inputs have been assigned to one cluster and the clusters are ordered according to their similarity, e.g. anticyclonic clusters are listed in a row and separated from cyclonic clusters. (see Cassano et al., 2006 for more details on this training). The SOM method is available at the nctool Matlab® toolbox.

This method has been applied to the T850 field in order to identify recurrent temperature patterns associated with Iberian HWEs. To do so, we first computed the mean spatial pattern of standardized T850 anomaly for all Iberian HWDs of each HWE, thus obtaining one pattern per HWE. SOM was then applied to classify HWEs according to their mean T850 patterns over the region [20-60 ºN, 35ºW-35ºE], which yielded a regionalization of Iberian HWEs. Similar results were obtained for small changes in the spatial domain and the number of clusters.

SOM has also been exploited to identify weather regimes (WRs afterward) over the Euro-Atlantic sector. To do so, we used the standardized Z500 anomaly field over the region [30-60ºN, 35ºW-35ºE] for all June-September days of the 1979-2017 period, retaining four WRs, as in Horton et al., (2015). The daily catalogue of WRs allows classifying HWDs into one of the four WRs (Figure 2.2). The first two WRs display a zonal dipole, with positive (negative) Z500 anomalies in the eastern Atlantic (northern-central Europe) and southeastern Europe (eastern Atlantic), respectively. WR3 depicts a meridional dipole dominated by positive Z500 anomalies near UK, that is characteristic of European blocking, and slightly negative Z500 anomalies over the Mediterranean. Finally, WR4 shows positive Z500 anomalies in western Europe, resembling the occurrence of subtropical ridges in the Euro-Atlantic sector.

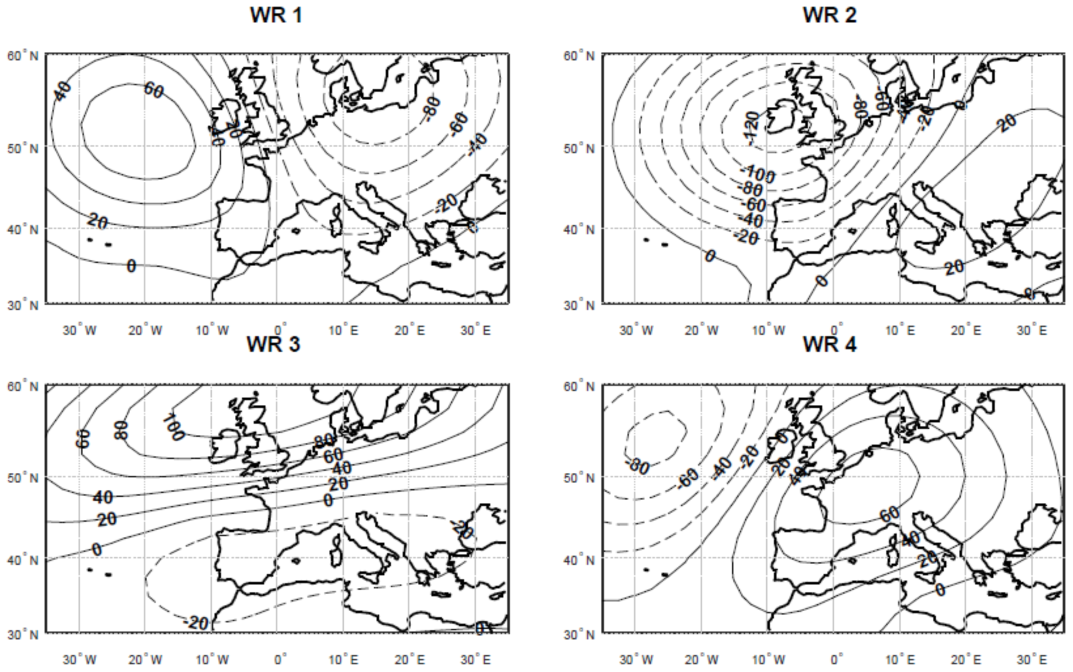

Figure 2.2. Composites of Z500 anomalies (contours, in m) for all June-September days of the 1979-2017 period classified in each WR.

2.2.3. *Flow Analogues.*

Recent studies have applied the analogue method to quantify the dynamical contribution to near-surface anomalies during extreme events and in the detection and attribution of extreme events to climate change (e.g. Stott et al., 2016; Yiou et al., 2017). The latter requires searching for flow analogues of the extreme event in two different subperiods. Herein, we have applied this method to each day of selected HWEs, by searching for analogues of the actual Z500 field in recent past and present subperiods, as defined in chapters 4 and 5. To do so, the NCEP/NCAR reanalysis was used as it covers a longer period than ERA-Interim.

The analogue technique employed in this work follows Jézéquel et al. (2018) and was applied to different HWEs and with different purposes (i.e. to reconstruct different target fields from flow analogues). In both cases, for each HWD, we looked for the N=20 days of each subperiod with the nearest Z500 anomaly fields. The search was restricted to the (-30, +30) interval of the corresponding calendar day, and the distance criterion was defined by the Euclidean distance over the [30-55ºN, 10ºW-15ºE] region. Then, we randomly picked one of the N analogues and repeated this process for each day of the considered event. This process was repeated 100,000 times for each subperiod separately, in order to derive a statistical distribution of the target field. The difference between the analogue-based distributions of both subperiods was assessed with a Mann-Withney U test and should be attributed to changes in the climatology. In addition, we also assessed whether the dynamics played a significant role in the observed magnitude of the reconstructed fields. To do this, the analogue-based distribution was compared with that obtained randomly. This process was performed for each subperiod, separately, by choosing random periods of successive days with the same length as the HWE, in order to account for persistence. Different choices in the spatial domain or the number of circulation analogues were tested, yielding similar results. In chapter 4, the top three Iberian HWEs were analysed separately in order to assess how these events may have looked like in the recent past (1948-1978), as compared to the present (1979-2017). For each of the N flow analogues, we first verified if an Iberian HWD was detected, and if so, the instantaneous pattern and the corresponding parameters were retained. The target fields were the mean spatial pattern and characteristics of the Iberian HWE (averaged over its life-cycle). Then, we reconstructed their analogue-based distributions for the present and recent past, allowing us to infer how that Iberian HWE could have been in the recent past.

In chapter 5, the analogue method is applied to reconstruct the Iberian T2m anomalies that could be expected from the atmospheric circulation associated with the June 2017 mega-heat wave. In this case, the recent past and present subperiods are defined as 1948-1979 and 1980-2016, respectively, and the target field is the Iberian-mean T2m anomaly averaged for the mega-heat wave period. The difference between the present and recent past distributions represents the overall changes. In principle, the differences between the flow-conditioned distributions of both subperiods should be ascribed to thermodynamical changes (i.e. warming), since the atmospheric circulation is constrained in the process by choosing the best flow analogues of each subperiod. However, the method does not impose a threshold to the metric of similarity (the RMSE) in order to discard flow analogues that are not good enough. Therefore, there could be differences between the flow analogues of both subperiods (e.g. worse analogues in the recent past than in the present) that contribute to the change in the reconstructed distributions. These differences are referred to as dynamical changes, since they concern to changes in the atmospheric circulation between subperiods. To quantify the contribution of dynamical changes, we removed the mean Z500 and T2m trends, thus eliminating the thermodynamically forced long-term changes in Z500 (e.g., Z500 rise by warming in lower levels). Then, new analogue-based distributions for the present and recent past were recomputed again from the detrended data, as explained above, being referred to as thermodynamically adjusted distributions. As warming effects have been removed, the difference between the thermodynamically adjusted distributions of the present and recent past are largely due to dynamical changes. Thermodynamical changes are thus defined as the residuals of the total changes (difference between the original analogue-based distributions) with respect to the dynamical changes (difference between the thermodynamically adjusted distributions).

2.2.4. Heat Wave Magnitude Index event

HWEs are ranked according to an adapted version of the HWMId index of Russo et al. (2015). This modified version integrates the intensity, spatial extension and persistence of HWEs into a single index, herein referred to as Heat Wave Magnitude Index event (HWMIe), which yields one value per HWE. The HWMId index of Russo et al. (2015) normalizes the temperature anomaly using the interquartile range:

$$HWMId_{i,j} = \begin{cases} \frac{T_d - T_{25p}}{T_{75p} - T_{25p}} & T_d - T_{25p} > 0 \\ 0 & T_d - T_{25p} \leq 0 \end{cases} \qquad (6)$$

where T_d is the daily mean T850 of day d and T_{25p} (T_{75p}) is the corresponding 25th (75th) percentile of that calendar day computed from the 31-day centred window of the 1981-2010 period. Russo et al. (2015) used this index to rank summers and not individual HWEs, and hence it does not distinguish different HWEs that occur within the same season (e.g. in addition to the August 2003 mega-heat wave, several regions were also affected by a HW in June 2003).

Conversely, the HWMIe aims to quantify the integrated effects of HWEs from an impact-oriented perspective. Therefore, the HWMId is only computed over inland grid points experimenting HW conditions (i.e. grid points over sea or unaffected by HWEs are discarded). For a given HWD, the area-weighted HWMId sum for the land grid points under HW conditions is first computed (HWMI) and these daily values are later accumulated over the life-cycle of the HWE to yield HWMIe:

$$HWMI = \sum_{i,j} HWMId_{i,j} * \cos(lat_j) \qquad (7)$$

$$HWMIe = \sum_{d} HWMI \qquad (8)$$

where i and j are the longitude and latitude, and d is each day of the HWE. This approach allows us to provide a metric for HWEs intensity by taking into account the persistence, spatial extent and amplitude of HW conditions over the land area affected by their spatial patterns.

2.2.5. Blocking and Ridge catalogues

To further characterize the atmospheric circulation, we have also used catalogues of blocking and subtropical ridge events for the 1948-2017 period of the NCEP/NCAR reanalysis. The blocking catalogue is computed using the Barriopedro et al., (2006) algorithm, which is based on the persistence (5 days) of large-scale (12.5° in longitude) reversals in the meridional Z500 gradient around typical latitudes of the extratropical jet stream (~50ºN). In addition, the catalogue from Sousa et al., (2018) is employed to diagnose the occurrence of subtropical ridges in three non-overlapping longitudinal sectors of 30° width that jointly extend over 30°W–60°E (Figure 2.3): Atlantic (ATL, from 30ºW to 0ºW), European (EUR, from 0º to 30ºE) and Russian (RUS, from 30ºE to 60ºE). These sectors are further sub-divided into two smaller 15º width subsectors (western and eastern halves of each sector). For each subsector, two conditions are imposed to detect a subtropical ridge in a given day: (i) at least 75% of the grid points within 35–55°N displayed Z500 values above the daily 80th percentile, computed from all 31-day centred windows of the analysed period, and (ii) no more than 50% of the grid points within 55–75°N are above the same threshold. The latter criterion is included to avoid the detection of blocking patterns as subtropical ridges, thus ensuring that the same day is not catalogued as a blocking and a ridge simultaneously.

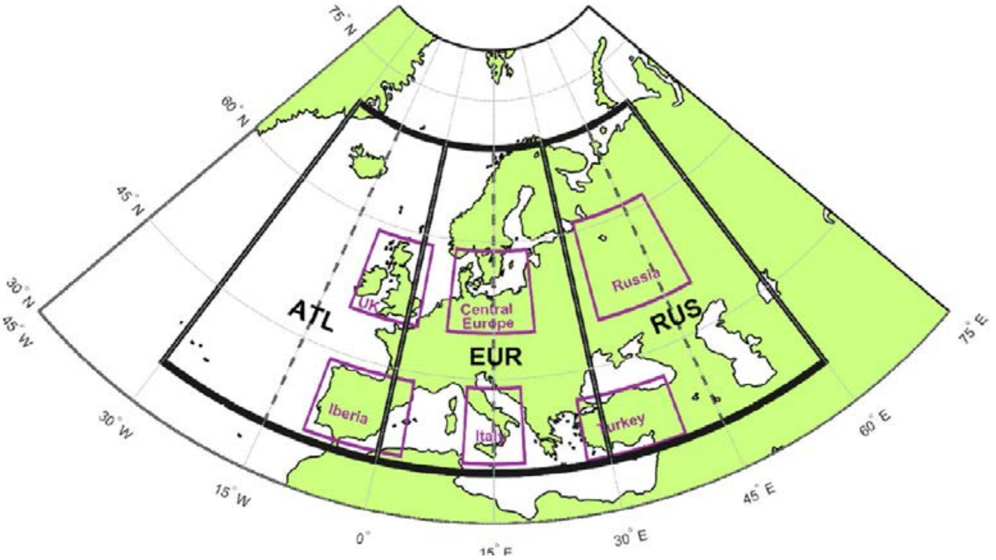

Figure 2.3. Geographical representation of the considered sectors in the subtropical ridge catalogue (thick black frames): Atlantic (ATL, from 30ºW to 0ºW); European (EUR, from 0º to 30ºE); Russian (RUS, from 30ºE to 60ºE). Each of these sectors are subdivided into two smaller 15º width subsectors by the dashed black lines. Figure extracted from Sousa et al., (2018).

3. HW detection algorithm

In this chapter we present a Lagrangian-inspired algorithm to identify and characterize HWs from daily gridded temperature fields. This description changes the focus from the local perspective of Eularian approaches to the temperature field, identifying and tracking the spatio-temporal evolution of HW patterns.

3.1. Detection scheme

Our HW detection algorithm comprises two phases. First it identifies daily HW patterns. Later it detects HWEs by tracking them. Figure 3.1. shows a schematic diagram summarizing the main steps of the algorithm including the adopted thresholds that will be justified below. The method works as follows (Sánchez-Benítez et al., 2019):

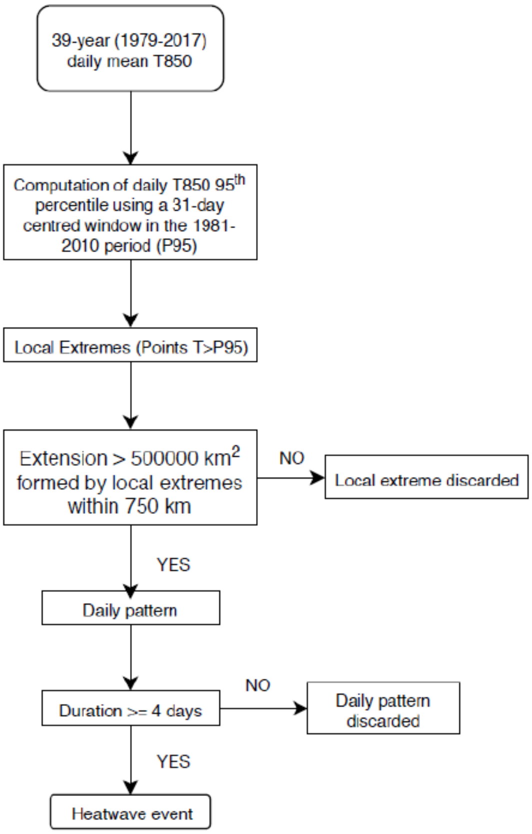

Figure 3.1. Schematic of the HW detection algorithm.

For each day, we identify the grid points exceeding a local temperature threshold (t_tem), defined for each grid point and calendar day, as explained below. They are referred to as local extremes. Then we search for areas with a high concentration of these extremes (hereafter named as daily HW patterns). They are formed by local extremes separated by less than a distance threshold (t_dis) covering an area of at least a given extension threshold (t_ext). The use of t_dis allows to aggregate points into the same pattern that are not necessarily contiguous but are separated less than the characteristic synoptic scale (and hence associated with the same weather system). Meanwhile, a t_ext allows filtering small scale patterns.

Once a daily HW pattern is identified, its spatio-temporal evolution is tracked in order to identify HWEs. This tracking aims to follow the evolution of the associated weather system. If it remains almost stationary (which is typical of blocking) the HW patterns of two consecutive days should have high overlapping (hereafter referred to as stationary HW pattern, Figure 3.2 top). However, if there is a substantial displacement of the weather system between two consecutive days (e.g. a subtropical ridge moving eastward), the HW pattern is expected to evolve in a similar way. In this case, some grid points that were under HW conditions on day d would remain so on day d+1, but, in general, the HW would mostly affect a new area (hereafter referred to as transient HW pattern, Figure 3.2 bottom). As a consequence, the overlapping would be considerably lower than in stationary patterns, but still associated with the same HWE. Accordingly, in our algorithm, a HW pattern on day d+1 is considered the continuation of another one detected on day d if at least one of these two conditions is satisfied: 1) their areas overlap at least a certain threshold (t_ove1; quasi-stationary HW patterns); 2) there is some overlap and the distance between their centres, defined as the area-weighted average of the standardized temperature anomalies, is lower than a distance threshold (t_spe; transient HW patterns). If a daily HW pattern is tracked for at least a duration threshold (t_dur) it is considered a HWE. All daily HW patterns that do not satisfy the aforementioned conditions are disregarded, and from now on, the term daily HW pattern will be restricted to the daily occurrences of a given HWE. Note that two HWEs can occur the same day and affect different regions. As such, a distinctive label is given to each HWE (and to all the grid points conforming its daily HW patterns). All days with at least one HWE over a given region are referred to as HWDs.

The algorithm provides the following outputs:

a) Daily HW patterns characteristics. They are identified by the label of the HWE they belong to, as well as by several parameters derived from their embedded local extremes such as the areal extent (in km^2), the intensity (in standard deviations, SD, measured by the area-weighted mean standardized temperature anomaly), the HWMI index (as defined in section 2.2.4), the overlapping among consecutive days (in %), displacement speed (in km/day) and the centre location (the mean longitude and latitude weighted by the temperature anomaly).
b) HWE characteristics. They include the label of the event, the start and end days, duration (in days), HWMIe index (as defined in section 2.2.4), as well as the maximum and mean daily parameters defined above and computed for the entire life-cycle of the HWE (e.g. mean areal extent, intensity, overlapping, speed and centre location).
c) 2-D daily maps with the HW patterns of all HWEs detected each day of the analysed period (see examples in Figure 3.2).

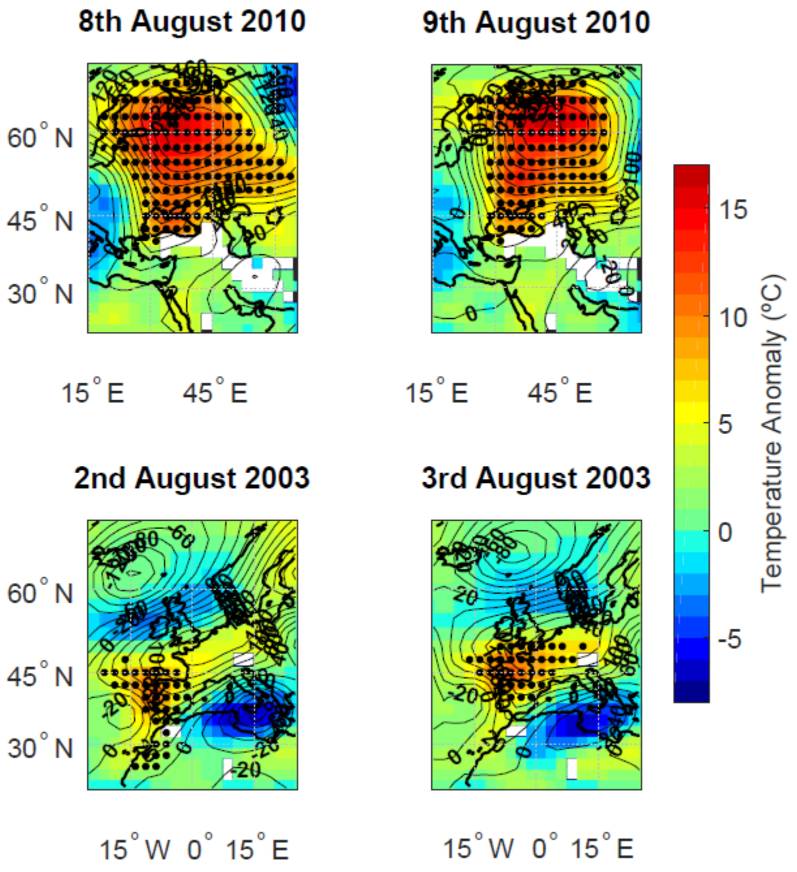

Figure 3.2. Temperature (shading, in ºC), and Z500 (contours, in m) anomalies for stationary (top, associated with a blocking) and transient (bottom, associated with a subtropical ridge) HW patterns. Grid points under local HW conditions are shown with dots. Data were extracted from NCEP/NCAR reanalysis.

3.2. Independent test

An independent list of Spanish HWEs (AEMET, 2018) based on land observations from weather stations is used to test and calibrate the algorithm. HWEs are therein defined as exceedances of the local 95th percentile of daily maximum T2m (computed using all days of July and August of the 1971-2000 period) in at least 10% of the weather stations during three or more consecutive days. We stress that stations used in this definition are not homogeneously distributed and the extension threshold can be satisfied by a cluster of nearby stations or by sparse stations that are far away. In spite of the differences in the underlying data and the methodology (observations vs reanalysis, Eulerian vs Lagrangian, local stations vs grid points), the AEMET catalogue is the only one available for our area of study.

First of all, we have tested whether our algorithm is useful to detect HWEs, as defined by AEMET. To do so, we run our algorithm using thresholds coherent with the AEMET definition. Data from NCEP/NCAR reanalysis are used since they cover the start date of the AEMET list (1975). The algorithm performs well as it captures all HWEs and ~90% of the Spanish HWDs in the AEMET catalogue. In fact, only those HWDs whose characteristics are too close to the detection thresholds are not detected by the algorithm (Table A1 in the Appendix). Note that AEMET, and many other HW definitions rely on T2m data; this field was also tried in an earlier version of the algorithm. Nonetheless, for our algorithm, the use of T2m involved several issues. Over the sea, T2m is strongly affected by Sea Surface Temperature (SST), which also responds to the atmospheric conditions but it is also affected by oceanic processes and therefore its variation is slower and smoother in comparison to land temperatures. This can become an issue during the marine HWEs (large sea areas with temperatures above t_tem, Hobday et al., 2016; Holbrook et al., 2019; Oliver et al., 2018), which are out of the scope of this work. These marine HWEs become problematic as they can connect two independent HW patterns (e.g. those occurring in different continents; Figure 3.3). To solve these issues, the ocean should be masked. However, this would clearly affect the detection of HWEs over areas surrounded by sea (e.g. Iberia), and would prevent the assessment of the HWE evolution before and after affecting land areas. Consequently, a higher level (850 hPa) has been chosen for the identification of HWEs, which is also widely employed to assess weather conditions (e.g. Cardil et al., 2015; Cassano et al., 2017; Tamarin-Brodsky et al., 2019). To check that this pressure level represents properly the surface conditions, Figure 3.4 shows the correlation between the Iberian mean daily T2m and the corresponding temperatures at different pressure levels for all days of the extended summers of the 1948-2017 period. The correlation is very high (r^2=0.96) up to the 850 hPa level, with a pronounced decay upwards. Note that this choice requires masking those grid points (e.g. over Alps and Atlas Mountains) that are located at higher altitudes than those typical of the 850 hPa pressure level (~1,500 m asl).

On the other hand, and different to the AEMET definition (and those based on daily maximum temperatures), the daily mean temperature is herein employed. This choice is motivated by our data sources, since the NCEP/NCAR reanalysis only provides data every 6h, which prevents computing the daily maximum T850.

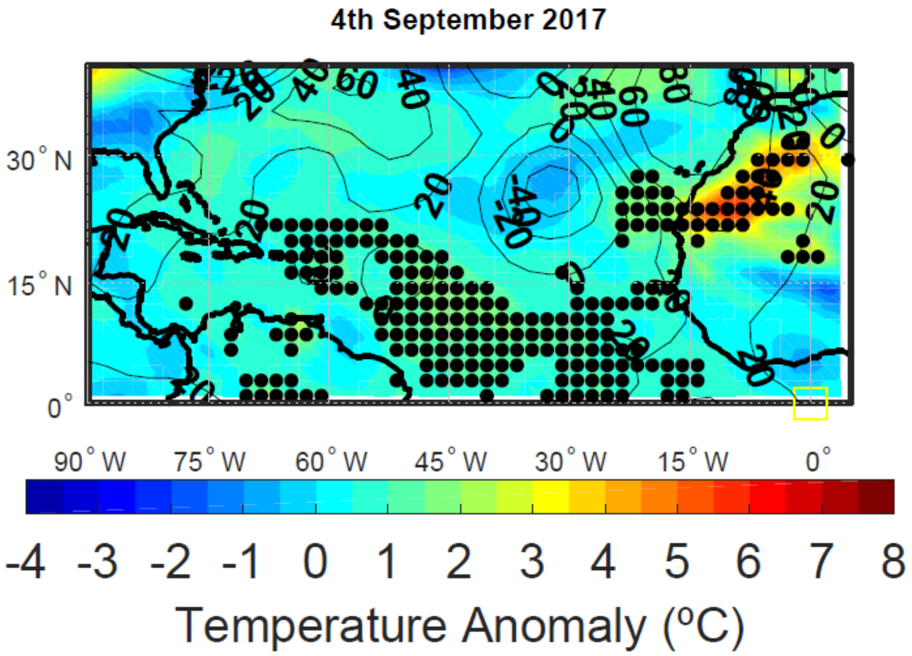

Figure 3.3. T2m (shading, in ºC), and Z500 (contours, in m) anomalies for a day when different land HW patterns are connected by a marine HW. Grid points under local HW conditions are shown with dots. Data were extracted from NCEP/NCAR reanalysis.

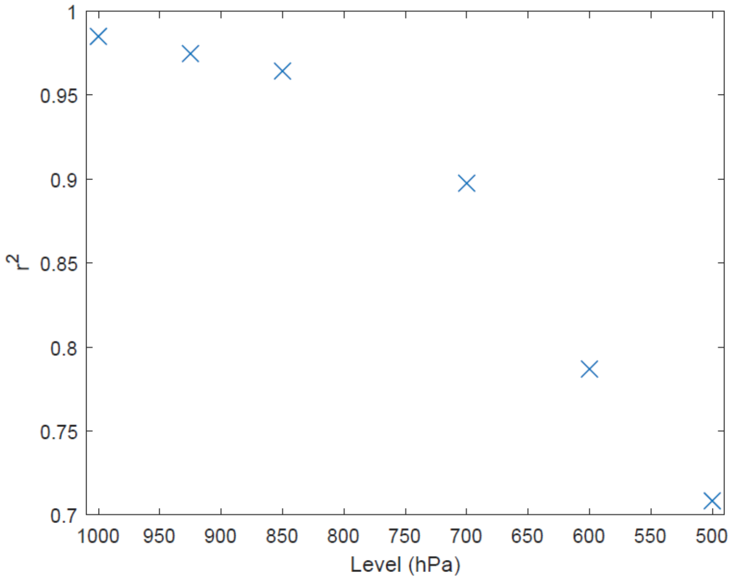

Figure 3.4. Correlation between the Iberian mean daily T2m and the corresponding temperatures at different vertical levels for all days of the extended summer (June-September) of the 1948-2017 period. Data were extracted from NCEP/NCAR reanalysis.

3.3. Definition of thresholds

Once we tested that the algorithm satisfactorily captures HWEs, we proceeded to calibrate it (i.e. setting thresholds), focusing on synoptic scale Iberian HWEs. The first threshold is t_tem. In agreement with most HW definitions, a local percentile-based t_tem was chosen to avoid biasing the detection of HWEs to climatological warmer regions. We used the 95th percentile, because it is widely employed, provides an enough sample to compute statistics, and ensures that the obtained HWEs are strong enough to cause relevant impacts (Garcia-Herrera et al., 2005; Lin et al., 2019; Scortichini et al., 2018).

Different to the AEMET definition, which uses a constant threshold for all days of the extended summer, t_tem is herein allowed to accommodate to the seasonal cycle of the local temperature. To illustrate the importance of this choice, Figure 3.5 shows the t_tem seasonal evolution for a grid point close to Madrid, computed both as an invariant threshold (which, in this case is close to 22ºC) and a time-varying threshold. The latter, computed from running windows of different width, reveals a pronounced seasonal cycle, in accordance with the mean temperature seasonal evolution (Figure 1.5). The difference between the time-varying and the invariant threshold is ~-3 ºC in early June, rising to ~+1 ºC by late July-early August, and decreasing afterwards to ~-4 ºC in late September. Hence, a constant percentile provides a value that is too high (low) in early and late (mid) extended summer. Regarding the length of the moving windows, the shortest one (3 days) provides a seasonal evolution, with differences of ~1ºC in few days caused by the data scarcity in the percentile computation. To avoid this issue, a 31-day moving window was chosen, as it provides a smoother evolution, while still capturing the seasonal cycle.

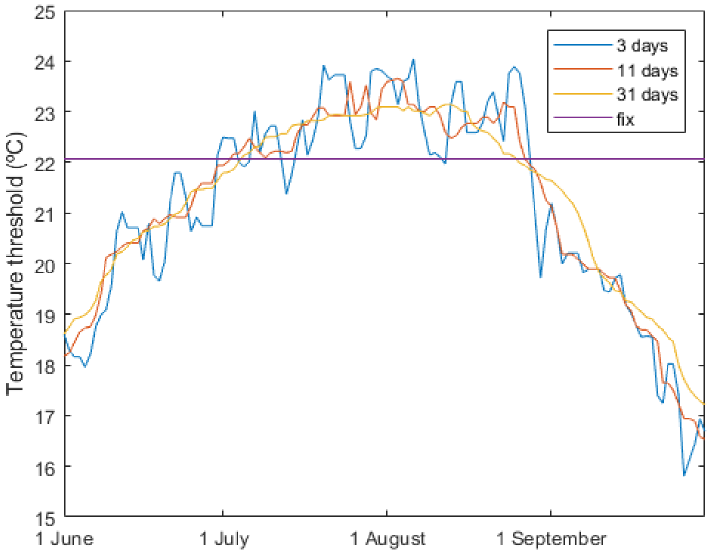

Figure 3.5. Seasonal evolution of the 95th percentile of T850 for 1981-2010 and a grid point close to Madrid, computed using a constant threshold (purple, all days of the extended summer) and moving windows of different width (blue for 3-days, red for 11-days and yellow for 31-days). Data were extracted from NCEP/NCAR reanalysis.

Although local extremes tend to occur in adjacent grid points, HW patterns can also display non-contiguous extremes associated with the same weather system (e.g. Figure 3.6. where the HW pattern is split in two, with grid points under HW conditions both at the south and northeast of the Alps). Accordingly, local extremes within a distance of t_dis are considered the same HW pattern. This threshold was set to 750 km according to the distance equivalent to the masked area in the Alps and Atlas regions. Note that the chosen threshold is close to Rossby radius of deformation (Lr), which is often employed to characterize the spatial scales of synoptic weather systems (Holton and Hakim, 2012). We further tested that higher thresholds could join HW patterns affected by different synoptic systems, as can be seen in Figure 3.7. In this example, where 1,000 km is used for t_dis, two independent HW patterns (associated with an Atlantic subtropical ridge and a Scandinavian blocking, respectively) are identified as the same HW pattern.

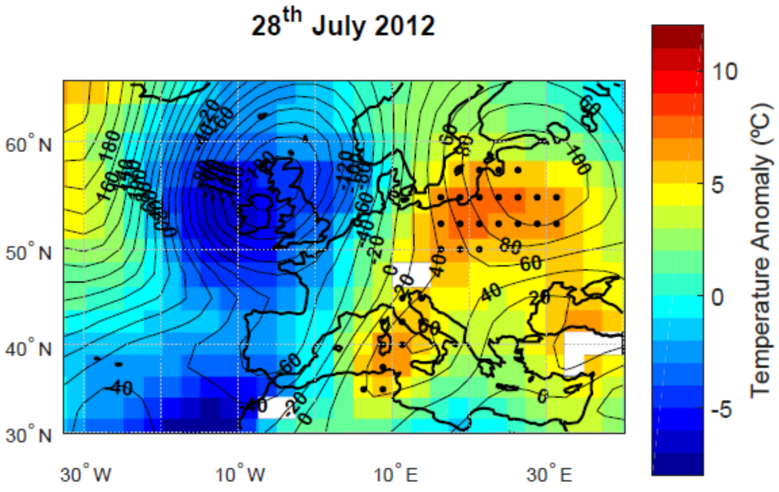

Figure 3.6. Temperature (shading, in ºC), and Z500 (contours, in m) anomalies for day with two HW patterns associated with the same weather system. Grid points under local HW conditions are shown with dots. Data were extracted from NCEP/NCAR reanalysis.

The t_ext threshold allows us to identify coherently HWs on large spatial scales. To be consistent with the t_dis threshold, t_ext was approximated by t_dis^{2}~ 750 km x 750 km = 562500 km^{2} (~Lr^{2}), and hence set to 500,000 km^{2} (~areal extent of Spain). The results are robust to small variations in this threshold. Obviously, when t_ext increases the number of HWEs and HWDs decrease (see Figure 3.8 for an example over Iberia). However, the exact value of t_ext is not so important, as the remaining thresholds (t_ove, t_spe and t_dur) also filter small scale HW patterns. We should note that the extension condition does not require a HW pattern to affect an inland area of t_ext surface area, since both land and sea grid points contribute to the areal extent of the HW pattern. Obviously, the chosen value for t_ext allows the detection of (but is not restricted to) mega-heat waves, which have at least the double extension of this threshold.

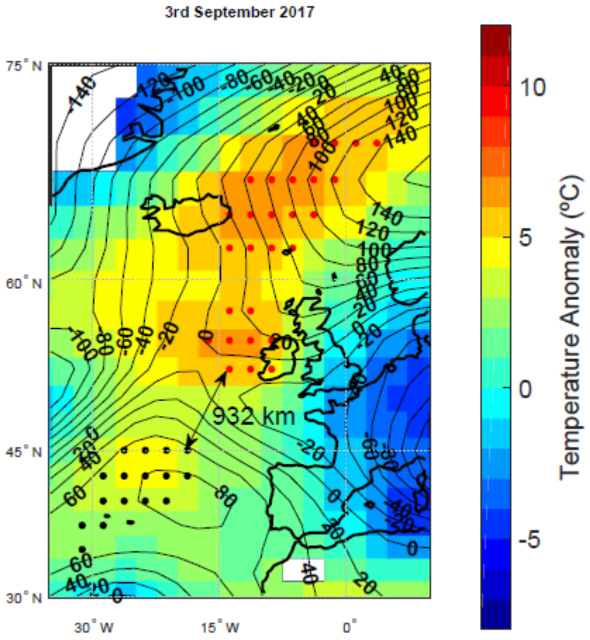

Figure 3.7. Temperature (shading, in ºC), and Z500 (contours, in m) anomalies for a day when the use of a too high t_dis threshold causes the merging of two independent HW patterns (highlighted by red and black dots), separated by the distance shown by the arrow. Data were extracted from NCEP/NCAR reanalysis.

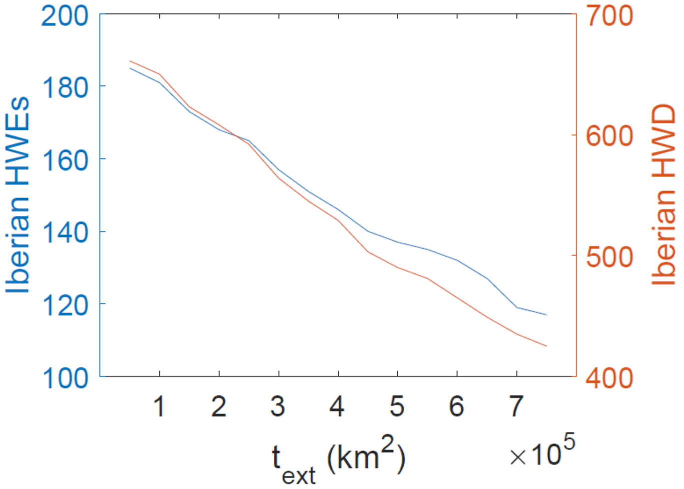

Figure 3.8. Number of Iberian HWEs (blue) and Iberian HWDs (red) captured by our algorithm for different extension thresholds. Data were extracted from NCEP/NCAR reanalysis.

Once daily HW patterns are fully defined, the following step is to fix the thresholds involved in their tracking. There are two options to consider a daily HW pattern the continuation of that observed on the day before. The first one concerns to quasi-stationarity. We consider that two HW patterns of consecutive days are quasi-stationary when their areas overlap by more than 50% (t_ove). This involves satisfying at least one of the following conditions: 1) more than t_ove of the HW pattern of day d belongs to the HW pattern of day d+1; 2) more than t_ove of the HW pattern of day d+1 was part of the HW pattern of day d. On the other hand, and as the second option, the algorithm allows detecting HWEs with non-stationary HW patterns. In this case, two successive HW patterns can still be considered the same HWE, if their areas display any overlapping (larger than zero) and their centres are separated by less than t_spe. This threshold was set to 1,000 km, and chosen empirically, after the visual inspection of cases (e.g. this value allows us tracking the August 2003 mega-heat wave as a single event). If two or more daily HW patterns satisfy these criteria, the ones with higher overlapping are selected.

The last threshold that must be fixed is t_dur. In previous studies it is common to set this threshold between 3 and 6 days. Figure 3.9 shows an almost linear decrease in the frequency of Iberian HWDs detected by the algorithm when t_dur increases. However, the percentage of AEMET HWDs captured by our algorithm displays a different dependence, with a clear decrease between four and five days. Consequently, a 4-day persistence was chosen for the t_dur threshold.

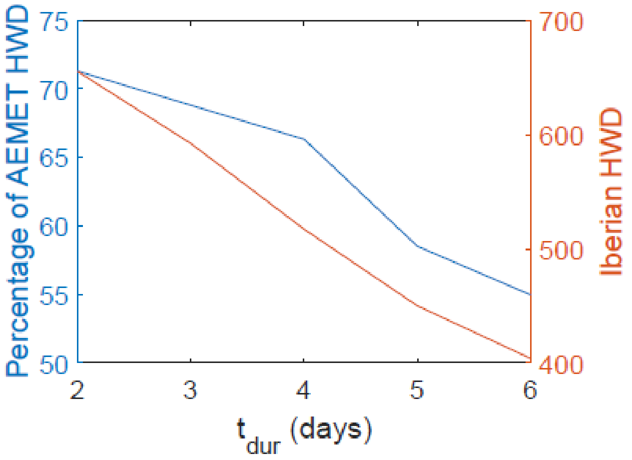

Figure 3.9. Percentage of Iberian HWDs (blue) from the AEMET list captured by our algorithm and Iberian HWDs (red) obtained using the algorithm for different length threshold. Data were extracted from NCEP/NCAR reanalysis.

4. Tracking Iberian Heat waves from a new perspective

4.1. Climatology of Iberian heat waves

As described in Section 2.1, the Iberian catalogue of HWEs has been obtained from T850 data of ERA-Interim with a 0.5º x 0.5º resolution and for the 1979-2017 period. Although the script can be run for any spatial domain, we used global data to avoid border effects. Afterwards, we selected those HWEs that affected any land grid point of the Iberian Peninsula for at least one day of the extended summer (Iberian HWEs, hereafter). The resulting catalogue contains 188 Iberian HWEs, leading to 623 Iberian HWDs during the extended summers of 1979-2017 (Table A2 in the Appendix). Recall that the term Iberian HWDs refers to those days when a given HWE affected Iberia, which does not necessarily include all days of the HWE life-cycle. These numbers are higher than those obtained in previous works with similar thresholds (Stefanon et al., 2012; Perkins, 2015; AEMET, 2018) due to the inclusion of September and the lack of a strict stationarity in the detection criteria of synoptic HWEs. There are no days with more than one HWE over Iberia and hence HWEs affect Iberia during 3.3 days, on average. The time series of Iberian HWEs and HWDs are shown in Figure 4.1. Iberian HWEs occurred every year of the analysed period, with a maximum of 10 in 2003 and 2017. The 2003 summer also displays the highest number of Iberian HWDs (a total of 45). The occurrence of Iberian HWEs and HWDs has increased in the 1979-2017 period, with significant positive trends of +1.0 HWE decade^{-1} ($p<0.01$) and +2.6 HWDs decade^{-1} ($p<0.05$), respectively. Iberian HWEs affect Iberia for 3.3 days on average, so the trend of +1.0 HWE decade^{-1} should translate into a trend of +3.3 HWDs decade^{-1}. As the actual trend of HWDs is lower than that, we infer that Iberian HWEs have become more transient. This is confirmed by computing the slope of Iberian HWDs associated with each Iberian HWE (Figure 4.2), which shows a non-significant decreasing trend. Therefore, the upward trend of HWDs is due to the increase in HWEs.

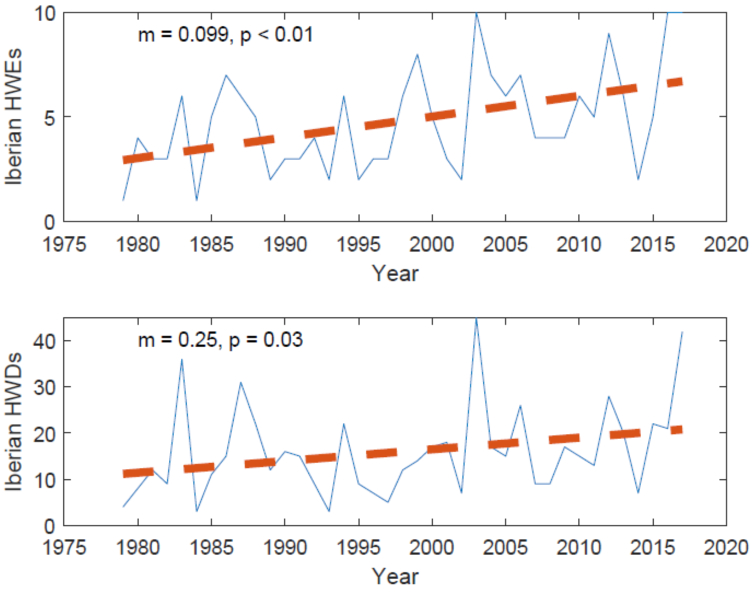

Figure 4.1. Extended summer frequency of (top) Iberian HWEs and (bottom) Iberian HWDs for the 1979-2017 period. The dashed line indicates the adjusted linear trend.

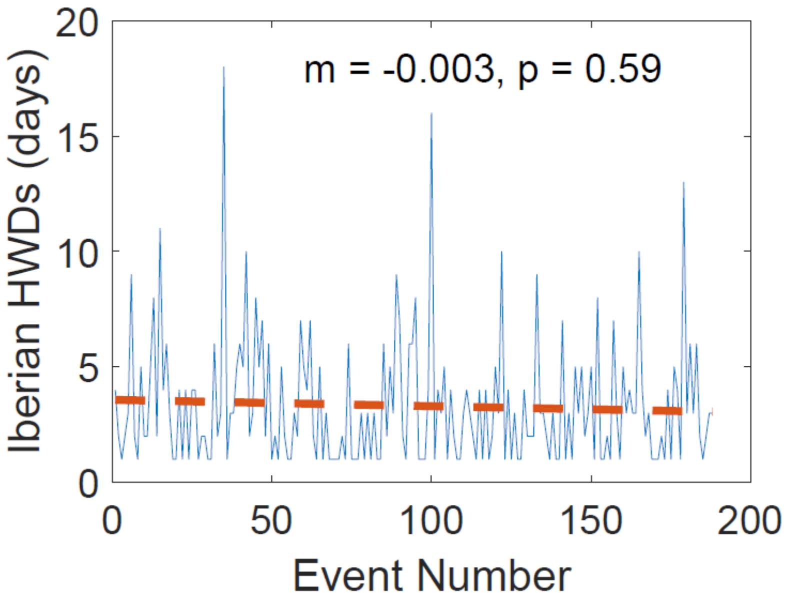

Figure 4.2. Iberian HWDs for each Iberian HWE. The x-axis shows the label of the Iberian HWE. The panel also includes the linear regression (red dashed line) and its slope (m) and significance (p).

As our algorithm focuses on synoptic HWs patterns instead of local events, it can also draw information on their spatio-temporal evolution, including periods before (pre-Iberian phase), during (Iberian phase) and after (post-Iberian phase) they affect Iberia. A summary of the main characteristics of Iberian HWEs is provided in Table 4.1 (last column). These parameters display large standard deviations (even higher than the mean in some of them), pointing to substantial variability among events, a typical feature of extreme events. Although HWEs affect Iberia for 3.3 days, they last 8.6 days on average, indicating a transient character. Within the life-cycle, the pre-Iberian phase is considerably shorter than the post-Iberian phase (1.7 vs 3.4 days/event). Indeed, more than half HWEs (55.4%) already hit this region the first day they are detected, indicating that Iberia is a favourable region for the build-up of synoptic HW conditions. Differently, the post-Iberian phase lasts at least as the Iberian phase, and most HWEs (76%) were still detected after affecting Iberia. The areal extent of HWEs tends to peak in the Iberian phase, when it reaches a mean extension of 2.6 million km^2, significantly higher than the 2.1 and 1.9 million km^2 of the pre- and post-Iberian phases ($p<0.01$). As expected from the land-sea distribution, the Iberian area affected by these events is on average one order of magnitude lower (around 20% of Iberia) than their total extension, meaning that Iberian HWEs have strong regional signatures.

Iberian HWEs characteristics	Atlantic	Subtropical	European	Mediterranean	All
Pre-Iberian phase (days)	1.8±2.6	1.9±3.3	1.3±2.6	1.8±4.1	1.7±3.2
Iberian phase (days)	3.5±3.0	3.7±3.5	3.5±2.5	2.6±2.1*	3.3±2.8
Post-Iberian phase (days)	2.5±2.4	3.9±3.4	2.4±2.9*	5.0±5.9*	3.4±3.9
Mean extension (10^6 km^2)	2.2±1.3	3.1±2.3**	2.0±0.9	2.1±1.0	2.3±1.4
Mean extension pre-Iberian phase (10^6 km^2)	2.1±2.2	2.3±1.5	1.8±1.1	2.0±1,5	2.1±1.7
Mean extension Iberian phase (10^6 km^2)	2.7±2.7	3.6±3.7*	2.2±1.4	2.2±1.7	2.6±2.5
Mean extension post-Iberian phase (10^6 km^2)	1.7±0.8	2.8±1.8**	1.5±0.7*	1.8±1.0	1.9±1.2
Affected Iberian area (10^5 km^2)	1.4±1.1	1.5±1.1	1.6±1.6	0.8±0.9**	1.3±1.2
HWMIe (10^2)	4.1±6.1	4.3±6.2	4.6±6.2	1.7±3.0**	3.6±5.6

Table 4.1 Characteristics (mean and standard deviation) of Iberian HWEs (last column) and regional SOM-based Iberian HWEs (columns two to five). Symbol * (**) indicates

significant differences at $p<0.05$ (0.01) level with respect to climatology. HWMIe is defined in section 2.2.4.

Further analyses indicate an intermonthly variability of Iberian HWEs and HWDs (Figures 4.3 and 4.4 respectively). On the contrary, there are marginal differences between the summer months for other HWE parameters (e.g. the mean Iberian phase duration). The highest total frequency of HWEs (HWDs) for 1979-2017 is found in August (July), while the seasonal minimum occurs in September. The largest trends are found in August for both diagnostics (with +0.48 HWEs decade^{-1}, $p<0.05$ level, and +1.58 HWD decade^{-1}, $p<0.01$), followed by June (+0.38 HWEs decade^{-1} and +0.97 HWD decade^{-1}, $p<0.05$ level). On the opposite, non-significant negative trends are found in September for any diagnostic. In summary, these analyses show that there are more HWEs in the high summer (August) and they also tend to occur more frequently in early summer. The latter implies a shift in the timing of HWEs towards earlier dates.

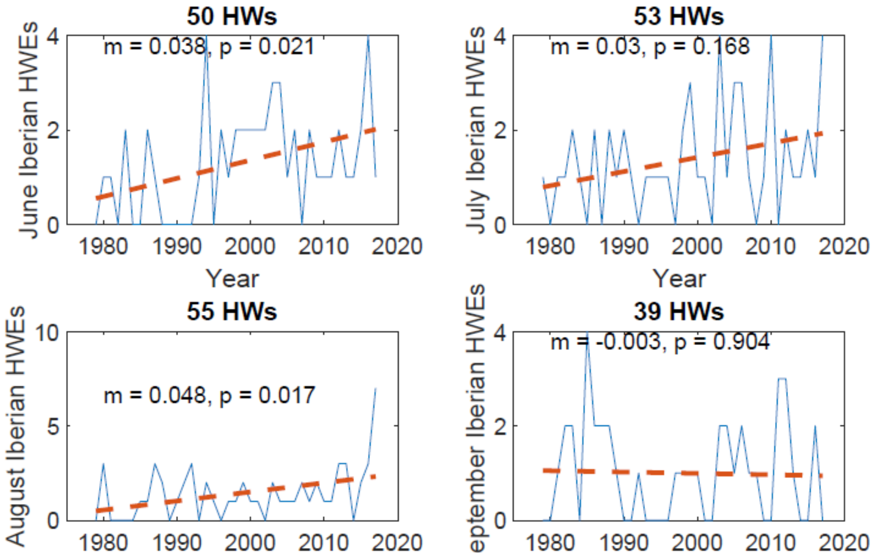

Figure 4.3. Monthly frequency of Iberian HWEs for the 1979-2017 period. June (top left), July (top right), August (bottom left) and September (bottom right). The panels also include their trends (m) and significance (p). The title indicates the total number of events in the corresponding month.

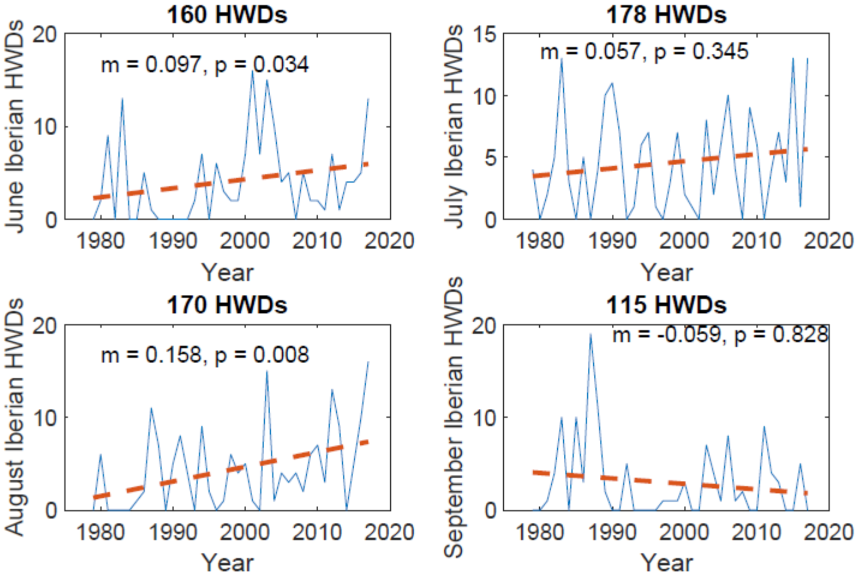

Figure 4.4. Same as Figure 4.3 but for Iberian HWDs.

The spatial distribution of HWEs and HWDs frequencies, and their trends are displayed in Figure 4.5. In addition to the spatial variability, the results evidence spatial differences between HWEs and HWDs. The Cantabrian coast shows the highest number of HWEs (more than 70), but not of HWDs, whose maximum is located in the southwestern region (more than 180). Therefore, HWEs reaching the Cantabrian region are more transient (i.e. HW conditions therein are less persistent) than those affecting southwestern Iberia. The lowest values of both magnitudes are found in the southeast, with ~50 HWs and 120 HWDs. This result may seem surprising. However, we should remind that the temperature threshold depends on the local temperature distributions, and hence a HWD is associated with lower temperatures in northern Iberia than in the southern area. In addition, the total number of temperature exceedances above the selected threshold (Figure A1 in the appendix), show low values in the southeasternmost sector of Iberia, suggesting a reduced variability in the temperature series of that region. Further analyses suggest that temperature exceedances in this region are short-living so tend to not satisfying the duration thresholds (Figure A2 in the appendix). Regarding the spatial trends (right panels of Fig. 4.5), they are significant (p<0.1) for some areas of central eastern Iberia, and there are more regions with significant positive trends in HWEs than in HWDs (in agreement with Fig. 4.1). HWEs and HWDs show a stronger resemblance in their trend patterns than those obtained for frequency, and have a high correspondence with the spatial distribution of T850 trend for the extended summer (see section 1.2).

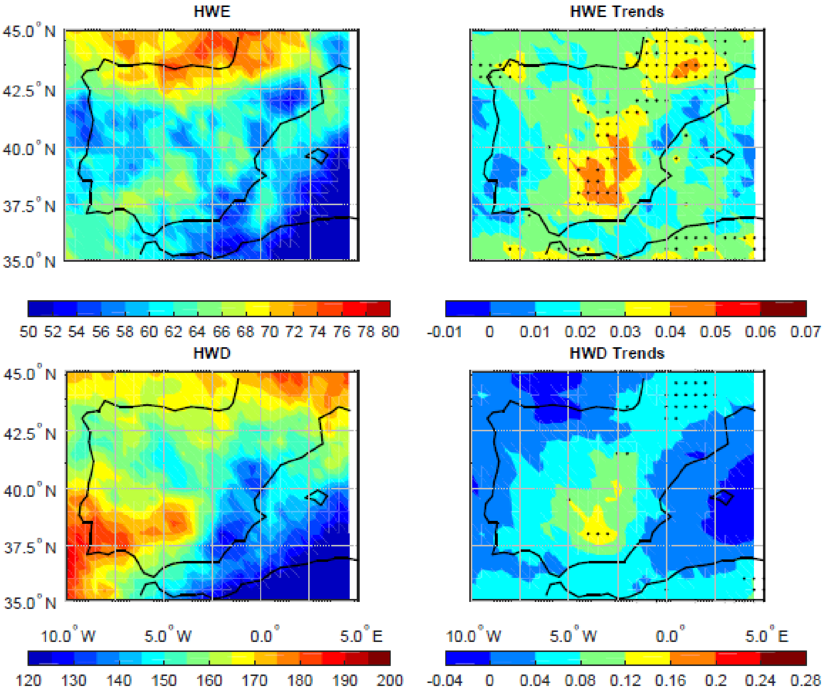

Figure 4.5. Spatial distribution of number (left) of Iberian HWEs (top) and Iberian HWDs (bottom), and their trends (right) for the 1979-2017 period. Dots indicate grid points with significant trends at p<0.1 level.

Next, we exploit the Lagrangian-perspective of the algorithm and describe the tracks of Iberian HWEs. When the full trajectories of all Iberian HWEs are considered together or separately for their different stages (pre-Iberian, Iberian and post-Iberian phases), conclusive results cannot be extracted (Figure A3 in the appendix). The same applies to the spatial distribution of HW centre location of each HWD (Figure A4 in the appendix). Consequently, the analysis of the spatio-temporal evolution is performed from a different perspective, focusing on the full HW patterns, instead of their centres. The spatial frequency of HWDs for the different phases is shown in Figure 4.6. Local frequencies are expressed in percentage of days with respect to the number of Iberian HW patterns that were detected during that period. Figures A5-A6-A7 in the appendix show the daily evolution for different lags within the pre-Iberian, Iberian and post-Iberian phase, respectively. Maximum frequencies are considerably higher for the Iberian phase (~30 %, Fig. 4.6a) than for the other stages of the life-cycle (~15%, Fig 4.6b and 4.6c), indicating more diffuse patterns during the pre- and post-Iberian phases.

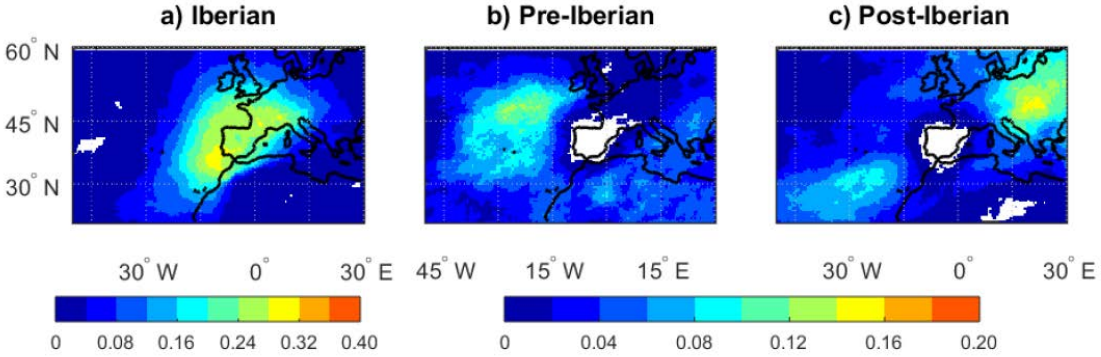

Figure 4.6. Composite of local frequencies (shading, colourbar) for different stages in the HWEs spatio-temporal evolution: a) Iberian, b) pre-Iberian and c) post-Iberian phase. Local frequencies are expressed in ratio with respect to the number of Iberian HW patterns that were detected during that period.

The HWEs already detected in the pre-Iberian phase (Figure 4.6b) are mostly located west of Iberia, although the contribution of other areas surrounding Iberia is not negligible. The majority of HWEs persisted in Iberia less than 3 days (only 91 out of 188 were still detected on d2), and the most persistent ones (d3) tend to affect the rest of western Europe (Figure A6). During the post-Iberian phase, HWEs tend to move towards central Europe or backward to the southwest Atlantic (Figure A7).

The boxplots of the intensity and extension for the different stages of Iberian HWEs only show small (non-significant) differences between them (not shown). Nevertheless, when the daily evolution of these HWE parameters is analysed, some remarkable signatures arise (Figure 4.7). HWEs that already existed on d-4 display higher intensity at that time than the median of the pre-Iberian phase. In the Iberian phase all parameters (intensity, extension, % of affected Iberian area and HWMI) display lower values on d0, growing with time until d3. This behaviour is not observed through the post-Iberian phase and other HWE parameters (not shown) which remain more constant.

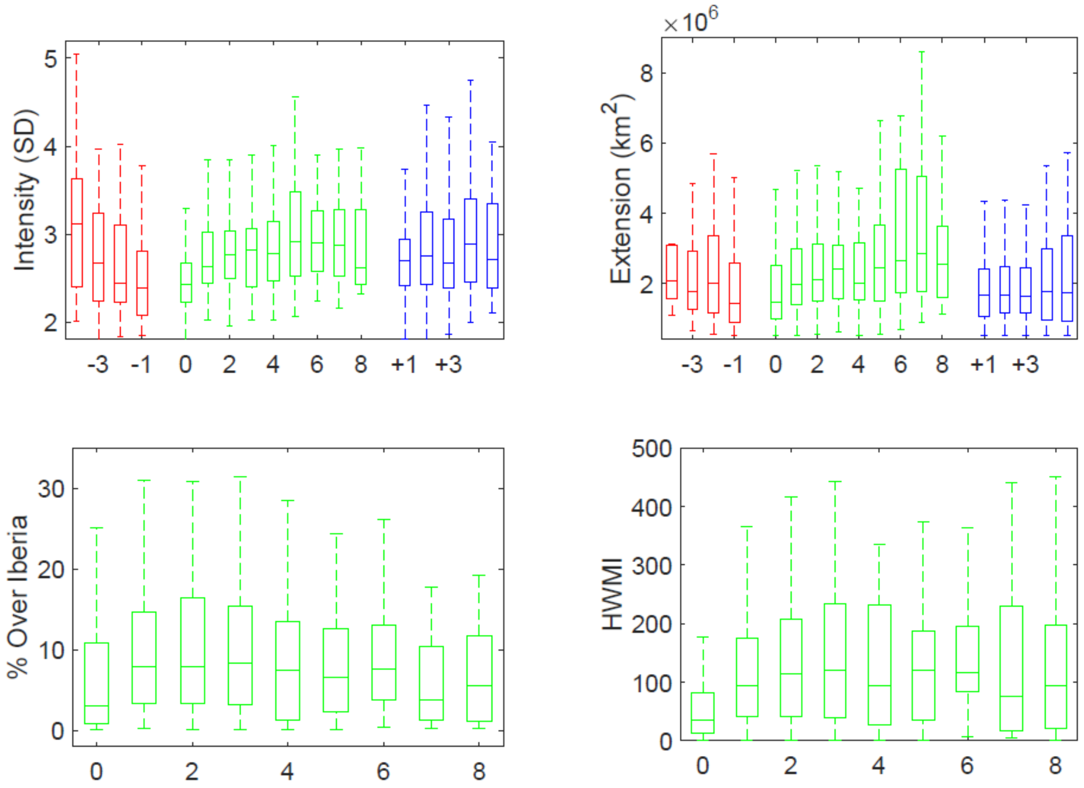

Figure 4.7. (Top) Distributions of intensity (in SD, left) and extension (in km^2, right) of HW patterns for different lags of the pre-Iberian (red boxplots), Iberian (green boxplots), and post-Iberian (blue boxplots) phases. (Bottom) As Top panels but for the percentage of Iberian affected area (in percentage with respect to the total HW pattern area, left), and HWMI (right) for different lags of the Iberian phase. The boxplots extend from the 25th to the 75th percentile, with the median in between, and the whiskers represent the maximum and minimum values.

4.2. Regional patterns

As shown in the previous section, when the spatio-temporal evolution of all Iberian HWEs is considered, preferred tracks do not clearly emerge. This diversity agrees with the large variability of HWEs parameters (Table 4.1) and is also observed in the associated temperature signatures over Iberia (not shown), indicating large variability in the spatial fingerprints of Iberian HWEs. In order to identify regional differences among Iberian HWEs, a SOM-based classification is performed for the 1979-2017 period based on their mean T850 anomaly patterns over Iberia (using only Iberian HWDs, see Section 2.2.2). As Iberian HWEs tend to cause HW conditions over ~20% of the territory, only four clusters are retained (This choice is further supported by a detailed inspection of the results for different numbers of clusters). To explore differences between the Iberian phase of regional HWEs, we composite their daily HW patterns and Z500 fields. Figure 4.8 shows the composites of the relative frequency (expressed in days with respect to the number of HWDs included in the cluster) and Z500 anomalies for the HWDs of each group. Similar analyses are performed for the pre- (Figure 4.9) and post-Iberian (Figure 4.10) phases of each cluster. As happened when all HWEs are considered together, local HW frequencies are considerably higher for the Iberian phase (~60%) than for the remaining stages of the life-cycle (~25-30%, Figures 4.9 and 4.10). The main HW characteristics of each cluster are summarized in Table 4.1 (columns 2 to 5) and their trends in Table 4.2.

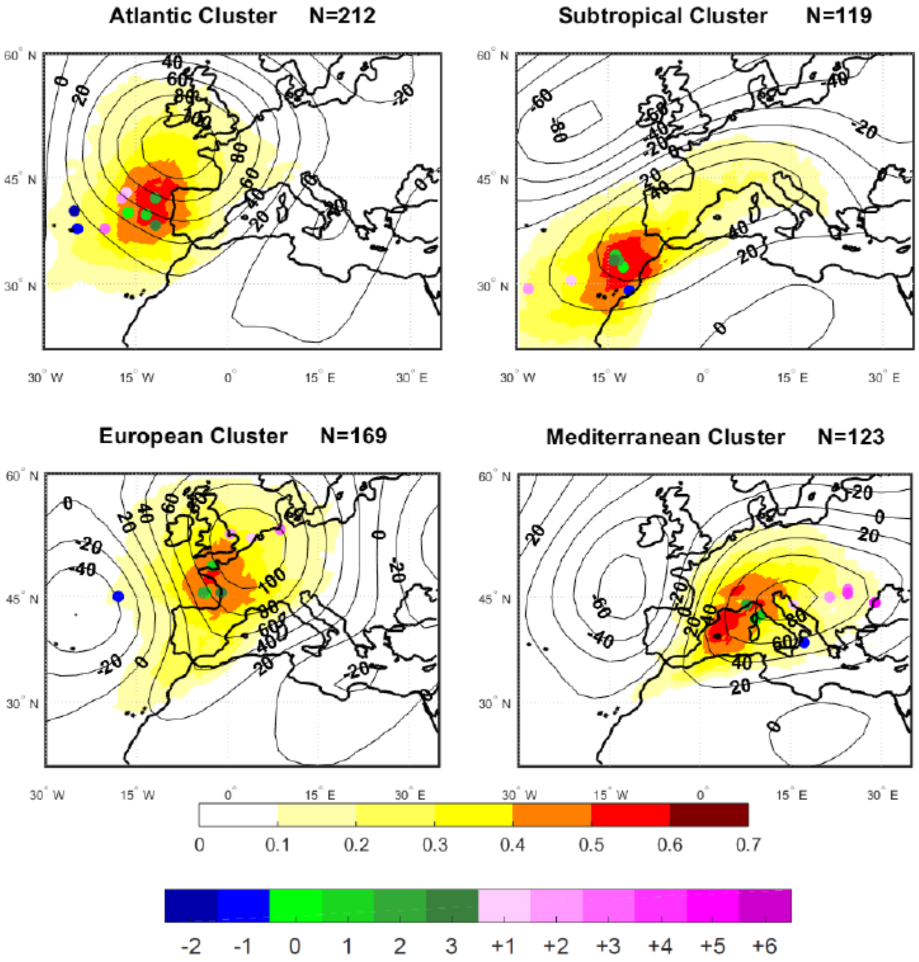

Figure 4.8. Composite of HWD frequency (shading, with respect to the total number of days in the cluster, top colourbar), Z500 anomaly (contours, in m) for the Iberian phase of the 1979-2017 HWEs included in each SOM-based cluster. The number of days included in each composite is indicated. To better illustrate the spatio-temporal evolution, the composite of centre location (dots, bottom colourbar) are shown for different lags of

the Iberian phase (green), as well as for their pre- (blue dots) and post-Iberian (pink) phases.

The first cluster (60 events) affects mainly western Iberia, with the maximum frequency located in the eastern Atlantic (Atlantic events, hereafter), in good agreement with the positive Z500 anomaly centre (Figure 4.8). Non-significant positive trends of HWEs and HWDs are found for the events of this cluster (Table 4.2, first column, see also the spatial distribution of local HWE trends and HWD trends in top left panels of Figures A8 and A9 in the appendix. HWEs of this cluster have characteristics close to the average of all Iberian HWEs. They tend to form in the eastern Atlantic at least one day before affecting Iberia (more than 50% of them exist in the pre-Iberian phase, Figure 4.9, top left panel). In the post-Iberian phase, they weaken and decrease in extension (at the largest rate of all clusters) without a preferred trajectory (Figure 4.10, top left panel).

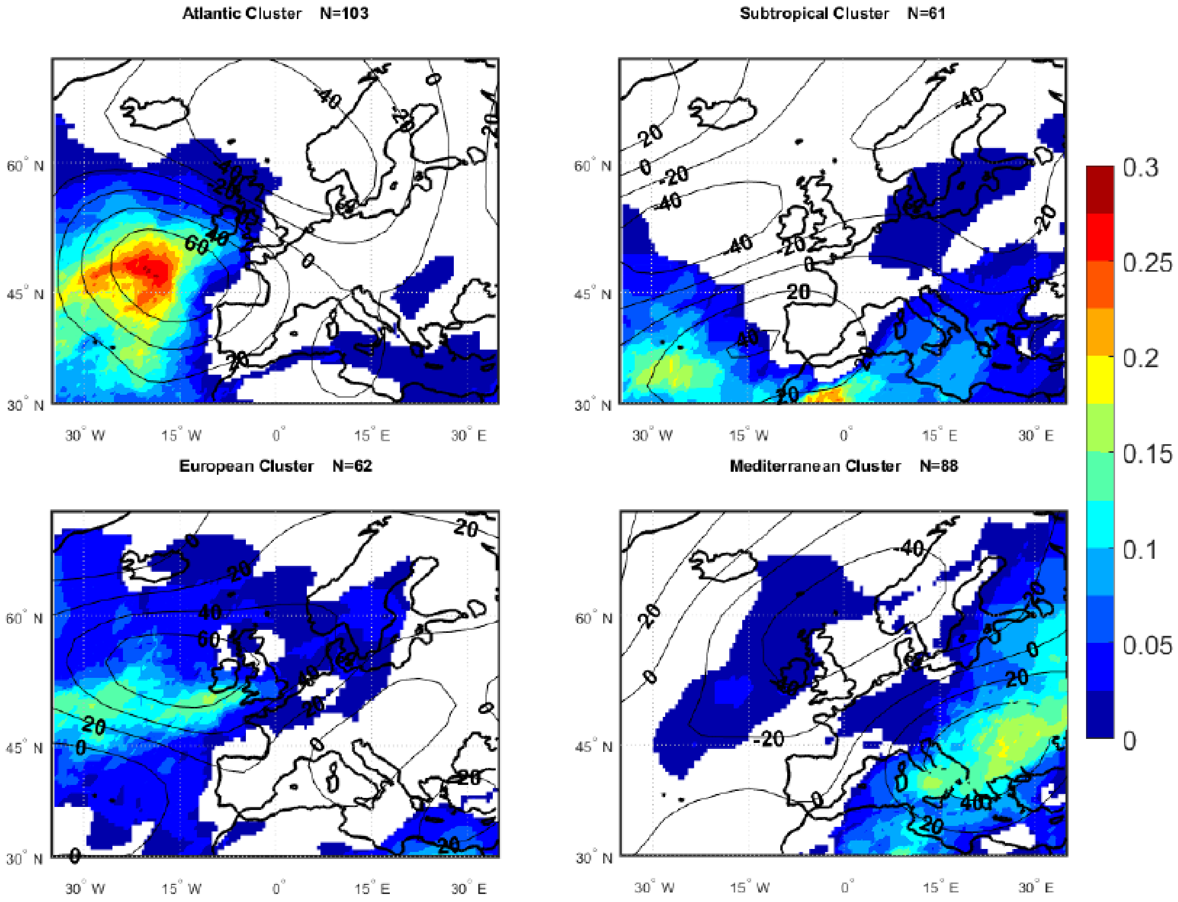

Figure 4.9. As to Figure 4.8 but for the pre-Iberian phase.

HWEs of the second cluster (32 events) have their largest impact over southern Iberia and the HW frequency maximum is located over Morocco (Subtropical events, hereafter, Figure 4.8, top right panel). The Z500 anomaly centre is shifted eastward of the HW maximum and centred over the western Mediterranean, suggesting an important role of advection of warm subtropical air masses. Non-significant trends of HWEs and HWDs are found for this group (Table 4.2). However, some grid points over central Iberia display positive significant trends (at $p<0.1$) in both magnitudes (top right panels of Figures A8 and A9 in the appendix). Subtropical events reach the highest mean extension of all regional Iberian HWEs (significant differences at $p<0.01$), as well as for the Iberian ($p<0.05$) and post-Iberian ($p<0.01$) phases (Table 4.1). In most cases, they originate at least one day before affecting Iberia, when they are located in northern Africa or the subtropical Atlantic (Figure 4.9, top right panel). In the post-Iberian phase, they can persist for long time (even a week), while keeping their large extension ($p<0.01$) and moving to southwest or northeast at a high speed (Figure 4.10, top right panel).

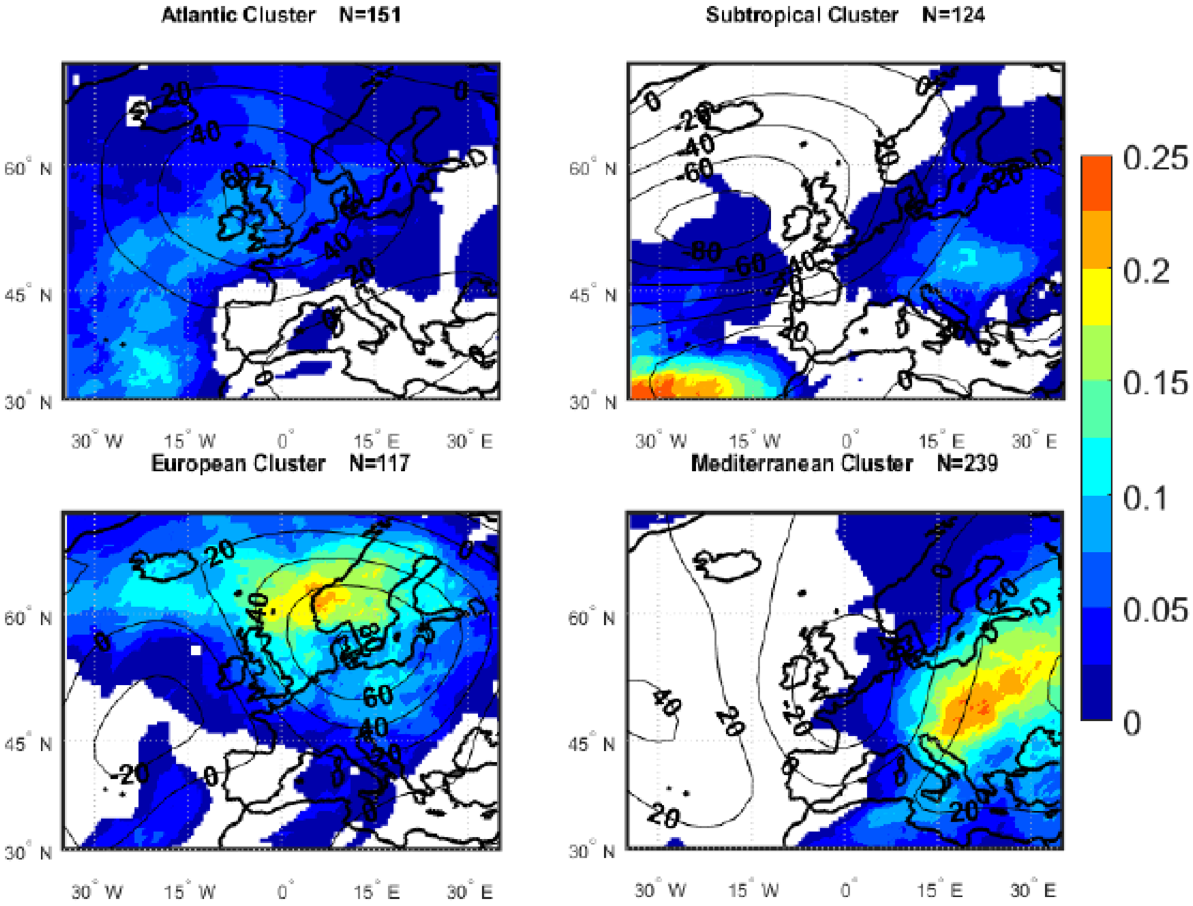

Figure 4.10. As to Figure 4.8 but for the post-Iberian phase.

	Atlantic	Subtropical	European	Mediterranean
Iberian HWEs trend (HWEs decade^{-1})	0.19	0.15	0.08	0.57**
Iberian HWDs trend (HWDs decade^{-1})	0.08	0.39	0.64	1.44**

Table 4.2. Iberian HWEs and HWDs trends of regional SOM-based clusters (columns two to five). ** indicates significant trends at $p<0.01$ level.

The third group (48 events) has the HW and Z500 anomaly patterns centred over western Europe (European events, hereafter, Figure 4.8, bottom left panel). Trends in their frequency of HWEs and HWDs are non-significant (Table 4.2), and the same applies to the spatial distribution of these parameters (bottom left panels of Figures A8 and A9 in the appendix). The area of Iberia affected by these HWEs is the largest of all groups (non-significant, though) hitting mainly its northern side. In addition, they tend to be short-lived, with more than 50% of them affecting Iberia the first day of detection and decaying rapidly in the post-Iberian phase (Figure 4.10, bottom left panel), with the significant lowest duration and extension in this phase ($p<0.05$). During their life-cycle, they tend to move to the east/northeast.

HWEs of the fourth cluster (48 events) are the most transient over Iberia ($p<0.05$), where they persist for only 2.6 days on average, mainly affecting its eastern side (Mediterranean events, hereafter). This group is dominated by a Z500 anomaly dipole favouring warm advection over eastern Iberia from inland (Figure 4.8, bottom right panel). These events display the lowest extension over Iberia and HWMIe ($p<0.01$), which also explains the low number of HWEs and HWDs in this area (Figure 4.5). Nevertheless, this cluster is responsible for most of the HWE and HWD trends in the eastern side of Iberia (bottom right panels of Figures A8 and A9 in the appendix). In fact, this Mediterranean cluster is the only group with significant trends in HWEs and HWDs ($p<0.01$, Table 4.2), explaining more than half of the total Iberian trends shown in Figure 4.1 (57% for both variables) and many of the local trends in Figure 4.5. The Iberian trends are no longer significant when Mediterranean events are removed from the pool of Iberian HWEs. This is the cluster with the lowest number of events already existing in the pre-Iberian phase (33.3%). In this phase, HW conditions are confined to eastern Europe and western Mediterranean (Figure 4.9, bottom right panel). After affecting Iberia, they tend to persist many days (5.0 days on average, $p<0.05$) and evolve eastwards (Figure 4.10, bottom right panel).

4.3. *Associated atmospheric circulation*

In this section, we explore the atmospheric circulation patterns associated with Iberian HWEs and their regional events. To do so, we employ the catalogue of WRs obtained from the SOM algorithm (Section 2.2.2), which classifies the atmospheric flow of each day in one of the four recurrent WRs shown in Figure 2.2. From a climatological viewpoint, all WRs occur with similar frequencies (around 25%, Figure 4.11, inner ring). However, when considering only Iberian HWDs there is a clear predominance of WR4. More specifically, 57% of Iberian HWDs occur under this WR (Figure 4.11, second ring), which is more than double the climatological frequency. The other WRs experience a clear reduction during Iberian HWDs, as compared with their climatological frequencies. Interestingly, the frequency of WR4 is considerably reduced for the pre- and post-Iberian phases in comparison with the Iberian phase frequency (Figure 4.11, fourth and outer ring).

This analysis is also applied to the Iberian HWDs of each cluster of Section 4.2. separately (Figure 4.12). For all clusters, the results are similar to those obtained when Iberian HWEs are considered all together: the four types of regional events are preferentially associated with WR4 during the Iberian phase. This is because during this stage all events tend to concentrate over a relatively small region (Iberia) so that their associated circulation anomalies are indistinguishable from the larger scale perspective of the WRs. Nevertheless, when we consider the pre- and post-Iberian phases we find differences among the preferred WRs of each cluster: WR1 is the dominant precursor of Atlantic events; Subtropical events are preferentially preceded by either WR1 or WR4; WR3 shows a clear predominance during the pre-Iberian phase of European events; Mediterranean events tend to be preceded by WR2. These results indicate that different WRs or combinations of WRs are involved through the life-cycle of regional Iberian

HWEs. This stresses the importance of assessing simultaneously the occurrence of all WRs during a given time interval.

To deep further in this issue, we explore whether WRs have some skill to anticipate the frequency of regional Iberian HWEs on seasonal scales. To do so, we apply a stepwise regression model (Wilks, 2011) for each type of Iberian HWs over 1979-2017, using the corresponding seasonal frequency of Iberian HWDs as a predictand and the extended summer frequencies of the four WRs as predictors. The stepwise regression proceeds forwards and backwards (adding and removing predictors), retaining only those predictors (if any) that improve significantly ($p<0.05$) the explained variance of the predictand. The method identifies different significant predictors for all types of regional HWEs (Table 4.3), with the exception of Subtropical events (which are therefore omitted in Table 4.3). The lack of a skilful model for subtropical events suggests that the atmospheric circulation characteristic of these events does not fit well into any WR. Consequently, from a seasonal WR perspective, the predictability of Iberian HWEs varies with the type of regional event. Overall, an enhanced frequency of WR4 favours Atlantic and European events, while Mediterranean (Atlantic) HWEs tend to be more frequent during extended summers with reduced frequencies of WR1 and WR3 (WR2).

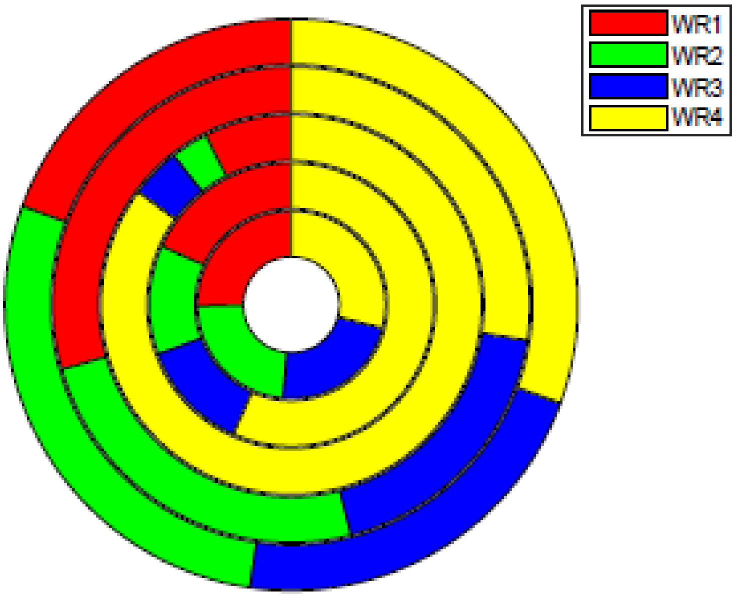

Figure 4.11. WRs frequency for (from inside to outside): all summer days; all Iberian HWDs; HWDs of the top 10 Iberian HWEs; HWDs of the pre-Iberian phase; HWDs of the post-Iberian phase. Colours identify the WRs.

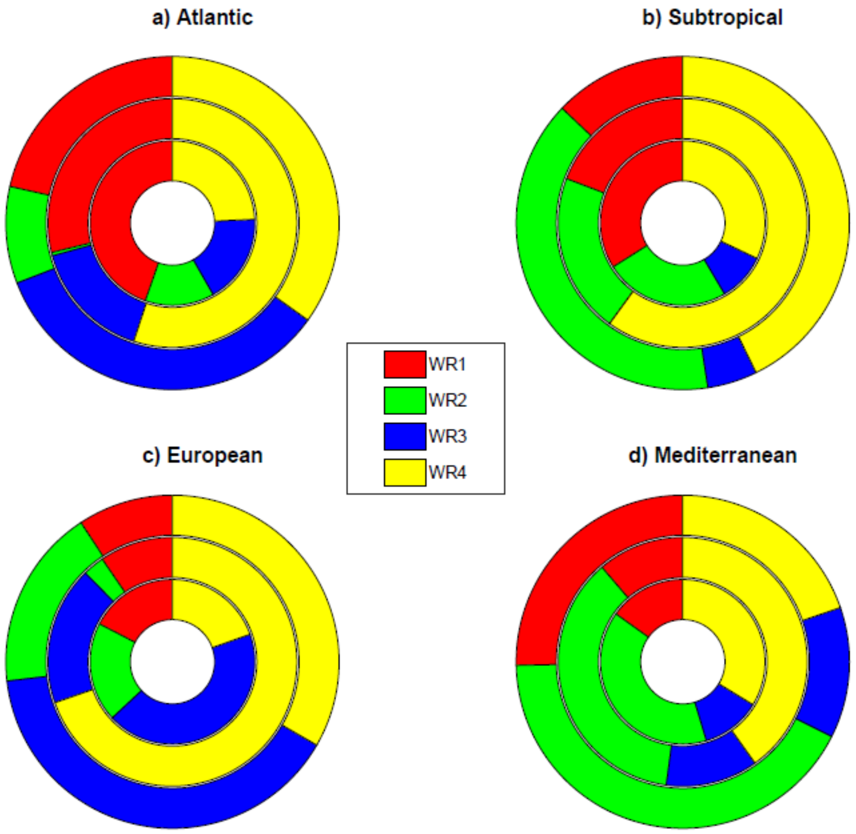

Figure 4.12. WRs frequencies for: a) Atlantic; b) Subtropical; c) European; d) Mediterranean HWEs in the pre-Iberian (inside), Iberian (middle) and post-Iberian (outside) phases. Colours identify the WRs.

Type of regional Iberian HWE	WR	Coefficient (p-value)	R^2 (p-value)	F-test (p-value)
Atlantic	WR4	0.15±0.05 (<0.01)	0.23 (<0.01)	4.64 (<0.05)
	WR2	-0.13±0.06 (<0.05)		
European	WR4	0.16±0.04 (<0.01)	0.25 (<0.01)	14.00 (<0.01)
Mediterranean	WR1	-0.19±0.05 (<0.01)	0.30 (<0.01)	9.04 (<0.01)
	WR3	-0.10±0.04 (<0.05)		

Table 4.3. Stepwise Regression model (1979-2017) for the extended summer HWD frequency of each type of Iberian regional HWE using the seasonal frequencies of WRs as predictors. Only the types for which a significant regression model is found are displayed. For each type of HWE, columns show the selected predictors, their regression coefficients (with p-values based on a t-test of null coefficients), the coefficient of determination (R^2) of the final regression model (with the p value of the correlation coefficient between the observed and predicted values) and the F-test statistic (with its p-value).

4.4. The contribution of the atmospheric circulation to HWs in a changing climate

In the previous sections the relationship between the atmospheric circulation and HWEs has been qualitatively described. Here we quantify how much of the observed T2m anomaly during Iberian HWDs can be explained by the atmospheric circulation using flow analogues (see section 2.2.3 for methodological details). The Z500 flow analogues were computed over the [30-55ºN, 10ºW-15ºE] region. To take into account the influence of climatological changes, howsoever caused, we reconstructed the T2m anomaly of all Iberian HWEs using flow analogues of the recent past (Table 4.4, first row and last column) and the present (Table 4.4, last row and column) subperiods. This allows inferring how these events could have been in terms of T2m if they would have occurred in the recent past and the present.

	Atlantic	Subtropical	European	Mediterranean	All
% T2m anomaly explained by dynamics 1948-1978	50,7	51,5	48,8	40,5**	48,0
% T2m anomaly explained by dynamics 1979-2017	65,1	60,6	71,1*	60,0	64,0

Table 4.4. % of T2m anomaly explained by the dynamics obtained using flow analogues for the indicated period (see section 2.2.3 for further details) for each SOM-based HWEs cluster (columns two to five) and for all events (last column). Symbol * (**) indicates significant differences at p<0.05 (0.01) level with respect to climatology.

We find that, when HWEs are considered all together (Table 4.4, last column), their associated dynamics, as reproduced by flow analogues of the past and present subperiods, explains more than 40% and 60% of the actual T2m anomaly, respectively. In other words, the same atmospheric circulation causes warmer HWEs in the present than in the past ($p<0.01$). The latter estimate of 60% is close to that obtained when we use contemporaneous flow analogues of each Iberian HWE (i.e. HWEs that occurred in a given subperiod are reconstructed with flow analogues of that subperiod), which was expected, since more than half of the HWEs have occurred in the present subperiod. Accordingly, the dynamics plays a key role in determining the intensity associated with Iberian HWEs. The remaining T2m anomaly should be ascribed to other factors (land-atmosphere feedbacks, SST anomalies, …).

Similar results are obtained for all types of SOM-based Iberian HWEs (last row of Tables 4.4). In all cases, the present-day dynamics explains more than 50% of the actual T2m anomaly, which is warmer than what would have occurred in the recent past under similar atmospheric circulation conditions ($p<0.01$). The difference between the recent past and present subperiods can be attributed to: (i) thermodynamical changes (e.g. the temperature trend observed in this area; see section 1.2); (ii) dynamical changes (e.g. changes in atmospheric circulation, so that flow conditions associated with present HWEs are better reproduced by present than recent past analogues). The importance of both factors is explored in more detail in Chapter 5, using the June 2017 mega-heat wave as a case study.

4.5. Top 10 HWEs in Iberia

The HWMIe defined in Section 2.2.4. accounts for the intensity, persistence and affected areal extension of HWEs, allowing us to rank them consistently. Here we use the HWMIe to identify the top ten Iberian HWEs of the analysed period (1979-2017). Their main characteristics are shown in Table 4.5. In addition, Figure 4.13 shows their spatial signatures in terms of total HWD frequency. As compared to the bulk of HWEs, these top events are associated with strengthened anticyclonic conditions, since the frequency of WR4 during these events increases from 57% to 85% (Figure 4.11, third ring). Another distinctive feature of these events is their duration over Iberia (rather than their total duration), which exceeds one week in most of the cases, thus doubling the mean duration of all Iberian HWEs.

Start Date	Duration (days)	Mean Longitude (ºE)	Mean Latitude (ªN)	Iberian phase (days)	HWMIe (10^3)	Type of regional Iberian HWE
30/7/2003	16	353,8	43,0	16	3.22	Atlantic
6/9/1987	19	356,9	39,9	18	3.05	Subtropical
11/6/2017	13	357,2	43,3	13	2.90	European
5/9/1988	11	343,2	36,6	6	2.14	Atlantic
4/6/1981	23	329,5	37,0	9	1.94	Atlantic
23/9/1983	7	353,6	43,3	6	1.83	European
19/7/1995	9	355,1	43,7	7	1.71	European
4/9/2016	5	356.3	46.6	4	1.66	European
20/6/2001	7	356,1	41,6	7	1.62	European
17/8/2012	13	18,69	43,2	8	1.62	Mediterranean

Table 4.5. Main characteristics of the top 10 Iberian HWEs of 1979-2017 ranked by their HWMIe value. Columns indicate (from left to right) the start dates, total duration (in days), mean latitude (ºN) and longitude (ºE), both averaged for the total duration, Iberian phase (in days), HWMIe and the type of regional Iberian HWE.

With the exception of the September 1983, which occurred in the late extended summer, and consequently it caused lower absolute temperature values, the listed events correspond to well-known episodes, supporting the performance of the algorithm and HWMIe. The HWE of highest impact in the reanalysis period was the August 2003 event, which has been widely described in the literature (e.g. Garcia-Herrera et al., 2010). Although this event experienced changes in extension and location (see Figure 1.3), it affected most of Iberia (with the exception of the southeastern part, Figure 4.13a) during all days of its life-cycle (16 days). Other well-known events are also included on the list, such as that of June 2017 (Figure 4.13c), which will be analized in detail in the next Chapter, or the September 2016 event (Figure 4.13h), which caused widespread impacts over most of the territory (Zschenderlein et al., 2018).

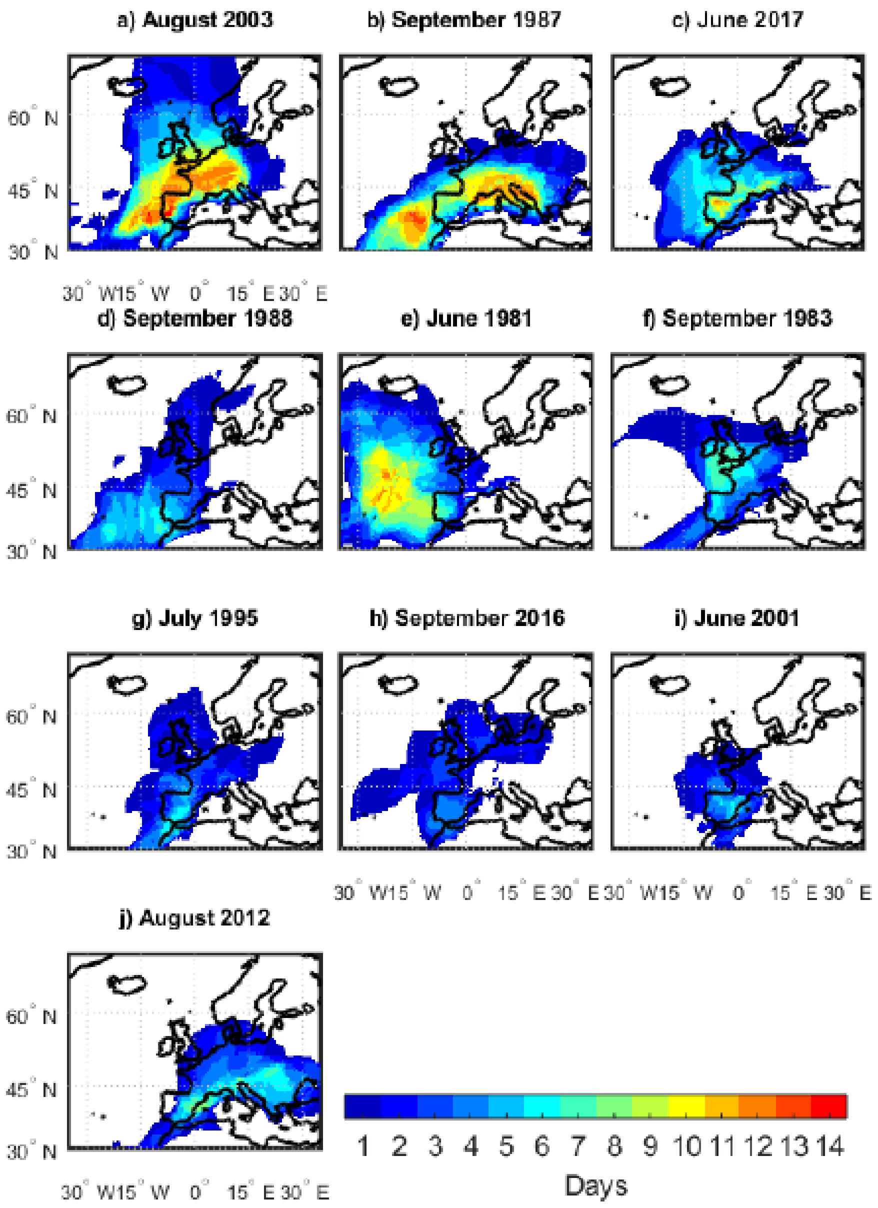

Figure 4.13. Local HWD frequency (in number of days) for the top 10 Iberian HWEs.

According to the SOM-based classification, half of these highest-impact Iberian HWEs are European events, followed by Atlantic events (30%). Interestingly, Subtropical and Mediterranean events are underrepresented on the list, as compared with their climatological frequencies. The impact of the only Mediterranean event in Table 4.5 (August 2012, Figure 4.13j) was confined to northeastern Iberia, but it enters on the list due to its outstanding intensity (locally more than 40 ºC) and duration (eight days over Iberia), thus appearing in the 10th position. The only Subtropical event of Table 4.5 (September 1987, Figure 4.13b) also deviated from the typical behaviour of these events, being the most persistent in Iberia (18 days), and causing local maxima of 12 Iberian HWDs.

Half of the top HWEs have occurred in the 21st century, although the 1980s was also an active decade. Taking advantage of the Lagrangian approach, we can further address how the characteristics of these HWEs could have been in a colder climate. To illustrate this, the top three Iberian HWEs are herein selected, as they have HWMIe values at least 25% larger than the remaining events. For each event, we have applied the analogue method to reconstruct its characteristics (extension, Iberian area, Iberian phase duration and HWMIe) in the same two subperiods employed in Section 4.4, recent past, 1948-1978, and present, 1979-2017 (see Section 2.2.3. for more details). The results are shown in Figure 4.14, with blue and red boxplots representing the distribution for the recent past and present subperiods, respectively. The three events experience significant increases ($p<0.01$) in their present-day characteristics as compared to those inferred for the recent past. Specifically, climate change (herein referred to the differences between the present and past periods) has doubled the areal extent of the most outstanding HWEs (Figure 4.14a), their intensity (HWMIe, Figure 4.14d) and the extension of the affected Iberian regions (Figure 4.14b), also increasing by more than 50% the duration of the Iberian phase (Figure 4.14c).

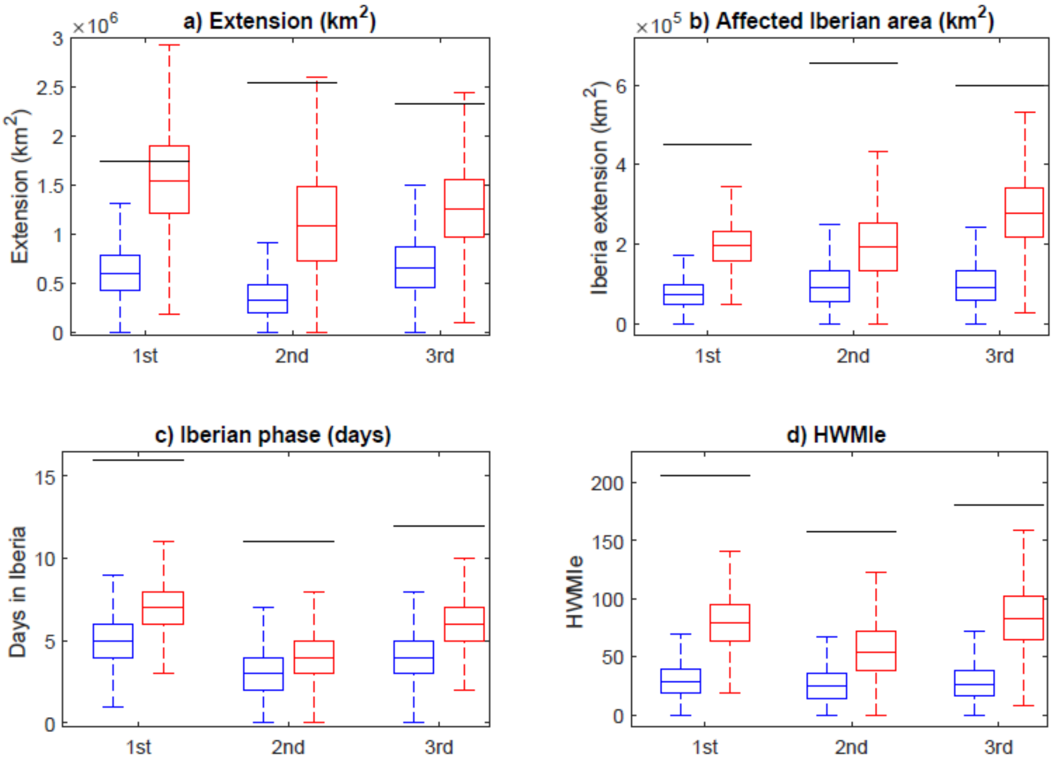

Figure 4.14. Estimated distributions of: a) spatial extension of the HWE (in km^2); b) extension of the affected Iberian area (in km^2); c) Iberian phase (in days) and; d) HWMIe (dimensionless) for the top three Iberian HWEs, as derived from Z500 flow analogues of the past (1948-1978, blue boxplots) and present (1979-2017, red boxplots) subperiods. The boxplot extends from the 25th to the 75th percentile, with the median in between, and the whiskers represent the maximum and minimum values. Black lines represent the actual parameter.

4.6. Comparison between ERA-Interim and NCEP/NCAR reanalysis

In this chapter the new detection algorithm has been applied to data from ERA-Interim reanalysis at 0.5ºx0.5º resolution to derive the catalogue of Iberian HWEs. A remaining question is whether it is robust to changes in the reanalysis and its horizontal resolution. This is addressed in two separated steps: 1) the issue of resolution (by comparing the results from ERA-Interim at 0.5º and 2.5º resolutions); 2) the issue of reanalysis (by comparing ERA-Interim with NCEP/NCAR reanalysis, both at 2.5º resolution).

1.- The low resolution data yields ~20 / 14 % less Iberian HWEs / HWDs than the high resolution version of ERA-Interim (compare Figure 4.15 with Figure 4.1), arguably due to the smoother temperature field in the former. Similarly, the trends in HWEs / HWDs are also reduced by a similar amount (from 0.99 HWEs decade^{-1}/2.54 HWDs decade^{-1} to 0.85 HWEs decade^{-1}/2.00 HWDs decade^{-1}). In spite of this, trends are still significant at $p<0.01$ and $p<0.1$, respectively (compare Figure 4.15 with Figure 4.1). Other analyses, such as the cluster of HWEs retrieves similar regional patterns for both resolutions (compare Figure 4.16 with Figure 4.10), with only small differences in the Subtropical cluster, which is displaced northeastward when a lower resolution is employed. In short, despite an overall reduction in HW frequency, the results presented herein are robust to changes in the horizontal resolution.

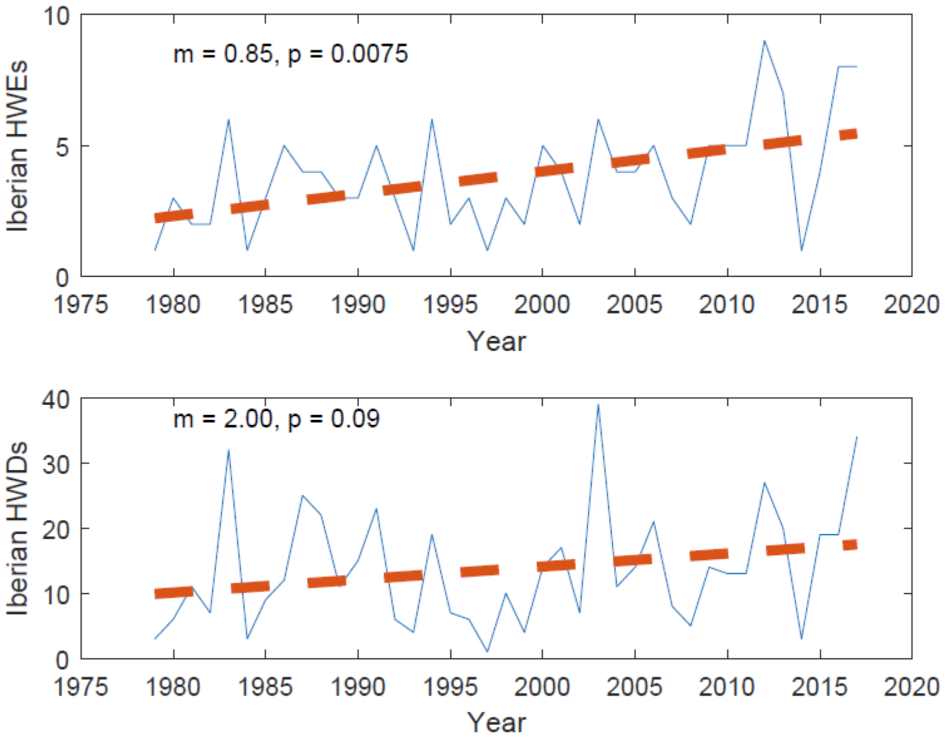

Figure 4.15. As Figure 4.1 but for ERA-Interim reanalysis data at 2.5ºx2.5º resolution.

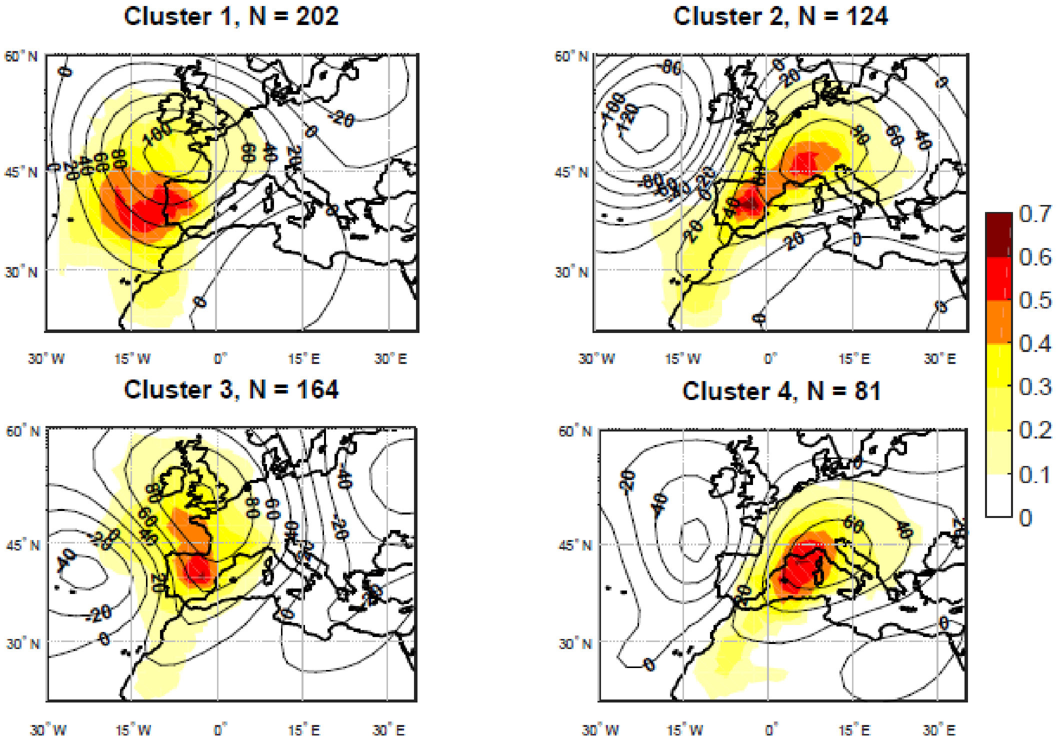

Figure 4.16. As Figure 4.10 but for ERA-Interim reanalysis data at 2.5ºx2.5º resolution.

2.- Regarding the comparison between NCEP/NCAR and ERA-Interim at the same resolution (2.5º), discrepancies should be ascribed to differences in the model and the assimilated data. Figure 4.17 represents the time series of Iberian HWEs and HWDs using NCEP/NCAR, which can be compared with Figure 4.15, where ERA-Interim at the same resolution is used. The climatological frequencies are only slightly lower (of the order of 10%) for NCEP/NCAR than for ERA-Interim, and the correlation coefficients between their time series are 0.75 and 0.9 (significant at $p<0.01$), respectively. The NCEP/NCAR trends for both diagnostics are also significant at the confidence level obtained from ERA-Interim at the same resolution. The spatial patterns of the four clusters of regional Iberian HWEs are also very similar between reanalyses (compare Figure 4.18 with Figure 4.16, noting the change in the order of appearance).

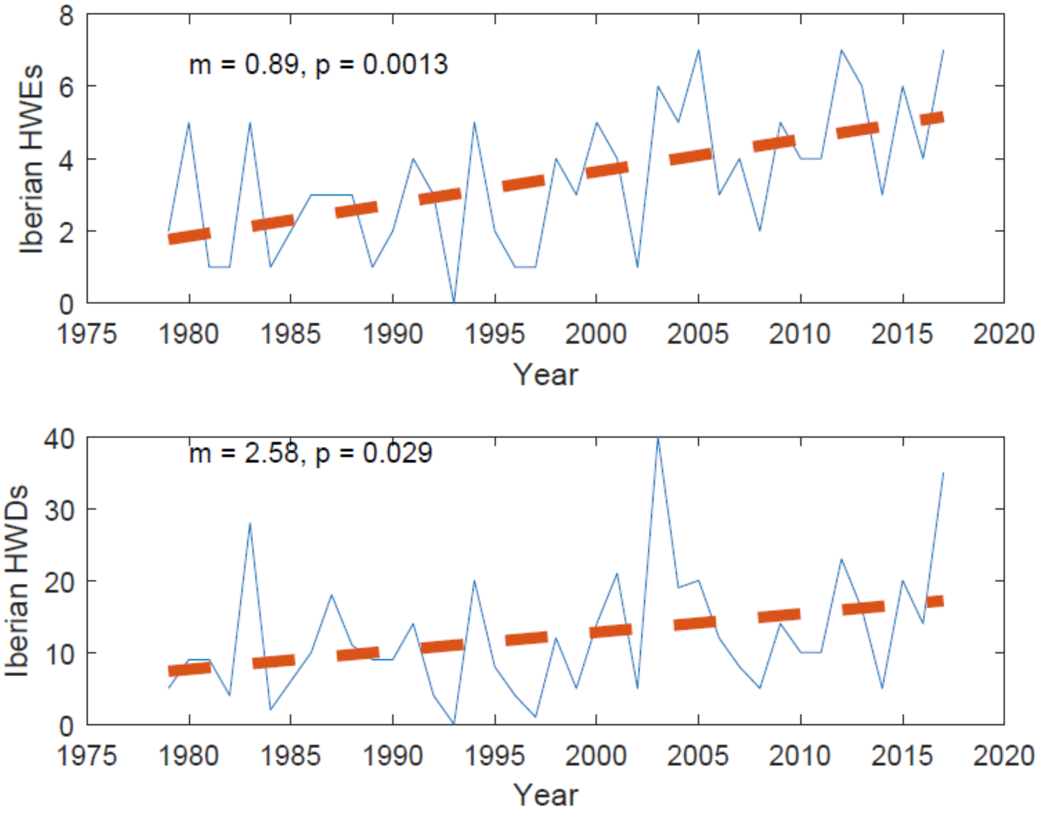

Figure 4.17. As Figure 4.15 but for NCEP/NCAR reanalysis data.

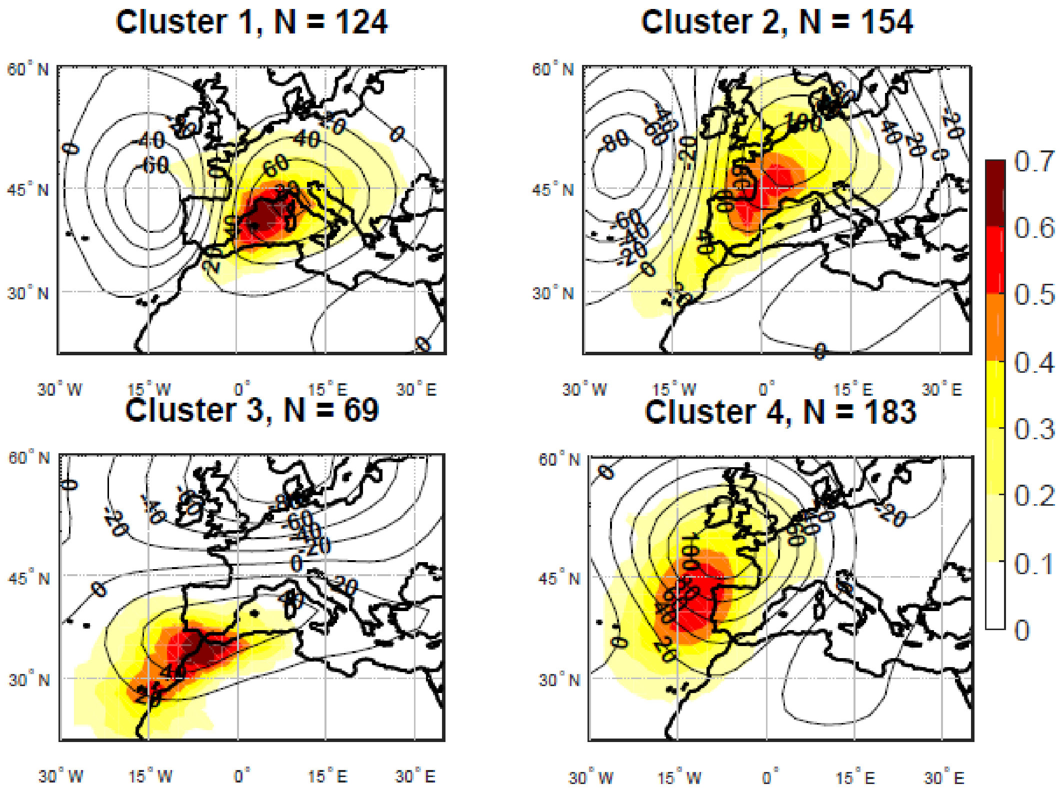

Figure 4.18. As Figure 4.16 but for NCEP/NCAR reanalysis data.

In summary, we conclude that the Iberian HWEs catalogue and its derived results are not substantially affected by the model and horizontal resolution of the reanalysis employed (at least, in what concerns the NCEP/NCAR and ERA-Interim). Interestingly, changes in resolution may cause larger differences than changes in the model. This is arguably due to the large amount of assimilated observations of T850 (and other related fields), as well as its relatively smoothed spatio-temporal variations, which render it a lower dependence on the reanalysis model. This also justifies the use of NCEP/NCAR reanalysis in the following Chapter.

5. June 2017. The Earliest European Summer Mega-heat wave of reanalysis period

In Section 4.1. we reported significant increasing trends of Iberian HWEs and HWDs for both the extended summer and June. This implies that HWEs have become more frequent in the extended summer and have extended to earlier dates. This is in accordance with the earlier summer onset found in Peña-Ortiz et al. (2015) for the last decades. In this context, in Section 4.5, we identified that the June 2017 event was the 3rd most outstanding one in Iberia according to the HWMIe, even when it occurred outside of the high-summer (July and August). Therefore, this event is especially interesting as it could be an actual manifestation of summers that are becoming longer and with an earliest onset. Consequently, a more detailed analysis of this event is performed in this Chapter. To this end, the detection algorithm was applied to data from NCEP/NCAR reanalysis for the 1948-2017 period. This reanalysis is the only one that supplies near real-time data and long time series, which were necessary conditions to assess this HWE in the companion paper to this Chapter (Sánchez-Benítez et al., 2018).

5.1. Description of the event

According to the algorithm, the June 2017 HWE lasted 2 weeks, from 10 to 23 June. Note that there are some differences between the HWE characteristics described here and in Table 4.4, due to the different reanalyses and horizontal resolutions employed in Chapters 5 and 4. However, they are very minor and do not affect the main conclusions of this Chapter. The HWE evolution for different stages of its life-cycle is represented in Figure 5.1. In the onset phase (Figure 5.1a-f), from 10th to 15th June, the event had an extension close to 1,000,000 km^2, affecting Iberia and southern France. The peak of the HWE occurred between 16th and 18th June, when it embraced an area of 4,000,000 km^2, extending to the eastern Atlantic and the European Atlantic seaboard (Figure 5.1g-i). During the decaying phase (19th–23rd June), the event moved northeastward towards central Europe (Figure 5.1j-n). As a whole, the total area under HW conditions was close to 8,000,000 km^2, including western and central Europe and the eastern Atlantic (Figure 5.2). Iberia was the most affected area, with 12 Iberian HWDs, being the longest June

HWE in this area for the reanalysis period (1948-2017). If all the extended summer months are considered, this event was the second longest HWE in Iberia, following that of August 2003 (16 days).

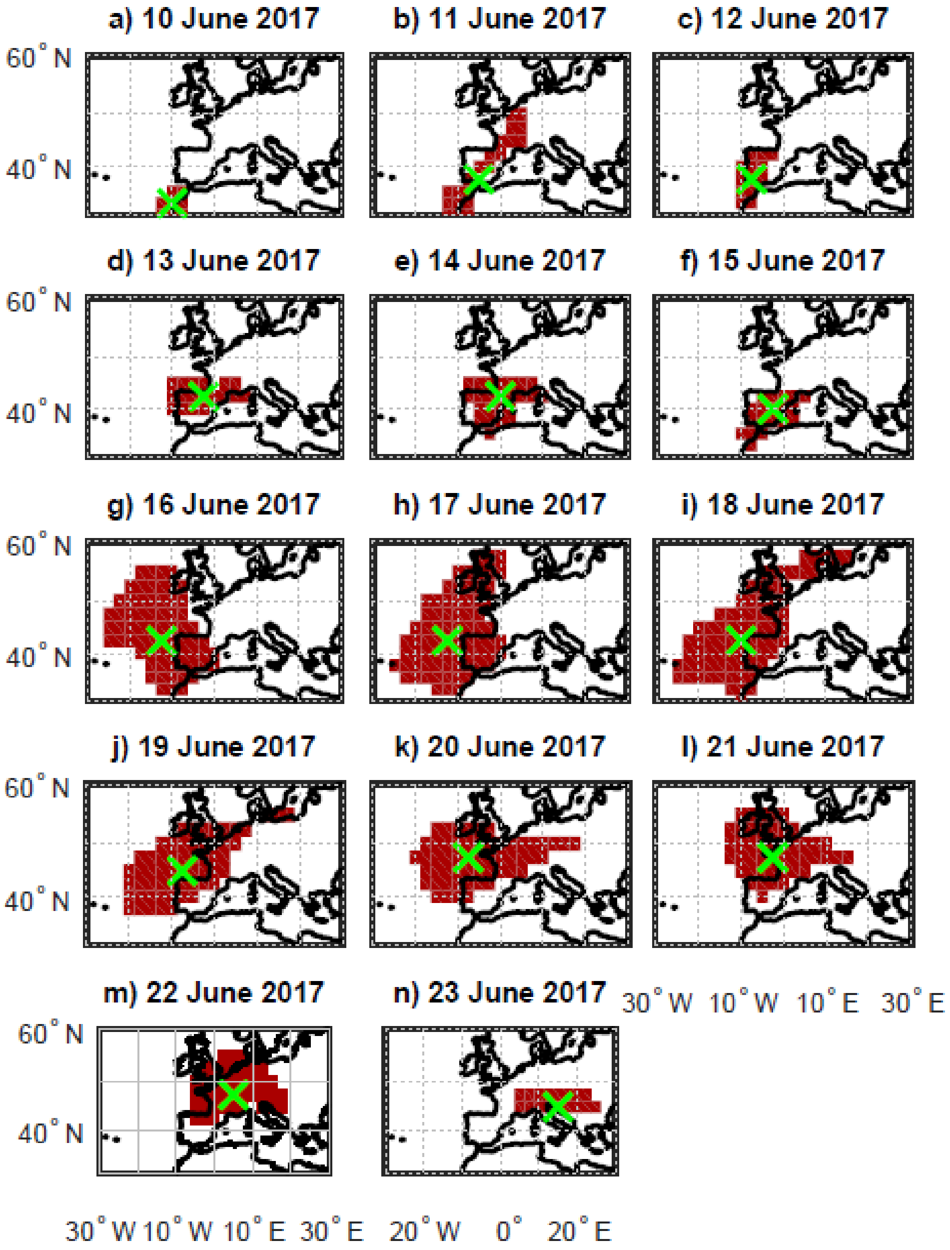

Figure 5.1. Spatio-temporal evolution of the June 2017 HWE. The regions under HW conditions (daily HW patterns) are represented with red shading, with green crosses denoting the corresponding centres.

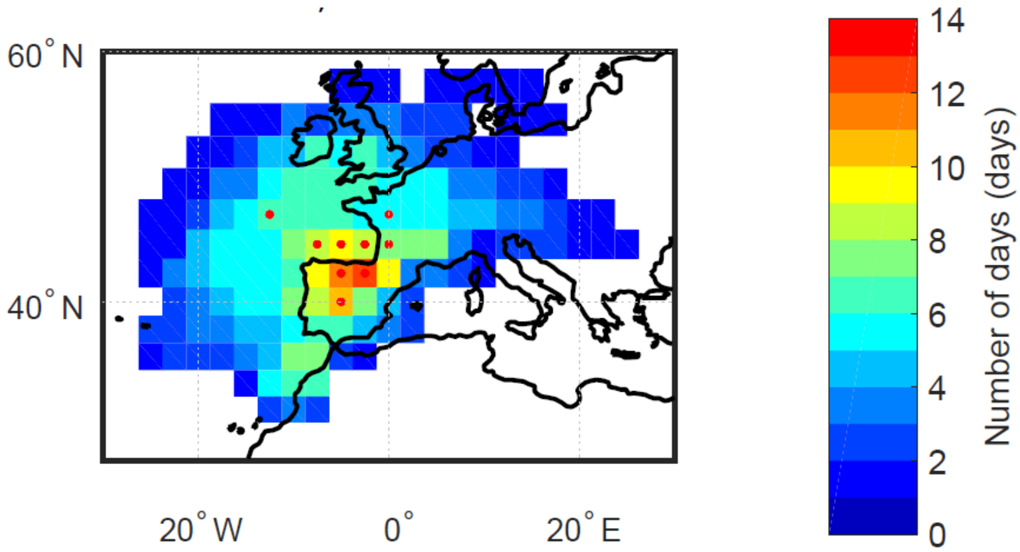

Figure 5.2. Total number of HWDs (shading) for 10–23 June 2017, with red dots indicating regions where the HW persistence was record-breaking for June.

5.2. The earliest European mega-heat wave of the reanalysis period

According to the results of the previous section, the 2017 event fulfilled the mega-heat wave criteria defined by Barriopedro et al., (2011). Therefore, in this section, we further exploit the possibilities of the algorithm and perform an additional validation test, exploring whether it is capable of diagnosing European mega-heat waves, as reported elsewhere. To do so, we have used the list of top summer events described in Russo et al. (2015) for 1950-2015. Our algorithm successfully detects the eleven events that occurred during the top summers included therein (see Table 5.1). This supports that, in addition to synoptic-scale HWEs, the algorithm can also be employed as a tool to characterize mega-heat wave events.

On the other hand, we have compared the characteristics of the 2017 June mega-heat wave with those diagnosed by the algorithm for the aforementioned top European events of the reanalysis period (Table 5.1). Similar to the 2017 mega-heat wave, all considered events displayed extensions above 1,000,000 km^2, durations longer than 7 days and local maximum intensities exceeding 2.5 SDs. However, the June 2017 event was the earliest one of the reanalysis period, not only in Iberia, but also in Europe. It was also exceptional at European scale, as it ranks the 7th strongest European HWE according to the HWMIe index (Table 5.1).

The high-summer character of this June HWE can be verified in Figure 5.3, where the mean Iberian T850 for the 7-day warmest period (14–20 June) is compared with the 7-day mean Iberian T850 distribution for June, July and August. This week was not only the warmest one of all Junes in Iberia but also extreme when compared to the relatively warmer high-summer months, as it falls beyond the 99th percentiles of the weekly T850 distribution in those months.

To further highlight the exceptionally of this event, Figure 5.4 shows the spatial extension of land areas over Iberia with record-breaking T2m throughout 1 April–31 August 2017 at different time-scales. A record-breaking is identified if the corresponding 2017 value was higher than the historical maximum. To compute the historical maximum, we compute running means of T2m for windows ranging between 1 and 91 days and centred on each extended summer day of the 1948–2017 period (e.g., for the 7-day time-scale centred on 15 June 1950, the 12–18 June 1950 interval is averaged). For each grid-point, calendar day, and time-scale, the year with the largest value of the 1948–2016 period is retained as historical maximum.

Start Date	End Date	Year	Affected area	Duration (days)	Extension (10^6 km^2)	Maximum Intensity (SD)	HWMIe
27 June	14 July	1954	Southwestern Russia	18 (2nd)	2.72 (4th)	3.05 (11th)	34.94 (3rd)
17 June	27 June	1969	Norway	11 (8th)	1.68 (12th)	3.50 (6th)	24.59 (8th)
26 June	10 July	1972	Finland	15 (5th)	2.92 (3rd)	4.18 (2nd)	33.16 (5th)
24 June	11 July	1976	United Kingdom	17 (3rd)	2.16 (7th)	3.08 (10th)	34.23 (4th)
24 July	4 August	1994	Benelux	11 (8th)	1.84 (10th)	3.31 (9th)	22.68 (9th)
29 July	14 August	2003	Central Europe	17 (3th)	3.26 (2nd)	3.89 (4th)	35.57 (2nd)
18 June	25 June	2006	Central Europe	8 (12th)	1.83 (11th)	2.51 (12th)	14.86 (12th)
15 July	28 July	2007	Greece	14 (6th)	2.43 (5th)	3.70 (5th)	30.44 (6th)
7 July	25 August	2010	Russia	50 (1st)	3.43 (1st)	4.61 (1st)	107.22 (1st)
2 August	11 August	2014	Scandinavia	10 (11th)	2.10 (9th)	3.49 (7th)	20.02 (11th)
28 June	8 July	2015	Central Europe	11 (8th)	2.22 (6th)	3.33 (8th)	21.75 (10th)
10 June	23 June	2017	Western Europe	14 (6th)	2.10 (8th)	4.06 (3rd)	27.36 (7th)

Table 5.1. Characteristics of the summer mega-heat waves detected by our algorithm for the top eleven summers described by Russo et al. (2015) and the 2017 June event. The following diagnostics (with their rank given in parenthesis) are provided: the duration of the event (in days), the mean areal extension (in 10^6 km^2), the mean intensity (in Standard Deviations, SD, defined as the area-weighted standardized temperature anomaly) and the HWMIe (dimensionless and described in section 2.2.6).

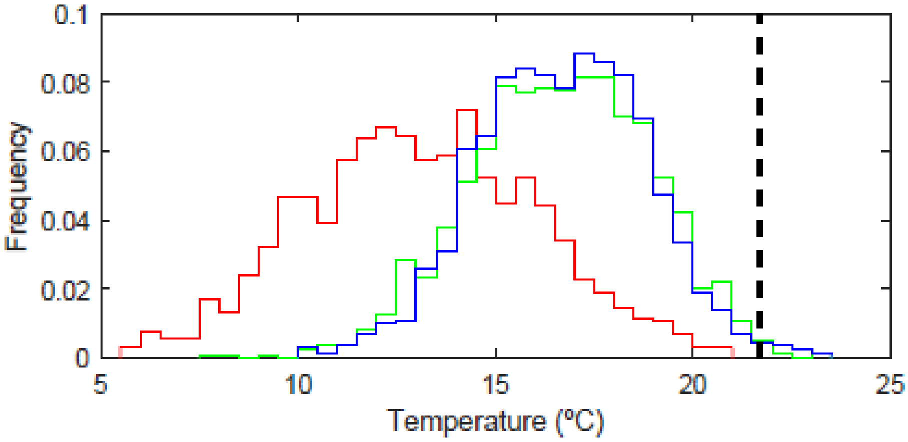

Figure 5.3. Frequency distribution of 7–day mean T850 (in ºC) over Iberia in the reanalysis period for each summer month (June, red line; July green line; August blue line). The black vertical line shows the mean T850 for 14–20 June 2017.

Between May and June, temperature records were broken over almost all Iberia for all analized time-scales. At short time-scales (daily to fortnightly) the record-breaking values reached their maximum extension in mid-June, coinciding with the mega-heat wave period. Longer (monthly to seasonal) periods including the mega-heat wave interval also displayed record-breaking values over Iberia, but they were more widespread before than after the event. In fact, generalized extreme hot conditions already started in spring and ended abruptly by late-June, despite the subsequent occurrence of short warm periods. Thus, the June event can be considered the extreme manifestation of a more persistent warm episode.

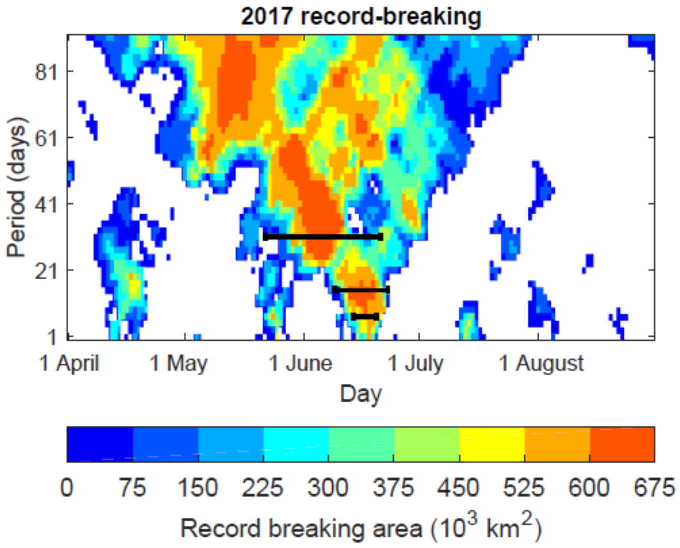

Figure 5.4. Temporal evolution (x-axis) of the spatial extent (in 10^3 km^2) of land areas over Iberia experiencing record-breaking T2m (with respect to the corresponding calendar day of the reanalysis period) on different time-scales (y-axis). Black bars indicate the period of maximum extension for 7–, 15– and 31–day time-scales.

5.3. Atmospheric circulation during the 2017 June mega-heat wave

Figure 5.5 shows the atmospheric conditions for the 7-day peak (similar results are obtained for other time-scales, Figure A10 in the appendix). The Z500 field was dominated by a conspicuous positive anomaly centred over France, with values up to 140 m, which exceeded historical maxima in Iberia and France by up to 30 m. As expected from the results in Section 4.3, all HWDs of this event are associated with WR4 (Figure 2.2). In the same period, some Iberian areas experienced 7-day mean T2m anomalies close to 10 ºC, exceeding the previous records by up to 3 ºC (Figure 5.5). Extreme conditions also extended to regions further north (e.g. western France and southern British Islands), with temperature anomalies close to 5 ºC and exceedances of ~1 ºC above previous maxima. This configuration, with positive T2m anomalies extending from northern Africa to central Europe, suggests a subtropical intrusion of warm air over western Europe. To support this, we computed the mean latitudinal location of different 850 hPa isotherms for the 14–20 June period. We highlight where a record breaking subtropical intrusion occurs (i.e. these isotherms are northern than ever in that calendar days) by comparing the mean latitude observed in the HW peak with the historical maximum mean latitude in the same calendar days of the 1948-2016 period. Figure 5.6 reveals that there was a generalized northward displacement of the isotherms over the eastern Atlantic and western Europe (ca. 10ºW – 15ºE), coinciding with regions of record-breaking T2m (Figure 5.6). The 18–22 ºC isotherms, which are typically located over northern Africa at this time of the year, shifted to Iberia, reaching its northernmost latitude for the reanalysis period, whereas those that are climatologically restricted to central Iberia (~12–13 ºC) were pushed to the British Islands.

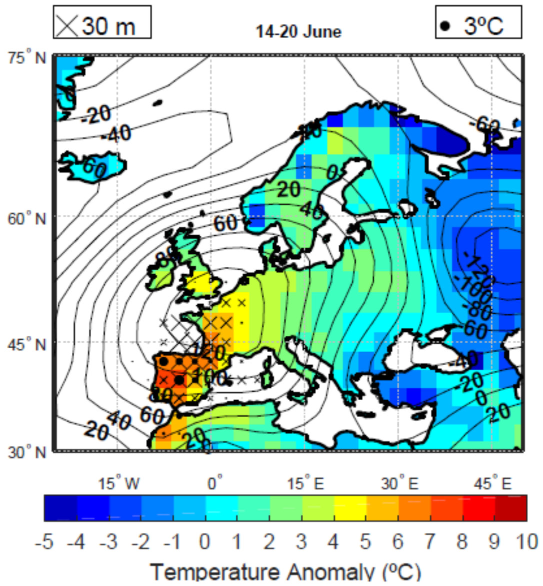

Figure 5.5. Synoptic conditions for the 14–20 June 2017 period. Shading shows the T2m anomalies (in ºC). Contours depict Z500 anomalies (in m). Grid points with record-breaking T2m (Z500) are marked with black dots (crosses), with the size proportional to the exceedance over the previous record.

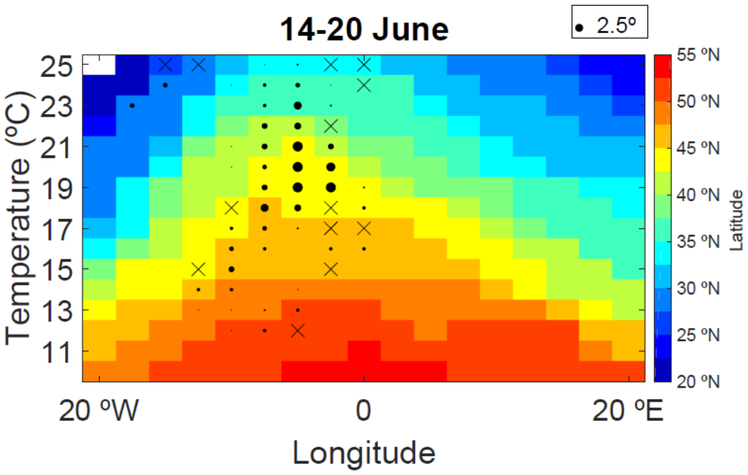

Figure 5.6. Longitudinal distribution (x-axis) of the mean latitude (in ºN, shading) of different 850 hPa isotherms (y-axis) for the period 14–20 June 2017. White colour denotes missing values. Dots (crosses) highlight longitudes where the latitude of the corresponding isotherm was higher than (equal to) the previous record, with the size proportional to the record exceedance.

The temperature pattern, with the warm air mass extending from the south through a narrow longitudinal band, is in agreement with the possible influence of a subtropical ridge. However, the poleward extension of affected areas was so high that this Iberian

HWE was catalogued as a European event, instead of a Subtropical one in Table 4.4. As discussed in Section 1.3, previous European mega-heat waves have also been frequently associated with atmospheric blocking, but recent studies have claimed for an overstatement in these assertions, stressing that some of these events were actually associated with subtropical ridges. To better uncover the nature of the synoptic systems behind the 2017 mega-heat wave, we used the subtropical ridge and blocking detection algorithms described in section 2.2.8. No blocking events were detected during the summer of 2017 over the Euro-Atlantic sector (Figure 5.7), which represents an anomalously low frequency of those episodes. Instead, there was a persistent subtropical ridge in the period 15–21 June over 15ºW–15ºE. As compared to all summer ridges affecting this sector in the 1950–2016 period, this event exhibited a record-breaking duration, equalling to that of 23–29 June 2005 (Table 5.2. shows the top subtropical ridges which lasted at least five days in this sector). The intensity of the subtropical ridge was also exceptional over a large area centred over western France, as revealed by the difference between the mean Z500 field for the 2017 ridge's life-cycle and the corresponding composite of all subtropical ridges of June (Figure 5.8a). In fact, it was locally stronger than the mean value for all subtropical ridges of July (Figure 5.8b) and August (Figure 5.8c). Thus, it could be viewed as a high-summer subtropical ridge occurring earlier than expected.

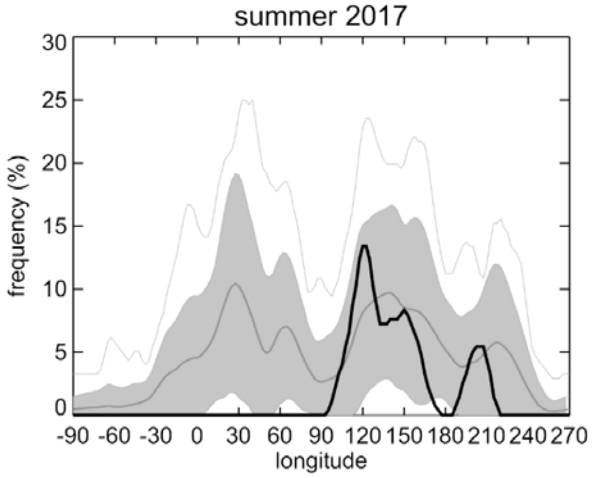

Figure 5.7. Summer (June-to-August) frequency of blocked days (in percentage with respect to the total number of summer days) as a function of the longitude. The thick black (gray) line represents the 2017 (climatological, 1981-2010) frequency. Shading denotes the ±1 SD level and the thin gray line is the 95th percentile of the climatological distribution.

Start day	Duration (days)
15/6/2017	7
23/6/2005	7
12/6/1981	6
26/8/2016	5
29/7/2001	5
13/6/2000	5
4/8/1998	5
12/7/1989	5
12/6/1984	5
17/7/1969	5
17/6/1960	5

Table 5.2. Subtropical ridges which at least lasted five days in the 15ºW-15ºE sector. The table shows their start day and their duration (in days).

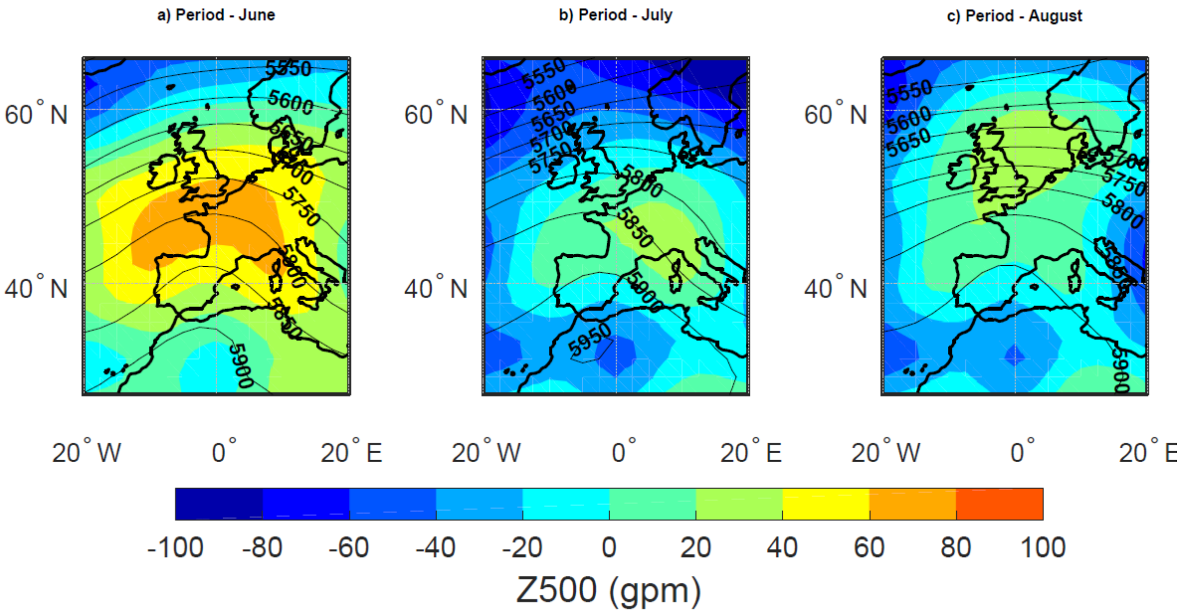

Figure 5.8. Spatial differences of the mean Z500 field (in gpm, shading) for the 15-21 June 2017 period and the composite (in gpm, contours) of all: a) June; b) July; c) August ridges over the 15ºW–15ºE sector.

5.4. Dynamical and thermodynamical contributions to the exceptionality of the event

In Section 4.5., the analogue method was employed to estimate the parameters of the top three Iberian HWEs (including the 2017 mega-heat wave) that could have been expected if similar atmospheric circulation would have occurred in the present and recent past subperiods. It was found that dynamics explained more than 50% of the actual characteristics of the 2017 June mega-heat wave (e.g. areal extent, duration of the Iberian phase, etc.) and that recent changes have contributed to double them (Figure 4.14). In this Section, a novel methodology is assembled to the analogue method in order to separate the contribution of thermodynamical and dynamical changes (see Section 2.2.3 for details). The method is applied to the area-weighted T2m anomaly mean averaged for the 2017 June mega-heat wave period (June 10th to June 23rd), rather than to its parameters, which are addressed in Section 4.5. The assessment is thus more oriented to the associated impacts in terms of T2m, aiming to quantify the role of thermodynamical and dynamical changes in exacerbating the magnitude of the 2017 June mega-heat wave. The Z500 flow analogues were computed over the [30-55ºN, 10ºW-15ºE] region.

The results of the analogue exercise are shown in Figure 5.9. The comparison of the actual T2m anomaly and that reconstructed by present-day analogues emphasizes the key role of the dynamics, which explained more than 50% of the observed T2m anomaly (compare the horizontal line and the orange whisker in Figure 5.9a). On the other hand, there are differences between the analogue-based distributions for the recent past and present subperiods (blue and orange whiskers in Figure 5.9a). In particular, given the atmospheric circulation of the June 2017 mega-heat wave, the associated T2m anomalies are higher now than would have been in the recent past ($p<0.01$). To better illustrate this difference, we have quantified the odds of exceeding a certain T2m anomaly in each distribution, by simply counting the fraction of replicates satisfying that condition. The probability distributions for the recent past and present subperiod are shown in Figure 5.9b with blue and orange lines, respectively. The results indicate that it is very likely that the observed circulation would have caused T2m anomalies above 3 ºC in the recent past and present. However, the probability of experiencing T2m anomalies above 3.5 ºC increases from 0.56 in the recent past to 0.95 in the present (almost a 2-fold increase). Under the same circulation, the chances of exceeding 4 ºC have increased by a factor of 5.

A substantial part of these changes is expected to be thermodynamically driven, since there is a similar difference between the random distributions of each subperiod (Figure 5.9a, pink whiskers), which are not conditioned by the dynamics (i.e. analogues are selected randomly, regardless the atmospheric circulation). In addition, the difference between the median of the analogue-based T2m distributions of both subperiods (~0.7 ºC) is in good agreement with the mean warming of the region (~1.0 ºC), suggesting a main role of thermodynamical changes. However, further analyses suggest a non-negligible influence of dynamical changes. Specifically, Figure 5.10a reveals that the flow analogues of the present subperiod display lower RMSE (with respect to the actual Z500 field) than those of the recent past, and hence present analogues are better replicates than those of the recent past. To better quantify the contribution of dynamical changes to the changes in the T2m distribution, the analogue method is repeated using detrended Z500 and T2m fields, therefore assuming that long-term changes have been thermodynamically forced (e.g., Z500 rise by warming in lower levels; see methodological details in Section 2.2.3.). The difference between the resulting "thermodynamically adjusted" T2m distributions of the two subperiods provides an estimate of dynamical changes (see Figure 5.10c). These distributions become much closer (Figure 5.10b) than the original ones (Figure 5.9a), supporting the major role of thermodynamical changes, whatever the causes of the regional warming are.

The contribution of thermodynamical and dynamical changes is better illustrated in Figure 5.9b. The black line represents the expected probability of occurrence of T2m anomalies in the present period when recent dynamical changes are taken into account alone. Note that its difference with respect to the recent past distribution (blue line) is actually the contribution of dynamical changes estimated in Figure 5.10c. The remaining change (i.e. the difference between the present distribution, shown in orange, and the black line) is attributed to thermodynamical changes. The results indicate that dynamical changes have contributed to increase the probability of moderate T2m anomalies (up to ~3.5 ºC), while thermodynamical trends are largely responsible for the probability increase of the most extreme temperatures. The latter means that the warming effect of thermodynamical changes has been more pronounced in the upper tail of extremes. On the other hand, dynamical changes have mainly contributed to warm weak-moderate extremes at least during atmospheric circulation conditions similar to those observed during the 2017 June mega-heat wave (i.e. subtropical ridges, see Section 5.3). These changes are in agreement with a significant trend in the monthly frequency of subtropical ridge days over this sector for June (Figure 5.11, $p<0.05$).

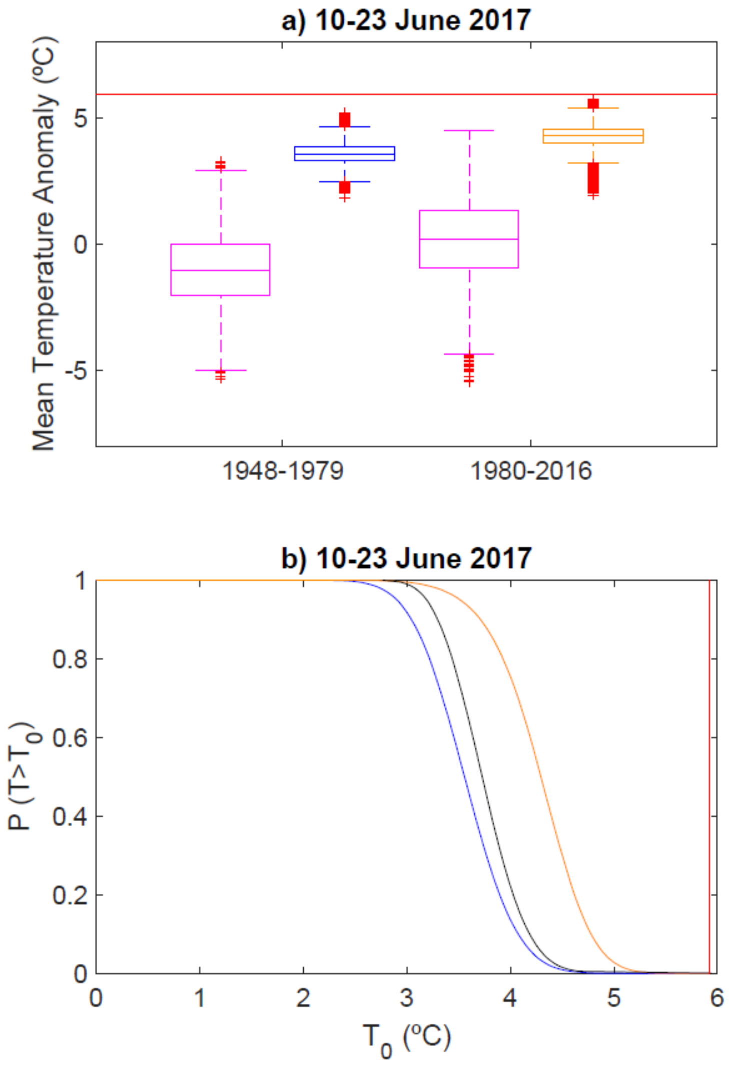

Figure 5.9. a) Distributions of T2m anomalies (in °C) averaged over Iberia for 10–23 June 2017 as derived from random periods (purple boxplots) and Z500 flow analogues (blue and orange boxplots) of the recent past (1948-1979, two left boxplots) and present (1980-2016, two right boxplots) climate; b) Flow-conditioned probability of exceeding a T2m threshold (T_0, x-axis) over Iberia in the recent past (blue) and present (orange) climate. The black line represents the estimated contribution of dynamical changes, after adding the difference between the “thermodynamically adjusted” distributions to the recent past probability. In both panels the red line represents the observed T2m anomaly of the event over Iberia for 10–23 June 2017.

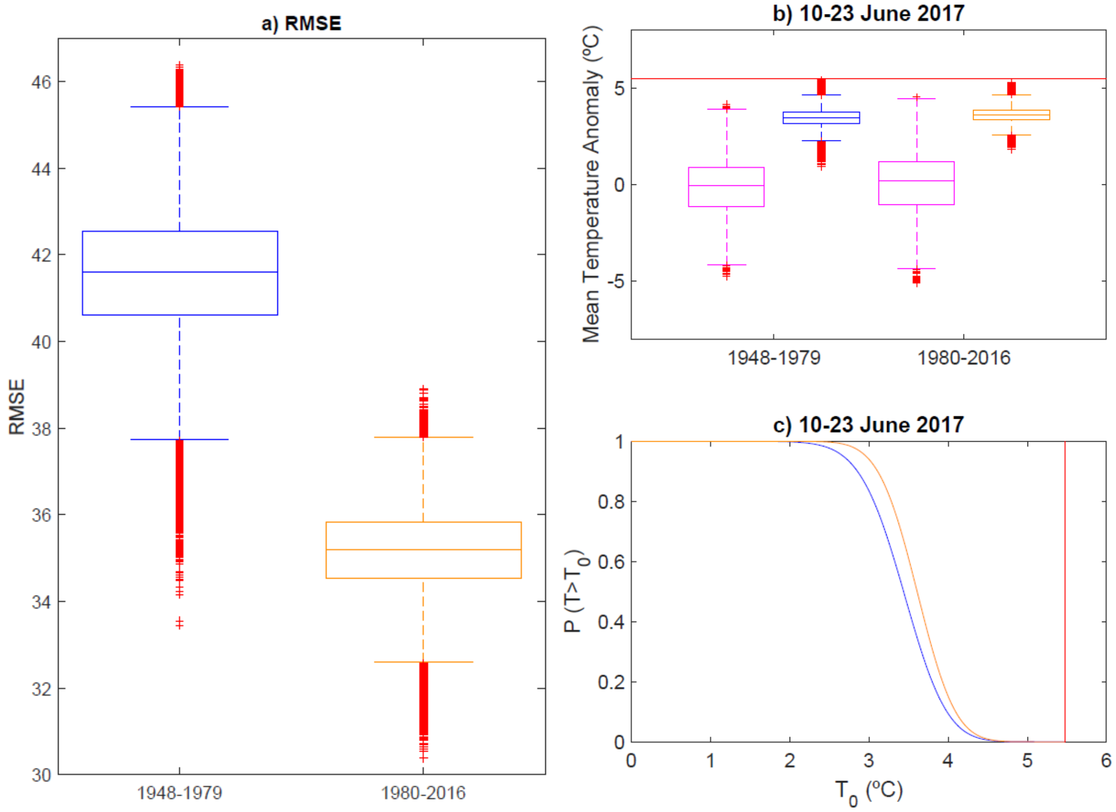

Figure 5.10. a) Root Mean Square Error (RMSE, in gpm) for Z500 flow analogues of the recent past (1948-1979, blue bloxplot) and present (1980-2016, orange boxplot) subperiod; b) and c) As Figure 5.9a and 5.9b but for the thermodynamically adjusted fields.

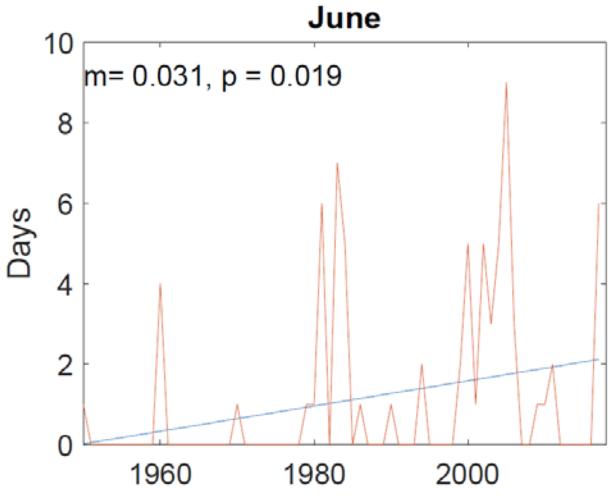

Figure 5.11. Monthly frequency of June days with subtropical ridges over the Atlantic sector for the 1950-2017 period. The figure also includes its trend (m) and its significance (p).

6. Conclusions

In this work, a new paradigm in the assessment of heat waves (HWs) is presented (Chapter 3). To do so, we designed a novel Lagrangian-inspired detection algorithm that changes the focus from the local perspective of Eulerian approaches to the spatial structure of temperature extremes. This new approach emphasizes the heat wave pattern and the follow-up of its spatio-temporal evolution, allowing us to study the life-cycle of heat wave events (HWEs) and the connection with synoptic weather patterns. It is based on percentiles of the local temperature distribution only, with additional criteria for spatial extension, and temporal persistence. The detection algorithm comprises two phases. First, it identifies daily HW patterns as an aggrupation of relatively close (less than 750 km) local extremes (temperature at 850 hPa values above a local time-varying 95th percentile) with an areal extent of at least 500,000 km^2. In a second stage, the spatio-temporal evolution of daily HW patterns is tracked in order to identify HWEs. To consider a daily HW pattern on day d+1 the continuation of another one detected on day d, either one of the two following conditions must be satisfied: a) their areas overlap more than 50% (quasi-stationary HW patterns); b) there is some overlap and the distance between their centres is lower than 1,000 km (transient HW patterns). If more than two HW patterns meet the previous criterion those with the largest overlapping are selected. Finally, a HWE is defined as a HW pattern persisting for at least 4 consecutive days. HWEs are characterized in terms of associated parameters (spatial extension, duration, intensity, trajectory, etc.). The selected thresholds are consistent with the synoptic scale and the algorithm performance and it sensitivity to small changes in these thresholds was tested. This algorithm can be applied to any region and climate realm.

In this work this algorithm has been used to derive a catalogue and climatology of Iberian HWEs for the extended summer season (June-to-September) using data of the ERA-Interim reanalysis with a 0.5º x 0.5º resolution and for the 1979-2017 period (Chapter 4). In addition, the algorithm has been successfully employed for the characterization of European mega-heat waves, including the recent June 2017 event, which is described in detail in Chapter 5. The results are robust to changes in the resolution and reanalysis, and allow us to answer the open questions posed in Chapter 1:

1. We report a mean frequency of about five Iberian HWEs per year, leading to 16 summer days with HW conditions over Iberia (Iberian heat wave days, HWDs). The analysis of the life-cycle of HWEs revealed that they are relatively long-lived, with a mean duration of 8.6 days. However, they only affected Iberia for 3.3 days on average, leading to short-lived HW conditions on local scales. Although Iberian HWEs are transient and spend most of their life-cycle elsewhere, more than half of them developed in Iberia, pointing it as a preferred region for the build-up of synoptic HWEs. Using an event-oriented diagnostic (Heat Wave Magnitude Index Event, HWMIe) that integrates the spatial extent, intensity and persistence of HWEs, we also identify the top ten Iberian HWEs for the 1979-2017 period, which were characterized by enhanced persistence and intensity, as compared to all Iberian HWEs.

2. Iberian HWEs have strong regional signatures, rarely affecting the entire Peninsula. Indeed, the land area under HW conditions is ~20% of Iberia on average. Although there is large variability among events, a clusterization of their mean temperature anomaly patterns yielded four groups with distinctive regional signatures and some characteristic HWE parameters. Overall, these clusters represent Atlantic, Subtropical, European and Mediterranean events that cause HW conditions over western, southern, northern and eastern Iberia, respectively. The Atlantic cluster includes the highest number of events of all groups, and highlights by a characteristic northeastward path in the pre-Iberian phase. The Subtropical cluster tends to originate in northern Africa and embraces the lowest number of events, but with the largest extension. The European cluster mostly includes events that formed in Iberia, thus affecting the largest surface of the territory, and decayed rapidly while moving northeastwards. HWEs belonging to the Mediterranean cluster are the most transient ones over Iberia, and show the lowest extension and intensity in this phase, but also the highest persistence in the post-Iberian phase, when they move eastwards growing in intensity and extension.

3. Iberian HWEs are associated with anomalous atmospheric circulation characterized mostly by a conspicuous positive Z500 anomaly aloft. The analysis of daily weather regimes (WRs) during Iberian HWDs revealed a clear predominance of WR4 (dominated by positive Z500 anomalies over western Europe), whose frequency of occurrence doubles as compared to climatology. Similar results are obtained for the regional groups of Iberian HWEs, indicating that the same WR can instigate HW conditions in different and relatively close areas depending on small changes in the

synoptic configuration. However, as HWEs of each cluster display distinctive features and trajectories through their life-cycle, we report differences among the preferred WRs for the pre- and post-Iberian phases. WR1 is a characteristic precursor of Atlantic and Subtropical events, while WR2 and WR3 preferentially precede Mediterranean and European events, respectively. On seasonal scales, regression models yielded significant relationships between the seasonal frequencies of WRs and regional Iberian HWDs, exception made for Subtropical events. The skill of WRs is relatively low (below 30% of explained variance) but could be improved by exploring other potential predictors of Iberian HWEs (e.g. soil moisture, sea surface temperatures, etc.). These results could be applied to seasonal forecasts of these predictors to infer the Iberian areas that are expected to be most affected by HWEs over the extended summer.

4. The long-term assessment of all events revealed significant trends in the frequency of Iberian HWEs (+1.0 HWE decade-1) and HWDs (+2.6 HWDs decade-1) for 1979-2017. We also found a slight tendency for these events to be more transient although this trend is non-significant. This unexpected result is explained by the significant increase of HWEs with parameters close to the imposed thresholds. Indeed, these characteristics are typical of Mediterranean events, whose increase explains most of the trends in Iberian HWEs, while contributing to lower current mean Iberian HWE parameters. In the absence of regional warming, these “edge-emerging” events would arguably not have been detected as HWEs. The Iberian HWEs and HWDs trends are in agreement with the recent warming. An additional flow analogue exercise of the three most outstanding Iberian HWEs, also unveils that recent warming has contributed to double some of their signatures (spatial extension, HWMIe), making these events more exceptional than they would have been in the past.

5. This method has been applied to the June 2017 event, which is also used as a case study to test the performance of the algorithm for the diagnosis of mega-heat waves. The event displayed typical signatures of European mega-heat waves (long duration, wide affected areas and outstanding intensity), being among the ten strongest events of the reanalysis period. However, the advanced timing was the most prominent feature of this event, as it was the earliest mega-heat wave in Europe since at least the mid twentieth century, causing absolute temperatures typical of high summer HWEs and record-breaking values on different regions and time scales. The atmospheric circulation, characterized by a high summer - like subtropical ridge, was largely responsible for the

observed temperature anomalies. However, the observed circulation caused higher temperatures in Iberia than those expected from past analogues. The difference is shown to be due to recent changes in dynamics and thermodynamics. A novel approach has been designed and assembled into the analogue method in order to quantify the role of dynamical and thermodynamical changes in exacerbating the magnitude of HWEs. The latter were more important in explaining the exceptional temperatures during the June 2017 HWE (i.e. the probability of occurrence of the most extreme temperatures), and very likely made this two-week event at least ~0.7ºC warmer on average. Nevertheless, dynamical changes were not negligible, rising the probability of occurrence of moderate temperature anomalies.

References

Acero, F.J., Fernández-Fernández, M.I., Sánchez Carrasco, V.M., Parey, S., Hoang, T.T.H., Dacunha-Castelle, D., García, J.A., 2018. Changes in heat wave characteristics over Extremadura (SW Spain). Theor. Appl. Climatol. 133, 605–617. https://doi.org/10.1007/s00704-017-2210-x

AEMET, 2018. Olas de Calor en España desde 1975. http://www.aemet.es/documentos/es/conocermas/recursos_en_linea/publicaciones_y_estudios/estudios/Olas_calor/Olas_Calor_ActualizacionOctubre2018.pdf (accesed 1 April 2019).

Ahmad, I., Tang, D., Wang, T., Wang, M., Wagan, B., 2015. Precipitation trends over Time using Mann-Kendall and Spearman's rho Tests in Swat River Basin, Pakistan. Adv. Meteorol. 2015. https://doi.org/10.1155/2015/431860

Allan, R.P., Soden, B.J., 2008. Atmospheric Warming and the Amplification of Precipitation Extremes. Science (80-.). 321, 1481–1484. https://doi.org/10.1126/SCIENCE.1160787

Allen, M.R., Dube, O.P., Solecki, W., Aragón-Durand, F., Cramer, W., Humphreys, S., Kainuma, M., Kala, J., Mahowald, N., Mulugetta, Y., Perez, R., Wairiu, M., Zickfeld, K., 2018. Framing and Context. In: Global Warming of 1.5°C. An IPCC Special Report on the impacts of global warming of 1.5°C above pre-industrial levels and related global greenhouse gas emission pathways, in the context of strengthening the global response to the threat of climate change, sustainable development, and effort to eradicate poverty. In press.

Álvarez-Castro, M.C., Faranda, D., Yiou, P., 2018. Atmospheric Dynamics Leading to West European Summer Hot Temperatures Since 1851. Complexity 2018, 1–10. https://doi.org/10.1155/2018/2494509

Anderson, G.B., Bell, M.L., 2011. Heat Waves in the United States: Mortality Risk during Heat Waves and Effect Modification by Heat Wave Characteristics in 43 U.S. Communities. Environ. Health Perspect. 119, 210–218. https://doi.org/10.1289/ehp.1002313

Angélil, O., Perkins-Kirkpatrick, S., Alexander, L. V., Stone, D., Donat, M.G., Wehner, M., Shiogama, H., Ciavarella, A., Christidis, N., 2016. Comparing regional precipitation and temperature extremes in climate model and reanalysis products. Weather Clim. Extrem. 13, 35–43. https://doi.org/10.1016/j.wace.2016.07.001

Bador, M., Terray, L., Boé, J., Somot, S., Alias, A., Gibelin, A.-L., Dubuisson, B., 2017. Future summer mega-heatwave and record-breaking temperatures in a warmer France climate. Environ. Res. Lett. 12, 074025. https://doi.org/10.1088/1748-9326/aa751c

Barriopedro, D., Fischer, E.M., Luterbacher, J., Trigo, R.M., García-Herrera, R., 2011. The hot summer of 2010: redrawing the temperature record map of Europe. Science 332, 220–224. https://doi.org/10.1126/science.1201224

Barriopedro, D., García-Herrera, R., Lupo, A.R., Hernández, E., 2006. A climatology of Northern Hemisphere blocking. J. Clim. 19, 1042–1063. https://doi.org/10.1175/JCLI3678.1

Bromwich, D.H., Wilson, A.B., Bai, L.S., Moore, G.W.K., Bauer, P., 2016. A comparison of the regional Arctic System Reanalysis and the global ERA-Interim Reanalysis for the Arctic. Q. J. R. Meteorol. Soc. 142, 644–658. https://doi.org/10.1002/qj.2527

Cardil, A., Eastaugh, C.S., Molina, D.M., 2015. Extreme temperature conditions and wildland fires in Spain. Theor. Appl. Climatol. 122, 219–228. https://doi.org/10.1007/s00704-014-1295-8

Carmona, R., Linares, C., Ortiz, C., Mirón, I.J., Luna, M.Y., Díaz, J., 2017. Spatial variability in threshold temperatures of heat wave mortality: impact assessment on prevention plans. Int. J. Environ. Health Res. 27, 463–475. https://doi.org/10.1080/09603123.2017.1379056

Cassano, E.N., Cassano, J.J., Seefeldt, M.W., Gutowski, W.J., Glisan, J.M., 2017. Synoptic conditions during summertime temperature extremes in Alaska. Int. J. Climatol. 37, 3694–3713. https://doi.org/10.1002/joc.4949

Cassano, E.N., Lynch, A.H., Cassano, J.J., Koslow, M.R., 2006. Classification of synoptic patterns in the western Arctic associated with extreme events at Barrow, Alaska, USA. Clim. Res. 30, 83–97. https://doi.org/10.3354/cr030083

Cassou, C., Cattiaux, J., 2016. Disruption of the European climate seasonal clock in a warming world. Nat. Clim. Chang. 6, 589–594. https://doi.org/10.1038/nclimate2969

Chan, S.C., Nigam, S., 2009. Residual Diagnosis of Diabatic Heating from ERA-40 and NCEP Reanalyses: Intercomparisons with TRMM. J. Clim. 22, 414–428. https://doi.org/10.1175/2008JCLI2417.1

Chapman, S.C., Watkins, N.W., Stainforth, D.A., 2019. Warming Trends in Summer Heatwaves. Geophys. Res. Lett. 46, 1634–1640. https://doi.org/10.1029/2018GL081004

Chiodo, G., Haimberger, L., 2010. Interannual changes in mass consistent energy budgets from ERA-Interim and satellite data. J. Geophys. Res. 115, D02112. https://doi.org/10.1029/2009jd012049

CLIVAR, 2017. Special Issue on climate over the Iberian Peninsula: an overview of CLIVAR-Spain coordinated science.

Crane, R.G., Hewitson, B.C., 2003. Clustering and upscaling of station precipitation records to regional patterns using self-organizing maps (SOMs). Clim. Res. 25, 95–107. https://doi.org/10.3354/cr025095

Dayon, G., Boé, J., Martin, É., Gailhard, J., 2018. Impacts of climate change on the hydrological cycle over France and associated uncertainties. Comptes Rendus - Geosci. https://doi.org/10.1016/j.crte.2018.03.001

Dee, D., Uppala, S.M., Simmons, A.J., Berrisford, P., Poli, P., Kobayashi, S., Andrae, U., Balmaseda, M.A., Balsamo, G., Bauer, P., Bechtold, P., Beljaars, A.C.M., van de Berg, L., Bidlot, J., Bormann, N., Delsol, C., Dragani, R., Fuentes, M., Geer, A.J., Haimberger, L., Healy, S.B., Hersbach, H., Hólm, E. V., Isaksen, L., Kållberg, P., Köhler, M., Matricardi, M., McNally, A.P., Monge-Sanz, B.M., Morcrette, J.-J., Park, B.-K., Peubey, C., de Rosnay, P., Tavolato, C., Thépaut, J.-N., Vitart, F., 2011. The ERA-Interim reanalysis: configuration and performance of the data assimilation system. Q. J. R. Meteorol. Soc. 137, 553–597. https://doi.org/10.1002/qj.828

Della-Marta, P.M., Luterbacher, J., von Weissenfluh, H., Xoplaki, E., Brunet, M., Wanner, H., 2007. Summer heat waves over western Europe 1880-2003, their relationship to large-scale forcings and predictability. Clim. Dyn. 29, 251–275. https://doi.org/10.1007/s00382-007-0233-1

Díaz, J., Carmona, R., Mirón, I.J., Luna, M.Y., Linares, C., 2018. Time trend in the impact of heat waves on daily mortality in Spain for a period of over thirty years (1983–2013). Environ. Int. 116, 10–17. https://doi.org/10.1016/j.envint.2018.04.001

Diffenbaugh, N.S., Giorgi, F., 2012. Climate change hotspots in the CMIP5 global climate model ensemble. Clim. Change 114, 813–822. https://doi.org/10.1007/s10584-012-0570-x

Diffenbaugh, N.S., Pal, J.S., Giorgi, F., Gao, X., 2007. Heat stress intensification in the Mediterranean climate change hotspot. Geophys. Res. Lett. 34, L11706. https://doi.org/10.1029/2007GL030000

Dole, R., Hoerling, M., Perlwitz, J., Eischeid, J., Pegion, P., Zhang, T., Quan, X.W., Xu, T., Murray, D., 2011. Was there a basis for anticipating the 2010 Russian heat wave? Geophys. Res. Lett. 38, L06702. https://doi.org/10.1029/2010GL046582

Dong, L., Mitra, C., Greer, S., Burt, E., 2018. The Dynamical Linkage of Atmospheric Blocking to Drought, Heatwave and Urban Heat Island in Southeastern US: A Multi-Scale Case Study. Atmosphere (Basel). 9, 33. https://doi.org/10.3390/atmos9010033

Dosio, A., Mentaschi, L., Fischer, E.M., Wyser, K., 2018. Extreme heat waves under 1.5 °C and 2 °C global warming. Environ. Res. Lett. 13, 054006. https://doi.org/10.1088/1748-9326/aab827

Duchez, A., Frajka-Williams, E., Josey, S.A., Evans, D.G., Grist, J.P., Marsh, R., McCarthy, G.D., Sinha, B., Berry, D.I., Hirschi, J.J.M., 2016. Drivers of exceptionally cold North Atlantic Ocean temperatures and their link to the 2015 European heat wave. Environ. Res. Lett. 11, 074004. https://doi.org/10.1088/1748-9326/11/7/074004

Fahad, S., Bajwa, A.A., Nazir, U., Anjum, S.A., Farooq, A., Zohaib, A., Sadia, S., Nasim, W., Adkins, S., Saud, S., Ihsan, M.Z., Alharby, H., Wu, C., Wang, D., Huang, J., 2017. Crop Production under Drought and Heat Stress: Plant Responses and Management Options. Front. Plant Sci. 8, 1147.

https://doi.org/10.3389/fpls.2017.01147

Ferguson, C.R., Villarini, G., 2014. An evaluation of the statistical homogeneity of the Twentieth Century Reanalysis. Clim. Dyn. 42, 2841–2866. https://doi.org/10.1007/s00382-013-1996-1

Fischer, E.M., 2014. Autopsy of two mega-heatwaves. Nat. Geosci. 7, 332–333. https://doi.org/10.1038/ngeo2148

Fischer, E.M., Knutti, R., 2015. Anthropogenic contribution to global occurrence of heavy-precipitation and high-temperature extremes. Nat. Clim. Chang. 5, 560–564. https://doi.org/10.1038/nclimate2617

Fischer, E.M., Schär, C., 2010. Consistent geographical patterns of changes in high-impact European heatwaves. Nat. Geosci. 3, 398–403. https://doi.org/10.1038/ngeo866

Fouillet, A., Rey, G., Laurent, F., Pavillon, G., Bellec, S., Guilhenneue-Jouyaux, C., Clavel, J., Jougla, E., Hémon, D., 2006. Excess mortality related to the August 2003 heat wave in France. Int. Arch. Occup. Environ. Health 80, 16–24. https://doi.org/10.1007/s00420-006-0089-4

Fujiwara, M., Wright, J.S., Manney, G.L., Gray, L.J., Anstey, J., Birner, T., Davis, S., Gerber, E.P., Lynn Harvey, V., Hegglin, M.I., Homeyer, C.R., Knox, J.A., Krüger, K., Lambert, A., Long, C.S., Martineau, P., Molod, A., Monge-Sanz, B.M., Santee, M.L., Tegtmeier, S., Chabrillat, S., Tan, D.G.H., Jackson, D.R., Polavarapu, S., Compo, G.P., Dragani, R., Ebisuzaki, W., Harada, Y., Kobayashi, C., McCarty, W., Onogi, K., Pawson, S., Simmons, A., Wargan, K., Whitaker, J.S., Zou, C.Z., 2017. Introduction to the SPARC Reanalysis Intercomparison Project (S-RIP) and overview of the reanalysis systems. Atmos. Chem. Phys. 17, 1417–1452. https://doi.org/10.5194/acp-17-1417-2017

García-Herrera, R., Barriopedro, D., 2018. Climate of the Mediterranean Region. Oxford Research Encyclopedia of Climate Science. Oxford University Press, USA. https://doi.org/10.1093/acrefore/9780190228620.013.509

Garcia-Herrera, R., Díaz, J., Trigo, R.M., Hernández, E., 2005. Extreme summer temperatures in Iberia: health impacts and associated synoptic conditions. Ann. Geophys. 23, 239-251. https://doi.org/10.5194/angeo-23-239-2005

Garcia-Herrera, R., Díaz, J., Trigo, R.M., Luterbacher, J., Fischer, E.M., 2010. A review of the european summer heat wave of 2003. Crit. Rev. Environ. Sci. Technol. 40, 267–306. https://doi.org/10.1080/10643380802238137

Gaylord, B., Kroeker, K.J., Sunday, J.M., Anderson, K.M., Barry, J.P., Brown, N.E., Connell, S.D., Dupont, S., Fabricius, K.E., Hall-Spencer, J.M., Klinger, T., Milazzo, M., Munday, P.L., Russell, B.D., Sanford, E., Schreiber, S.J., Thiyagarajan, V., Vaughan, M.L.H., Widdicombe, S., Harley, C.D.G., 2015. Ocean acidification through the lens of ecological theory. Ecology 96, 3–15. https://doi.org/10.1890/14-0802.1

Gibbons, J.D., Chakraborti, S., 2014. Nonparametric Statistical Inference, Fourth Edition: Revised and Expanded. Marcel Dekker, New York. ISBN: 9780824786618

Gouveia, C.M., Bistinas, I., Liberato, M.L.R., Bastos, A., Koutsias, N., Trigo, R., 2016. The outstanding synergy between drought, heatwaves and fuel on the 2007 Southern Greece exceptional fire season. Agric. For. Meteorol. 218–219, 135–145. https://doi.org/10.1016/j.agrformet.2015.11.023

Grumm, R.H., 2011. The central European and Russian heat event of July-August 2010. Bull. Am. Meteorol. Soc. 92, 1285–1296. https://doi.org/10.1175/2011BAMS3174.1

Haddeland, I., Heinke, J., Biemans, H., Eisner, S., Flörke, M., Hanasaki, N., Konzmann, M., Ludwig, F., Masaki, Y., Schewe, J., Stacke, T., Tessler, Z.D., Wada, Y., Wisser, D., 2014. Global water resources affected by human interventions and climate change. Proc. Natl. Acad. Sci. U. S. A. 111, 3251–6. https://doi.org/10.1073/pnas.1222475110

Haines, A., Kovats, R.S., Campbell-Lendrum, D., Corvalan, C., 2006. Climate change and human health: Impacts, vulnerability and public health. Public Health 120, 585–596. https://doi.org/10.1016/J.PUHE.2006.01.002

Hanna, E., Cropper, T.E., Hall, R.J., Cappelen, J., 2016. Greenland Blocking Index 1851–2015: a regional climate change signal. Int. J. Climatol. 36, 4847–4861. https://doi.org/10.1002/joc.4673

Hobday, A.J., Alexander, L. V., Perkins, S.E., Smale, D.A., Straub, S.C., Oliver, E.C.J., Benthuysen, J.A., Burrows, M.T., Donat, M.G., Feng, M., Holbrook, N.J., Moore, P.J., Scannell, H.A., Sen Gupta, A., Wernberg, T., 2016. A hierarchical approach to defining marine heatwaves. Prog. Oceanogr. 141, 227–238. https://doi.org/10.1016/j.pocean.2015.12.014

Hodzic, A., Madronich, S., Bohn, B., Massie, S., Menut, L., Wiedinmyer, C., 2007. Wildfire particulate matter in Europe during summer 2003: Meso-scale modeling of smoke emissions, transport and radiative effects. Atmos. Chem. Phys. 7, 4043–4064. https://doi.org/10.5194/acp-7-4043-2007

Hoegh-Guldberg, O., Mumby, P.J., Hooten, A.J., Steneck, R.S., Greenfield, P., Gomez, E., Harvell, C.D., Sale, P.F., Edwards, A.J., Caldeira, K., Knowlton, N., Eakin, C.M., Iglesias-Prieto, R., Muthiga, N., Bradbury, R.H., Dubi, A., Hatziolos, M.E., 2007. Coral reefs under rapid climate change and ocean acidification. Science 318, 1737–1742. https://doi.org/10.1126/science.1152509

Hoinka, K.P., De Castro, M., 2003. The Iberian Peninsula thermal low. Q. J. R. Meteorol. Soc. 129, 1491–1511. https://doi.org/10.1256/qj.01.189

Holbrook, N.J., Scannell, H.A., Sen Gupta, A., Benthuysen, J.A., Feng, M., Oliver, E.C.J., Alexander, L. V., Burrows, M.T., Donat, M.G., Hobday, A.J., Moore, P.J., Perkins-Kirkpatrick, S.E., Smale, D.A., Straub, S.C., Wernberg, T., 2019. A global assessment of marine heatwaves and their drivers. Nat. Commun. 10, 1–13. https://doi.org/10.1038/s41467-019-10206-z

Holton, J.R., Hakim, G.J., 2012. An introduction to dynamic meteorology: Fifth edition. Academic Press. ISBN: 978-0123848666

Horton, D.E., Johnson, N.C., Singh, D., Swain, D.L., Rajaratnam, B., Diffenbaugh, N.S., 2015. Contribution of changes in atmospheric circulation patterns to extreme temperature trends. Nature 522, 465–469. https://doi.org/10.1038/nature14550

Hulbe, C., 2017. Is ice sheet collapse in West Antarctica unstoppable? Science (80-.). 356, 910–911. https://doi.org/10.1126/science.aam9728

Huth, R., Kyselý, J., Pokorná, L., 2000. A GCM Simulation of Heat Waves, Dry Spells, and Their Relationships to Circulation. Clim. Change 46, 29–60. https://doi.org/10.1023/A:1005633925903

Imada, Y., Watanabe, M., Kawase, H., Shiogama, H., Arai, M., 2019. The July 2018 high temperature event in Japan could not have happened without human-induced global warming. Sci. Online Lett. Atmos. 15, 8–12. https://doi.org/10.2151/sola.15A-002

IPCC, 2012. Managing the Risks of Extreme Events and Disasters to Advance Climate Change Adaptation. A Special Report of Working Groups I and II of the Intergovernmental Panel on Climate Change [Field, C.B., V. Barros, T.F. Stocker, D. Qin, D.J. Dokken, K.L. Ebi, M.D, Managing the Risks of Extreme Events and Disasters to Advance Climate Change Adaptation: Special Report of the Intergovernmental Panel on Climate Change. Cambridge University Press, Cambridge, United Kingdom and New York, NY, USA. https://doi.org/10.1017/CBO9781139177245

IPCC, 2013. Climate Change 2013: The Physical Science Basis. Contribution of Working Group I to the Fifth Assessment Report of the Intergovern-mental Panel on Climate Change. Cambridge University Press, Cambridge, United Kingdom and New York, NY, USA.

IPCC, 2014. Fifth Assessment Report of the Intergovernmental Panel on Climate Change. Retrieved from http://www.tandfonline.com/doi/abs/10.4155/cmt.13.80.

Jaiswal, R.K., Lohani, A.K., Tiwari, H.L., 2015. Statistical Analysis for Change Detection and Trend Assessment in Climatological Parameters. Environ. Process. 2, 729–749. https://doi.org/10.1007/s40710-015-0105-3

Jézéquel, A., Yiou, P., Radanovics, S., 2018. Role of circulation in European heatwaves using flow analogues. Clim. Dyn. 50, 1145–1159. https://doi.org/10.1007/s00382-017-3667-0

Kalnay, E., Jenne, R., 1991. Summary of the NMC/NCAR Reanalysis Workshop of April 1991. Bull. Am. Meteorol. Soc. 72, 1897–1904. https://doi.org/10.1175/1520-0477-72.12.1897

Kalnay, E., Kanamitsu, M., Kistler, R., Collins, W., Deaven, D., Gandin, L., Iredell, M., Saha, S., White, G., Woollen, J., Zhu, Y., Chelliah, M., Ebisuzaki W., Higgins, W., Janowiak, J., Mo, K.C., Ropelewski, C., Wang, J., Leetmaa, A., Reynolds, R., Jenne, R., Joseph, D., 1996. The NCEP NCAR 40-Year Reanalysis Project. Bull.

Am. Meteorol. Soc. 77, 437–472. https://doi.org/10.1175/1520-0477(1996)077<0437:TNYRP>2.0.CO;2

Kalvelage, K., Passe, U., Rabideau, S., Takle, E.S., 2014. Changing climate: The effects on energy demand and human comfort. Energy Build. 76, 373–380. https://doi.org/10.1016/J.ENBUILD.2014.03.009

Kohonen, T., 2001. Self-Organizing Maps, Springer Series in Information Sciences. Springer, Berlin, Heidelberg. https://doi.org/10.1007/978-3-642-56927-2

Konovalov, I.B., Beekmann, M., Kuznetsova, I.N., Yurova, A., Zvyagintsev, A.M., 2011. Atmospheric impacts of the 2010 Russian wildfires: Integrating modelling and measurements of an extreme air pollution episode in the Moscow region. Atmos. Chem. Phys. 11, 10031–10056. https://doi.org/10.5194/acp-11-10031-2011

Kovats, R.S., Hajat, S., 2008. Heat Stress and Public Health: A Critical Review. Annu. Rev. Public Health 29, 41–55. https://doi.org/10.1146/annurev.publhealth.29.020907.090843

Lader, R., Bhatt, U.S., Walsh, J.E., Rupp, T.S., Bieniek, P.A., 2016. Two-meter Temperature and Precipitation from Atmospheric Reanalysis Evaluated for Alaska. J. Appl. Meteorol. Climatol. 55, 901–922. https://doi.org/10.1175/JAMC-D-15-0162.1

Lanzante, J.R., 1996. Resistant, robust and non-parametric techniques for the analysis of climate data: Theory and examples, including applications to historical radiosonde station data. Int. J. Climatol. 16, 1197–1226. https://doi.org/10.1002/(SICI)1097-0088(199611)16:11<1197::AID-JOC89>3.0.CO;2-L

Lesk, C., Rowhani, P., Ramankutty, N., 2016. Influence of extreme weather disasters on global crop production. Nature 529, 84–87. https://doi.org/10.1038/nature16467

Lin, Y.K., Maharani, A.T., Chang, F.T., Wang, Y.C., 2019. Mortality and morbidity associated with ambient temperatures in Taiwan. Sci. Total Environ. https://doi.org/10.1016/j.scitotenv.2018.09.161

Meehl, G.A., Tebaldi, C., 2004. More Intense, More Frequent, and Longer Lasting Heat Waves in the 21st Century. Science (80-.). 305, 994–997. https://doi.org/10.1126/science.1098704

Miralles, D.G., Gentine, P., Seneviratne, S.I., Teuling, A.J., 2019. Land–atmospheric feedbacks during droughts and heatwaves: state of the science and current challenges. Ann. N. Y. Acad. Sci. 1436, 19–35. https://doi.org/10.1111/nyas.13912

Miralles, D.G., Teuling, A.J., van Heerwaarden, C.C., Vilà-Guerau de Arellano, J., 2014. Mega-heatwave temperatures due to combined soil desiccation and atmospheric heat accumulation. Nat. Geosci. 7, 345–349. https://doi.org/10.1038/ngeo2141

Mishra, V., Mukherjee, S., Kumar, R., Stone, D.A., 2017. Heat wave exposure in India in current, 1.5 °C, and 2.0 °C worlds. Environ. Res. Lett. 12, 124012. https://doi.org/10.1088/1748-9326/aa9388

Morabito, M., Crisci, A., Messeri, A., Messeri, G., Betti, G., Orlandini, S., Raschi, A., Maracchi, G., 2017. Increasing Heatwave Hazards in the Southeastern European Union Capitals. Atmosphere (Basel). 8, 115. https://doi.org/10.3390/atmos8070115

Naumann, G., Alfieri, L., Wyser, K., Mentaschi, L., Betts, R.A., Carrao, H., Spinoni, J., Vogt, J., Feyen, L., 2018. Global Changes in Drought Conditions Under Different Levels of Warming. Geophys. Res. Lett. 45, 3285–3296. https://doi.org/10.1002/2017GL076521

Nerem, R.S., Beckley, B.D., Fasullo, J.T., Hamlington, B.D., Masters, D., Mitchum, G.T., 2018. Climate-change-driven accelerated sea-level rise detected in the altimeter era. Proc. Natl. Acad. Sci. U. S. A. 115, 2022–2025. https://doi.org/10.1073/pnas.1717312115

Newsham, G.R., Bowker, B.G., 2010. The effect of utility time-varying pricing and load control strategies on residential summer peak electricity use: A review. Energy Policy 38, 3289–3296. https://doi.org/10.1016/J.ENPOL.2010.01.027

Oliver, E.C.J., Donat, M.G., Burrows, M.T., Moore, P.J., Smale, D.A., Alexander, L. V., Benthuysen, J.A., Feng, M., Sen Gupta, A., Hobday, A.J., Holbrook, N.J., Perkins-Kirkpatrick, S.E., Scannell, H.A., Straub, S.C., Wernberg, T., 2018. Longer and more frequent marine heatwaves over the past century. Nat. Commun. 9, 1–12. https://doi.org/10.1038/s41467-018-03732-9

Ordóñez, C., Elguindi, N., Stein, O., Huijnen, V., Flemming, J., Inness, A., Flentje, H., Katragkou, E., Moinat, P., Peuch, V.-H., Segers, A., Thouret, V., Athier, G., van

Weele, M., Zerefos, C.S., Cammas, J.-P., Schultz, M.G., 2010. Global model simulations of air pollution during the 2003 European heat wave. Atmos. Chem. Phys. 10, 789–815. https://doi.org/10.5194/acp-10-789-2010

Parente, J., Pereira, M.G., Amraoui, M., Fischer, E.M., 2018. Heat waves in Portugal: Current regime, changes in future climate and impacts on extreme wildfires. Sci. Total Environ. 631–632, 534–549. https://doi.org/10.1016/J.SCITOTENV.2018.03.044

Park, B.J., Kim, Y.H., Min, S.K., Lim, E.P., 2018. Anthropogenic and Natural Contributions to the Lengthening of the Summer Season in the Northern Hemisphere. J. Clim. 31, 6803–6819. https://doi.org/10.1175/JCLI-D-17-0643.1

Peña-Ortiz, C., Barriopedro, D., García-Herrera, R., 2015. Multidecadal variability of the summer length in Europe. J. Clim. 28, 5375–5388. https://doi.org/10.1175/JCLI-D-14-00429.1

Perkins-Kirkpatrick, S.E., Gibson, P.B., 2017. Changes in regional heatwave characteristics as a function of increasing global temperature. Sci. Rep. 7, 12256. https://doi.org/10.1038/s41598-017-12520-2

Perkins-Kirkpatrick, S.E., White, C.J., Alexander, L. V., Argüeso, D., Boschat, G., Cowan, T., Evans, J.P., Ekström, M., Oliver, E.C.J., Phatak, A., Purich, A., 2016. Natural hazards in Australia: heatwaves. Clim. Change 139, 101–114. https://doi.org/10.1007/s10584-016-1650-0

Perkins, S.E., 2015. A review on the scientific understanding of heatwaves-Their measurement, driving mechanisms, and changes at the global scale. Atmos. Res. 164–165, 242–267. https://doi.org/10.1016/j.atmosres.2015.05.014

Pezza, A.B., van Rensch, P., Cai, W., 2012. Severe heat waves in Southern Australia: synoptic climatology and large scale connections. Clim. Dyn. 38, 209–224. https://doi.org/10.1007/s00382-011-1016-2

Pfahl, S., 2014. Characterising the relationship between weather extremes in Europe and synoptic circulation features. Nat. Hazards Earth Syst. Sci. 14, 1461–1475. https://doi.org/10.5194/nhess-14-1461-2014

Putnam, A.E., Broecker, W.S., 2017. Human-induced changes in the distribution of rainfall. Sci. Adv. 3, e1600871. https://doi.org/10.1126/sciadv.1600871

Ramos, A.M., Trigo, R.M., Santo, F.E., 2011. Evolution of extreme temperatures over Portugal: Recent changes and future scenarios. Clim. Res. 48, 177–192. https://doi.org/10.3354/cr00934

Rasilla, D., Allende, F., Martilli, A., Fernández, F., 2019. Heat Waves and Human Well-Being in Madrid (Spain). Atmosphere (Basel). 10, 288. https://doi.org/10.3390/atmos10050288

Ratnam, J. V., Behera, S.K., Ratna, S.B., Rajeevan, M., Yamagata, T., 2016. Anatomy of Indian heatwaves. Sci. Rep. 6, 24395. https://doi.org/10.1038/srep24395

Reeves, J., Chen, J., Wang, X.L., Lund, R., Lu, Q.Q., 2007. A review and comparison of changepoint detection techniques for climate data. J. Appl. Meteorol. Climatol. 46, 900–915. https://doi.org/10.1175/JAM2493.1

Rodríguez-Puebla, C., Encinas, A.H., García-Casado, L.A., Nieto, S., 2010. Trends in warm days and cold nights over the Iberian Peninsula: Relationships to large-scale variables. Clim. Change 100, 667–684. https://doi.org/10.1007/s10584-009-9721-0

Russo, S., Sillmann, J., Fischer, E.M., 2015. Top ten European heatwaves since 1950 and their occurrence in the coming decades. Environ. Res. Lett. 10, 124003. https://doi.org/10.1088/1748-9326/10/12/124003

Samaniego, L., Thober, S., Kumar, R., Wanders, N., Rakovec, O., Pan, M., Zink, M., Sheffield, J., Wood, E.F., Marx, A., 2018. Anthropogenic warming exacerbates European soil moisture droughts. Nat. Clim. Chang. 8, 421–426. https://doi.org/10.1038/s41558-018-0138-5

Sánchez-Benítez, A., García-Herrera, R., Barriopedro, D., Sousa, P.M., Trigo, R.M., 2018. June 2017: The Earliest European Summer Mega-heatwave of Reanalysis Period. Geophys. Res. Lett. 45, 1955–1962. https://doi.org/10.1002/2018GL077253

Sánchez-Benítez, A., Barriopedro, D., García-Herrera, R., 2019. Tracking Iberian heatwaves from a new perspective. Weather Clim. Extrem. in press.

Schaller, N., Sillmann, J., Anstey, J., Fischer, E.M., Grams, C.M., Russo, S., 2018. Influence of blocking on Northern European and Western Russian heatwaves in large climate model ensembles. Environ. Res. Lett. 13, 054015. https://doi.org/10.1088/1748-9326/aaba55

Schewe, J., Heinke, J., Gerten, D., Haddeland, I., Arnell, N.W., Clark, D.B., Dankers, R., Eisner, S., Fekete, B.M., Colón-González, F.J., Gosling, S.N., Kim, H., Liu, X., Masaki, Y., Portmann, F.T., Satoh, Y., Stacke, T., Tang, Q., Wada, Y., Wisser, D., Albrecht, T., Frieler, K., Piontek, F., Warszawski, L., Kabat, P., 2014. Multimodel assessment of water scarcity under climate change. Proc. Natl. Acad. Sci. U. S. A. 111, 3245–50. https://doi.org/10.1073/pnas.1222460110

Schoetter, R., Cattiaux, J., Douville, H., 2015. Changes of western European heat wave characteristics projected by the CMIP5 ensemble. Clim. Dyn. 45, 1601–1616. https://doi.org/10.1007/s00382-014-2434-8

Scortichini, M., De'Donato, F., De Sario, M., Leone, M., Åström, C., Ballester, F., Basagaña, X., Bobvos, J., Gasparrini, A., Katsouyanni, K., Lanki, T., Menne, B., Pascal, M., Michelozzi, P., 2018. The inter-annual variability of heat-related mortality in nine European cities (1990-2010). Environ. Heal. 17, 1–10. https://doi.org/10.1186/s12940-018-0411-0

Shepherd, T.G., 2016. A Common Framework for Approaches to Extreme Event Attribution. Curr. Clim. Chang. Reports 2, 28–38. https://doi.org/10.1007/s40641-016-0033-y

Sousa, P.M., Barriopedro, D., Ramos, A.M., García-Herrera, R., Espírito-Santo, F., Trigo, R.M., 2019. Saharan air intrusions as a relevant mechanism for Iberian heatwaves: The record breaking events of August 2018 and June 2019. Weather Clim. Extrem. 26, 100224. https://doi.org/10.1016/J.WACE.2019.100224

Sousa, P.M., Trigo, R.M., Barriopedro, D., Soares, P.M.M., Santos, J.A., 2018. European temperature responses to blocking and ridge regional patterns. Clim. Dyn. 50, 457–477. https://doi.org/10.1007/s00382-017-3620-2

Stefanon, M., D'Andrea, F., Drobinski, P., 2012. Heatwave classification over Europe and the Mediterranean region. Environ. Res. Lett. 7, 014023. https://doi.org/10.1088/1748-9326/7/1/014023

Steul, K., Schade, M., Heudorf, U., 2018. Mortality during heatwaves 2003–2015 in Frankfurt-Main – the 2003 heatwave and its implications. Int. J. Hyg. Environ.

Health 221, 81–86. https://doi.org/10.1016/J.IJHEH.2017.10.005

Stott, P.A., Christidis, N., Otto, F.E.L., Sun, Y., Vanderlinden, J.P., van Oldenborgh, G.J., Vautard, R., von Storch, H., Walton, P., Yiou, P., Zwiers, F.W., 2016. Attribution of extreme weather and climate-related events. Wiley Interdiscip. Rev. Clim. Chang. 7, 23–41. https://doi.org/10.1002/wcc.380

Sunday, J.M., Fabricius, K.E., Kroeker, K.J., Anderson, K.M., Brown, N.E., Barry, J.P., Connell, S.D., Dupont, S., Gaylord, B., Hall-Spencer, J.M., Klinger, T., Milazzo, M., Munday, P.L., Russell, B.D., Sanford, E., Thiyagarajan, V., Vaughan, M.L.H., Widdicombe, S., Harley, C.D.G., 2017. Ocean acidification can mediate biodiversity shifts by changing biogenic habitat. Nat. Clim. Chang. 7, 81–85. https://doi.org/10.1038/nclimate3161

Tamarin-Brodsky, T., Hodges, K., Hoskins, B.J., Shepherd, T.G., 2019. A dynamical perspective on atmospheric temperature variability and its response to climate change. J. Clim. 32, 1707–1724. https://doi.org/10.1175/JCLI-D-18-0462.1

Tito, R., Vasconcelos, H.L., Feeley, K.J., 2018. Global climate change increases risk of crop yield losses and food insecurity in the tropical Andes. Glob. Chang. Biol. 24, e592–e602. https://doi.org/10.1111/gcb.13959

Toloo, G., FitzGerald, G., Aitken, P., Verrall, K., Tong, S., 2013. Are heat warning systems effective? Environ. Heal. 12, 27. https://doi.org/10.1186/1476-069X-12-27

Tomczyk, A.M., Półrołniczak, M., Bednorz, E., 2017. Circulation conditions' effect on the occurrence of heatwaves in Western and Southwestern Europe. Atmosphere (Basel). 8, 31. https://doi.org/10.3390/atmos8020031

Torralba, V., Doblas-Reyes, F.J., Gonzalez-Reviriego, N., 2017. Uncertainty in recent near-surface wind speed trends: a global reanalysis intercomparison. Environ. Res. Lett. 12. https://doi.org/10.1088/1748-9326/aa8a58

Trenberth, K., 2011. Changes in precipitation with climate change. Clim. Res. 47, 123–138. https://doi.org/10.3354/cr00953

Trigo, R.M., García-Herrera, R., Díaz, J., Trigo, I.F., Valente, M.A., 2005. How exceptional was the early August 2003 heatwave in France? Geophys. Res. Lett. 32, L10701. https://doi.org/10.1029/2005GL022410

Unkašević, M., Tošić, I., 2009. An analysis of heat waves in Serbia. Glob. Planet. Change 65, 17–26. https://doi.org/10.1016/J.GLOPLACHA.2008.10.009

Vautard, R., Honoré, C., Beekmann, M., Rouil, L., 2005. Simulation of ozone during the August 2003 heat wave and emission control scenarios. Atmos. Environ. 39, 2957–2967. https://doi.org/10.1016/j.atmosenv.2005.01.039

Walpole, R.E., Myers, R.H., Myers, S.L., Ye, K., 2011. Probability & Statistics for Engineers & Scientists. Prentice Hall. ISBN: 978-1292161365

Wilks, D.S., 2011. Statistical methods in the atmospheric sciences, 3rd ed. Academic Press. ISBN: 9780123850225

Willis, M.J., Zheng, W., Durkin, W.J., Pritchard, M.E., Ramage, J.M., Dowdeswell, J.A., Benham, T.J., Bassford, R.P., Stearns, L.A., Glazovsky, A.F., Macheret, Y.Y., Porter, C.C., 2018. Massive destabilization of an Arctic ice cap. Earth Planet. Sci. Lett. 502, 146–155. https://doi.org/10.1016/J.EPSL.2018.08.049

World Meteorological Organization (WMO), 1992. International meteorological vocabulary, 2nd ed.

Wright, J.S., Fueglistaler, S., 2013. Large differences in reanalyses of diabatic heating in the tropical upper troposphere and lower stratosphere. Atmos. Chem. Phys. 13, 9565–9576. https://doi.org/10.5194/acp-13-9565-2013

Yiou, P., Boichu, M., Vautard, R., Vrac, M., Jourdain, S., Garnier, E., Fluteau, F., Menut, L., 2014. Ensemble meteorological reconstruction using circulation analogues of 1781-1785. Clim. Past. https://doi.org/10.5194/cp-10-797-2014

Yiou, P., Jézéquel, A., Naveau, P., Otto, F.E.L., Vautard, R., Vrac, M., 2017. A statistical framework for conditional extreme event attribution. Adv. Stat. Climatol. Meteorol. Oceanogr. 3, 17–31. https://doi.org/10.5194/ascmo-3-17-2017

Yue, S., Pilon, P., Cavadias, G., 2002. Power of the Mann-Kendall and Spearman's rho tests for detecting monotonic trends in hydrological series. J. Hydrol. 259, 254–271.

Zschenderlein, P., Fragkoulidis, G., Fink, A.H., Wirth, V., 2018. Large-scale Rossby wave and synoptic-scale dynamic analyses of the unusually late 2016 heatwave over Europe. Weather 73, 275–283. https://doi.org/10.1002/wea.3278

Appendix

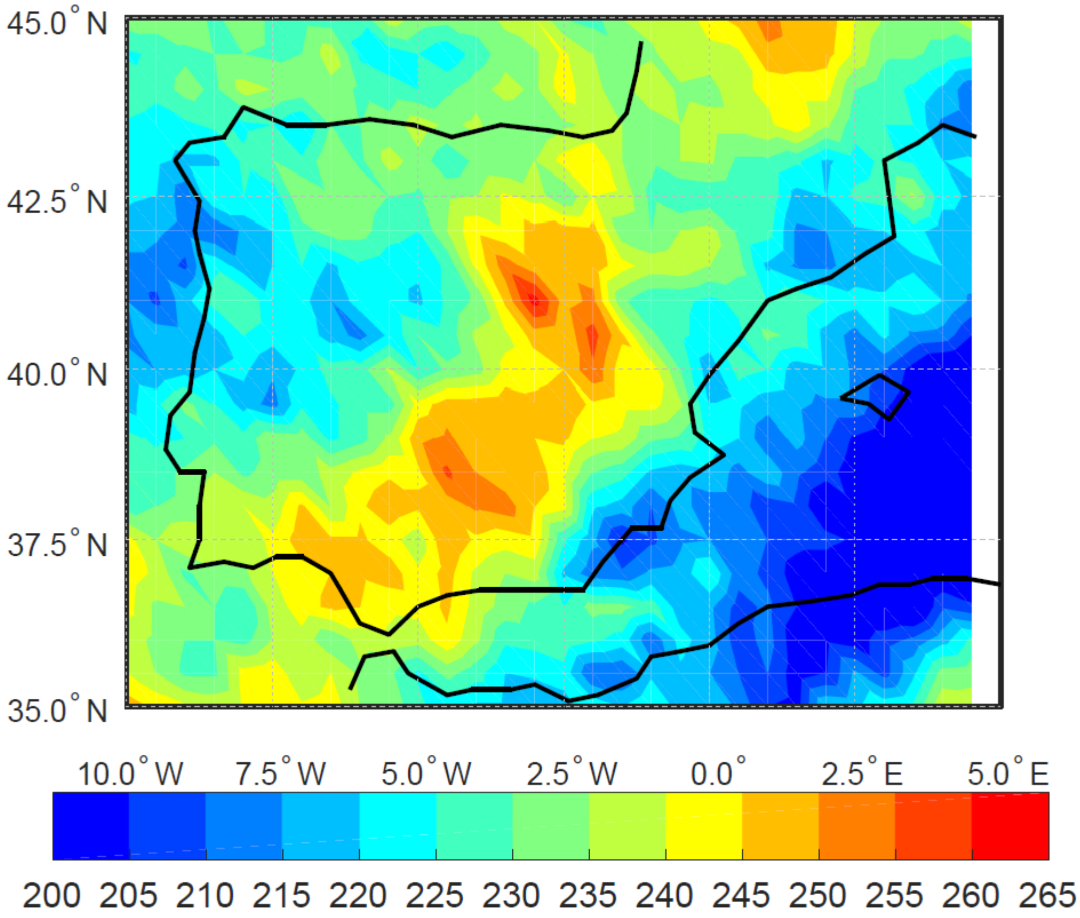

Figure A1. Spatial distribution of exceedances of the 95th Percentile for the ERA-Interim reanalysis in the 1979-2017 period.

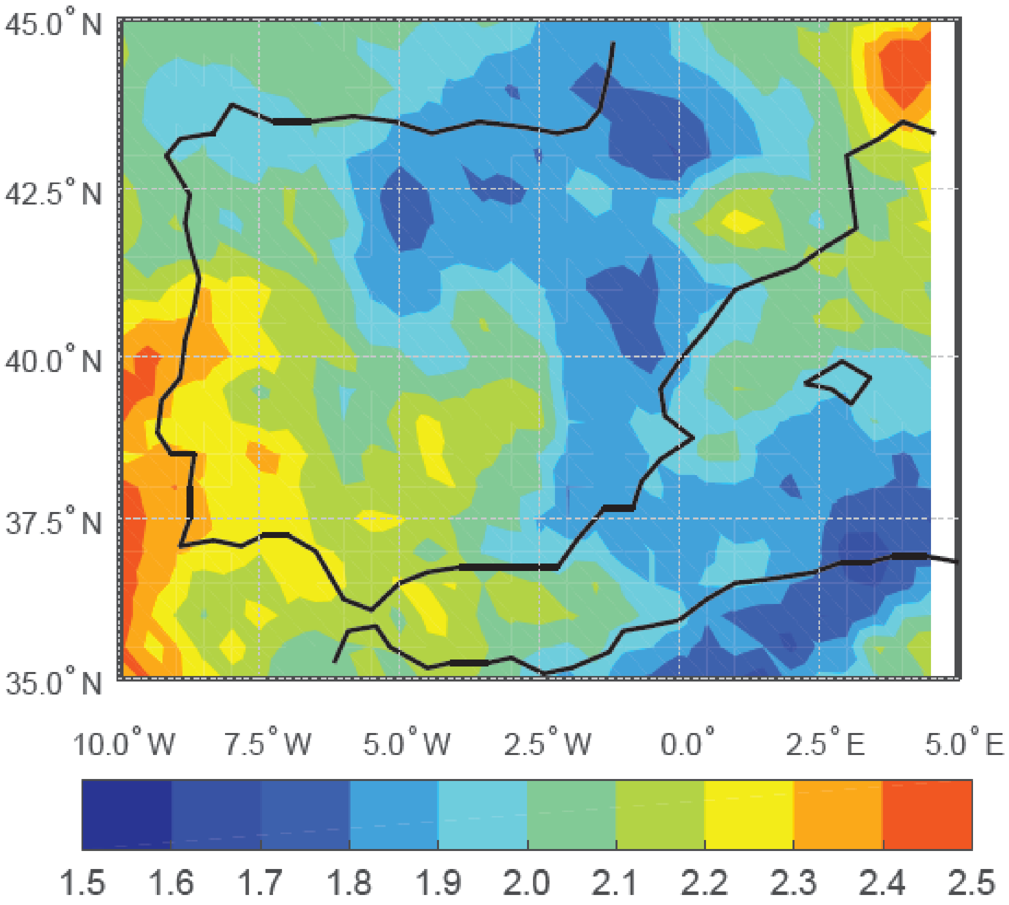

Figure A2. Spatial distribution of mean persistence (in days) of the 95th percentile exceedances. Data were extracted from the ERA-Interim reanalysis in the 1979-2017 period.

Figure A3. Mass centre track for all the Iberian HWEs in the 1979-2017 period. Red/green/blue is used for the pre-Iberian/Iberian/post-Iberian phase, with the transition among different phases in black.

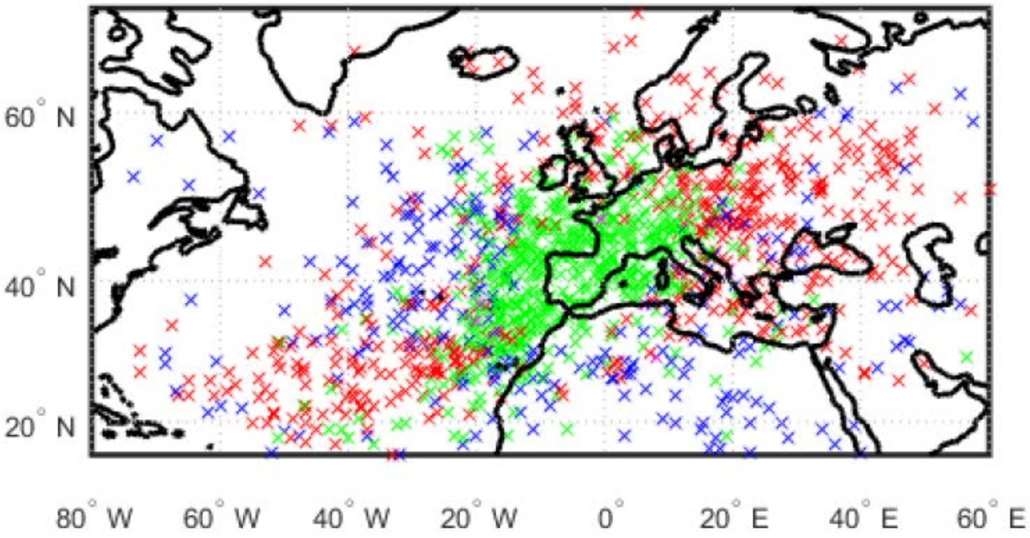

Figure A4. Mass centre location for all the Iberian HWEs in the 1979-2017 period. Red/green/blue is used for the pre-Iberian/Iberian/post-Iberian phase.

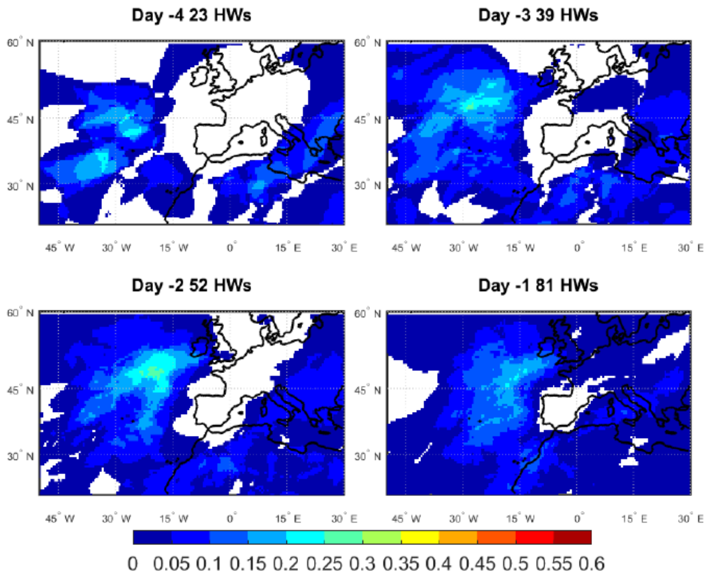

Figure A5. Composite of HWD frequency (shading, with respect to the total days in the step, colourbar) in different steps in the pre-Iberian phase (from 4 days before reaching Iberia (referred as D-4), top left, to the day before affecting it (D-1 from now), bottom right). The title indicates the number of days HWs detected in each step.

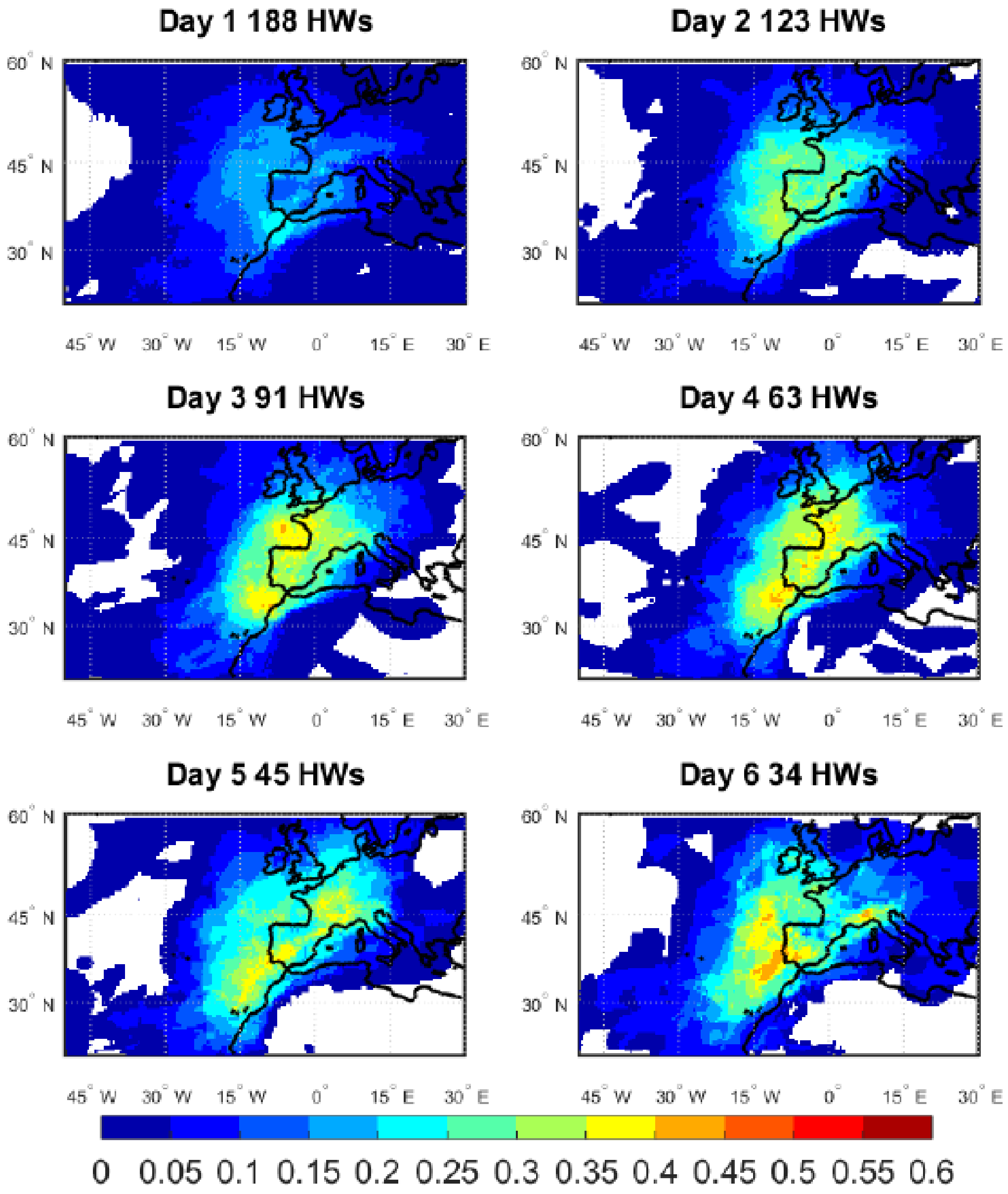

Figure A6. Composite of HWD frequency (shading, with respect to the total days in the step, colourbar) in different steps in the Iberian phase (from the first day (D1 afterward), top left, to the sixth day (referred as D6), bottom right, in Iberia). The title indicates the number of days included in each step.

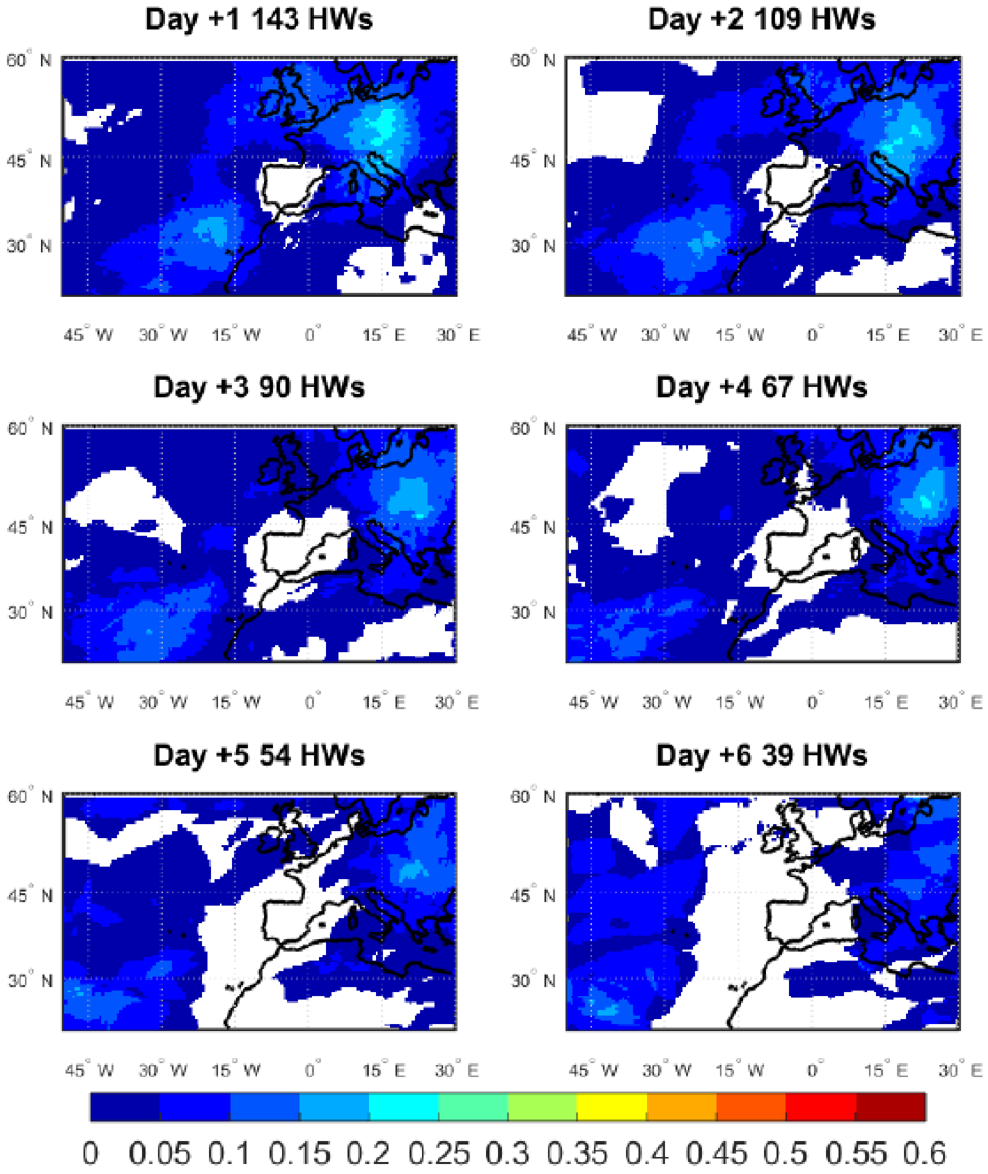

Figure A7. Composite of HWD frequency (shading, with respect to the total days in the step, colourbar) in different steps in the post-Iberian phase (from the first day after leaving Iberia (D+1 from now), top left, to the sixth day (D+6 hereafter), bottom right). The title indicates the number of days included in each step.

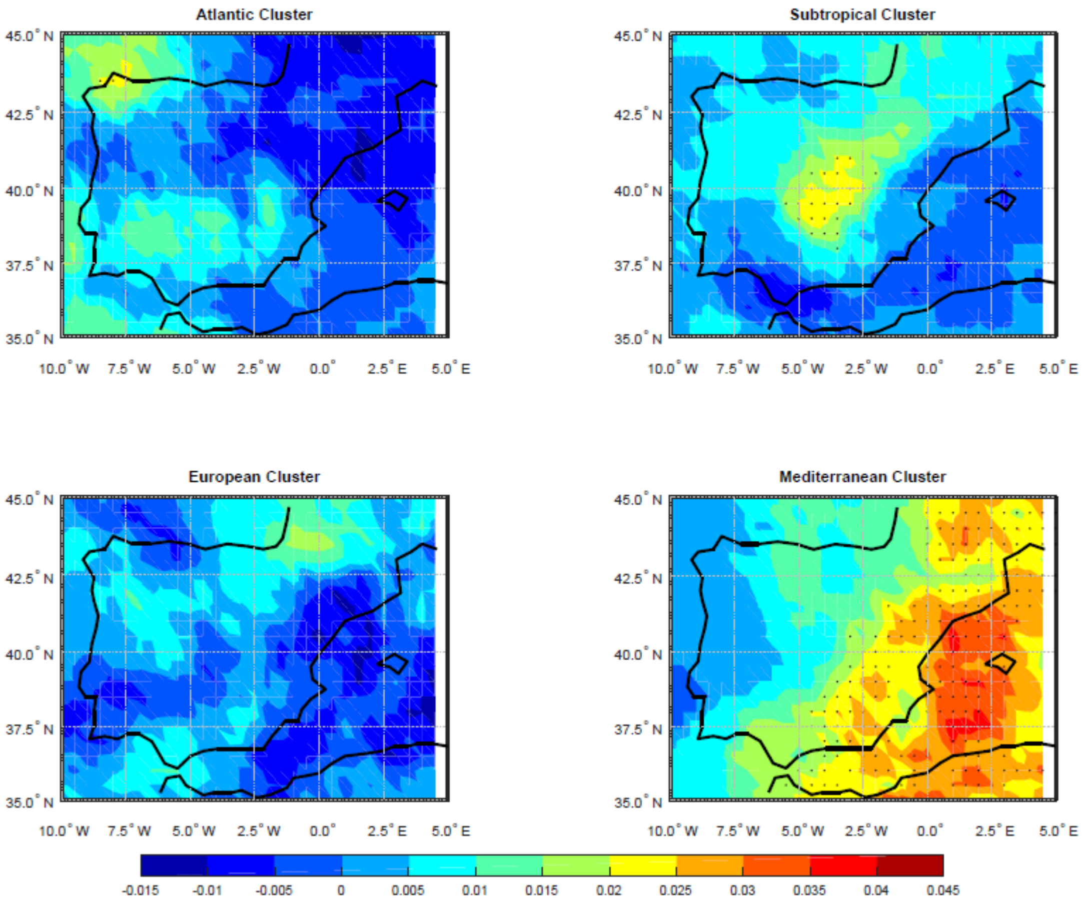

Figure A8. Spatial distribution of HWEs trends for the 1979-2017 period using the ERA-Interim reanalysis for the different SOM-based clusters. The points indicate grid points whose trends are significant at p<0.1 level.

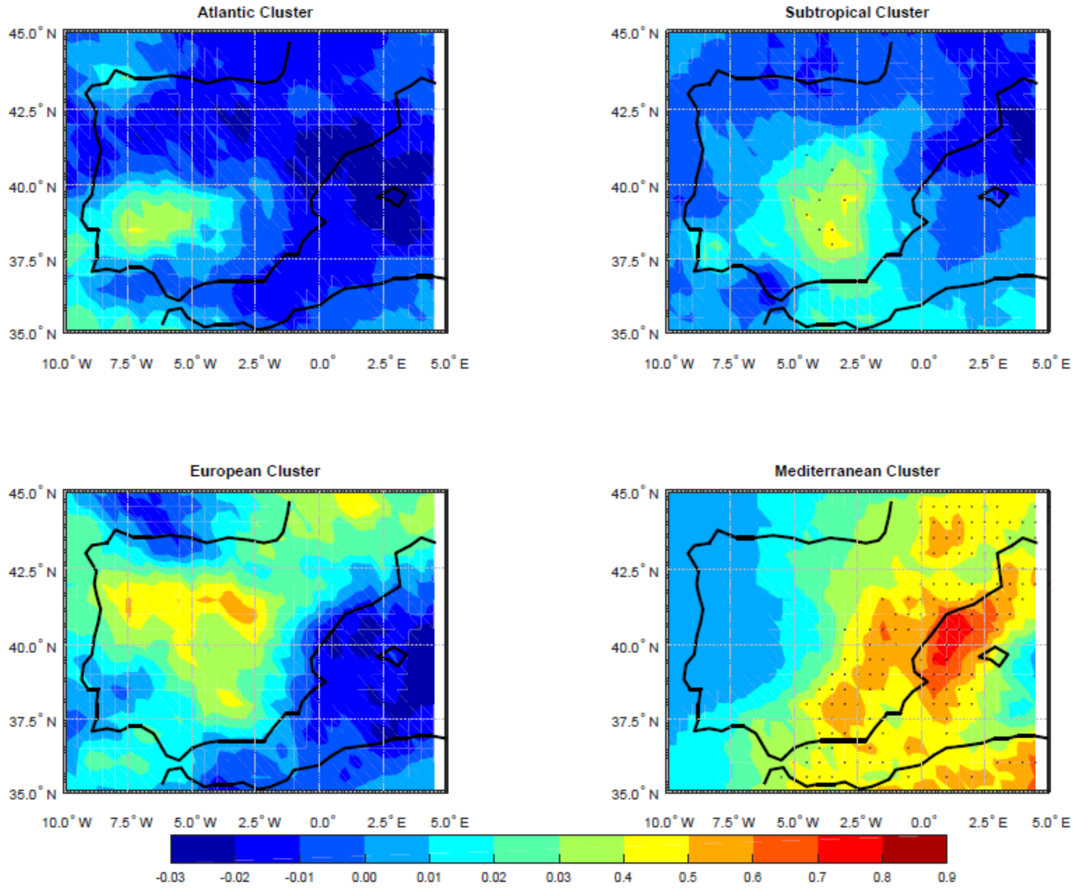

Figure A9. Same as Figure A8 but for Iberian HWDs.

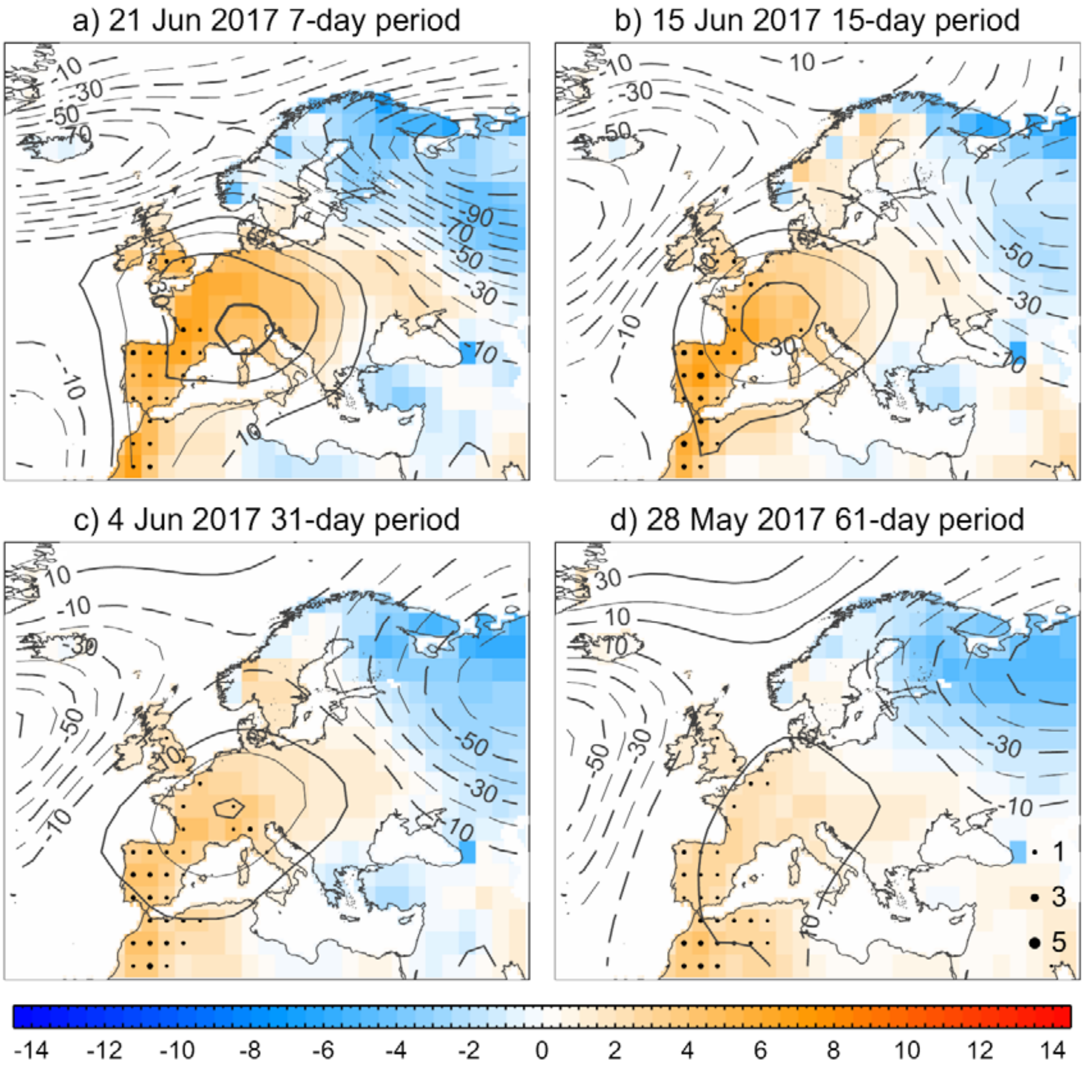

Figure A10**.** Synoptic conditions for the 2017 summer periods when a maximum number of places were simultaneously experiencing record-breaking temperatures at different temporal scales. Shading indicates surface temperatures (ºC) and contours depict Z850 (gpm) anomalies (with reference to the 1981-2010 period), respectively, averaged for: a) 7-day; b) 15-day; c) 31-day; d) 61-day periods centred on the day indicated at the top of each panel. Grid points with record-breaking temperatures are marked with a black point, the size being proportional to the exceedance of the temperature anomaly over the previous maximum (since 1948). Data source is NCEP/NCAR reanalysis for 1948-2017.

Non-Detected days	Non-reached Threshold	Maximum percentile	HW extension (10^4 km^2)
13/07/1975	Temperature	91,7	0
15/07/1978	Extension	98,7	20,75
17/07/1978	Duration	99,9	33,99
11/06/1981	Temperature	89,5	0,00
22/07/1984	Duration	95,7	7,04
18/08/1991	Duration	99,1	20,10
03/08/1991	Duration	97,0	6,76
29/06/1994	Temperature	88,6	0,00
02/07/1994	Temperature	94,5	0,00
21/06/2001	Temperature	93,5	0,00
22/06/2001	Temperature	94,4	0,00
23/06/2001	Temperature	94,3	0,00
24/06/2001	Temperature	93,4	0,00
23/06/2003	Temperature	89,1	0,00
06/08/2005	Duration	99,8	37,24
08/08/2005	Duration	99,6	27,52
29/07/2007	Duration	99,3	23,62
30/07/2007	Duration	98,0	20,29
18/08/2009	Duration	99,1	26,19
19/08/2011	Duration	99,1	36,95
23/08/2012	Duration	99,6	30,48
02/07/2015	Temperature	87,7	0,00
03/07/2015	Temperature	94,8	0,00
16/07/2015	Duration	99,0	29,90
27/07/2016	Extension	97,7	3,43
28/07/2016	Duration	96,8	10,10
18/07/2016	Duration	99,7	19,62
31/07/2018	Temperature	93,0	0,00
01/08/2018	Extension	95,4	3,24
03/08/2018	Duration	99,0	27,52

Table A1. AEMET list HWDs which our detection algorithm fails to detect. Columns indicate (from left to right) the day, non-reached Threshold, highest Iberian temperature (in percentile) and Iberian affected area.

Start Date	Duration (days)	Mean extension (10^6 km^2)	Iberian phase (days)	Mean Iberian affected area (10^5 km^2)	HWMIe	Type of regional Iberian HWE
27/7/1979	4	2,36	4	2,20	517,7	European
27/5/1980	16	1,95	2	1,60	184,0	European
5/8/1980	14	3,64	1	0,17	9,8	Subtropical
18/8/1980	5	2,02	2	6,21	790,4	European
24/8/1980	14	1,43	3	0,74	127,4	Subtropical
4/6/1981	23	3,89	9	3,41	1940,6	Atlantic
12/7/1981	6	1,24	2	0,59	59,8	Atlantic
21/9/1981	4	1,62	1	0,23	13,0	Mediterranean
4/7/1982	7	1,79	5	3,15	1006,3	European
3/9/1982	7	1,13	2	0,07	7,0	Atlantic
14/9/1982	4	1,97	2	0,19	20,6	European
4/6/1983	5	1,15	5	1,45	439,2	European
10/6/1983	10	2,46	8	1,83	837,0	Atlantic
9/7/1983	12	2,02	2	0,12	13,4	European
19/7/1983	14	2,32	11	0,62	441,0	Mediterranean
3/9/1983	10	3,01	4	1,36	308,7	Atlantic
23/9/1983	7	3,58	6	4,72	1826,1	European
9/7/1984	6	1,54	3	1,63	279,1	European
22/8/1985	7	1,84	1	0,75	42,0	Subtropical
4/9/1985	8	2,00	1	1,02	57,8	Atlantic
9/9/1985	4	1,31	4	1,36	307,8	Atlantic
19/9/1985	6	0,89	1	0,11	5,9	Mediterranean
27/9/1985	10	2,73	4	1,13	267,4	European
11/6/1986	4	1,14	1	0,05	2,3	Atlantic
26/6/1986	7	2,34	4	1,47	357,9	European
7/7/1986	5	1,21	4	1,14	240,4	Atlantic
15/7/1986	6	0,84	1	0,04	2,2	Atlantic
20/8/1986	4	1,73	2	1,74	219,5	Subtropical
16/9/1986	4	2,64	2	0,27	32,7	Mediterranean
22/9/1986	8	1,25	1	0,07	4,3	European
24/6/1987	4	1,10	1	0,19	9,3	Atlantic
28/7/1987	21	6,60	6	3,46	1451,5	Atlantic
1/8/1987	4	0,82	2	1,79	199,3	Atlantic
19/8/1987	5	4,75	3	2,71	481,8	European
6/9/1987	19	3,09	18	2,69	3049,4	Subtropical
8/9/1987	21	3,05	1	0,11	6,3	Mediterranean
11/7/1988	6	1,55	3	1,09	197,4	Subtropical

30/7/1988	4	1,68	3	2,31	423,3	Subtropical
17/8/1988	21	2,82	5	1,38	451,9	Subtropical
5/9/1988	11	2,30	6	4,89	2135,8	Atlantic
25/9/1988	6	1,65	5	1,61	488,9	Subtropical
10/7/1989	14	1,87	10	1,56	866,9	Atlantic
28/9/1989	5	2,14	2	1,20	154,2	Atlantic
11/7/1990	5	1,13	3	1,28	218,2	Atlantic
17/7/1990	9	1,22	8	1,98	908,4	Atlantic
2/8/1990	14	2,04	5	1,41	410,4	European
13/7/1991	7	1,38	7	3,07	1278,4	Atlantic
4/8/1991	10	2,05	2	1,51	170,4	Atlantic
25/8/1991	8	1,61	6	1,87	702,5	European
7/8/1992	5	1,45	1	0,66	37,3	Subtropical
18/8/1992	4	0,96	2	2,06	251,3	Mediterranean
26/8/1992	7	2,06	1	0,81	49,0	Subtropical
14/9/1992	5	0,96	5	2,57	758,8	European
25/6/1993	4	1,22	2	0,44	50,3	European
3/7/1993	4	1,20	1	0,11	6,4	Mediterranean
27/5/1994	8	2,37	1	3,11	206,4	European
5/6/1994	6	1,64	3	0,36	57,2	Atlantic
23/6/1994	7	0,84	2	0,43	48,1	European
30/6/1994	13	2,70	7	3,41	1513,4	Subtropical
9/8/1994	10	2,12	5	0,59	175,9	Mediterranean
20/8/1994	5	1,35	4	3,24	841,5	Mediterranean
19/7/1995	9	1,75	7	3,97	1709,7	European
13/8/1995	10	1,30	2	0,30	33,5	Atlantic
6/6/1996	6	1,26	1	0,56	33,5	European
13/6/1996	6	1,80	5	0,96	267,6	Atlantic
12/7/1996	5	1,25	1	0,04	2,3	Atlantic
10/6/1997	13	1,10	3	0,22	36,1	Mediterranean
30/7/1997	11	1,23	1	0,34	18,0	Atlantic
5/9/1997	4	1,26	1	0,05	2,4	European
3/6/1998	22	2,50	1	0,07	4,0	Mediterranean
29/6/1998	7	1,56	1	0,02	1,3	Mediterranean
15/7/1998	9	3,71	2	0,72	71,9	Subtropical
20/7/1998	4	0,96	1	0,48	25,7	Mediterranean
31/7/1998	13	2,91	6	2,40	864,4	Atlantic
20/9/1998	5	1,88	1	0,02	1,2	Atlantic
30/5/1999	7	1,69	1	0,58	34,0	Mediterranean
20/6/1999	8	2,35	1	0,94	48,3	Atlantic
30/6/1999	10	4,60	3	3,83	692,5	Subtropical
4/7/1999	5	1,10	1	0,75	43,0	Mediterranean

8/7/1999	4	2,19	3	2,50	421,0	Atlantic
31/7/1999	16	1,79	1	0,31	16,0	Subtropical
16/8/1999	7	3,65	3	0,03	5,2	Mediterranean
19/9/1999	21	2,15	1	0,09	5,1	Mediterranean
30/5/2000	5	3,17	1	1,61	88,3	Subtropical
14/6/2000	10	1,82	6	0,87	296,1	Atlantic
30/6/2000	13	3,39	2	0,87	102,1	Mediterranean
19/8/2000	11	1,85	5	0,75	237,3	Mediterranean
8/9/2000	4	1,05	3	1,96	336,2	Atlantic
26/5/2001	15	2,79	9	1,14	565,8	Subtropical
20/6/2001	7	1,15	7	3,90	1617,7	European
26/7/2001	7	2,35	2	1,51	183,1	Atlantic
3/6/2002	4	0,73	1	0,32	17,8	European
14/6/2002	8	1,51	6	1,98	664,0	European
9/6/2003	7	1,48	6	2,46	826,8	Mediterranean
18/6/2003	9	1,64	8	1,88	904,4	European
30/6/2003	9	2,58	1	0,16	8,7	Mediterranean
9/7/2003	6	1,06	1	1,37	71,0	Atlantic
13/7/2003	8	2,64	1	0,50	27,7	European
20/7/2003	6	1,11	4	0,53	118,0	Mediterranean
30/7/2003	16	4,10	16	3,29	3223,3	Atlantic
28/8/2003	15	3,05	1	0,09	5,5	Mediterranean
6/9/2003	12	2,04	4	0,45	105,3	Atlantic
18/9/2003	5	1,95	3	0,04	5,7	European
2/6/2004	8	0,78	5	0,57	152,4	Atlantic
12/6/2004	5	1,91	1	0,09	4,6	Atlantic
27/6/2004	12	1,77	4	3,21	751,3	Subtropical
24/7/2004	7	1,18	2	0,56	60,1	Atlantic
8/8/2004	7	3,21	1	0,05	2,3	European
7/9/2004	4	1,08	1	0,04	2,5	European
19/9/2004	9	1,75	3	0,69	122,8	Atlantic
17/6/2005	5	1,57	4	1,23	261,1	European
9/7/2005	9	3,69	3	1,49	247,5	European
19/7/2005	4	2,01	2	0,29	30,1	Atlantic
23/7/2005	9	5,44	1	0,16	8,1	Mediterranean
5/8/2005	4	3,71	4	2,75	693,8	Atlantic
3/9/2005	4	2,19	1	0,52	29,5	European
4/6/2006	11	1,56	4	1,85	421,7	Atlantic
19/6/2006	6	2,07	1	0,07	3,8	Mediterranean
10/7/2006	4	1,28	2	4,09	453,6	European
15/7/2006	9	1,82	5	0,56	148,4	European
25/7/2006	4	1,09	3	0,35	54,1	Mediterranean

28/8/2006	11	2,97	10	2,62	1590,2	Atlantic
21/9/2006	7	2,24	1	0,02	1,1	European
28/7/2007	7	2,56	4	1,22	276,3	Subtropical
13/8/2007	28	2,97	1	0,28	16,5	Mediterranean
27/8/2007	5	1,45	3	2,87	566,7	Mediterranean
6/9/2007	4	2,05	1	0,23	11,9	Atlantic
6/6/2008	18	2,03	1	0,02	1,3	Mediterranean
26/6/2008	5	1,40	4	0,43	90,6	Subtropical
15/8/2008	16	1,97	2	0,11	12,4	European
9/9/2008	6	1,08	2	0,20	25,6	Mediterranean
28/5/2009	6	1,18	2	1,36	140,9	European
20/7/2009	18	3,43	9	1,15	622,2	Subtropical
7/8/2009	9	1,16	3	0,36	62,5	Atlantic
18/8/2009	4	1,27	3	0,81	141,0	Subtropical
30/5/2010	13	4,90	2	2,53	273,7	Atlantic
3/7/2010	17	3,57	1	0,30	15,1	Subtropical
5/7/2010	4	1,66	3	2,22	364,4	Atlantic
10/7/2010	8	2,68	1	0,87	44,5	Subtropical
14/7/2010	32	4,10	1	0,23	12,1	Mediterranean
23/8/2010	15	9,78	7	2,32	1046,3	Subtropical
19/6/2011	10	2,43	1	1,52	80,9	Atlantic
20/8/2011	10	1,64	3	3,07	573,6	Mediterranean
9/9/2011	4	5,92	1	2,32	132,6	Subtropical
10/9/2011	10	1,11	5	1,00	299,1	Mediterranean
28/9/2011	6	3,09	3	0,54	87,8	European
24/6/2012	5	2,97	5	4,28	1375,4	Subtropical
29/6/2012	11	1,17	2	1,25	155,7	Mediterranean
16/7/2012	8	5,90	3	1,12	175,7	Subtropical
31/7/2012	6	1,32	5	1,04	337,8	Mediterranean
5/8/2012	4	1,94	1	0,05	2,7	Mediterranean
17/8/2012	13	1,94	8	3,18	1615,2	Mediterranean
6/9/2012	7	1,28	1	0,22	11,9	Atlantic
12/9/2012	4	1,13	1	1,12	60,7	Atlantic
22/9/2012	12	1,85	2	1,25	149,3	Mediterranean
17/6/2013	6	1,56	1	0,30	17,1	Mediterranean
4/7/2013	12	3,87	7	1,81	725,8	Atlantic
1/8/2013	4	1,49	3	1,09	186,0	European
6/8/2013	4	1,68	1	0,07	3,9	Mediterranean
11/8/2013	12	3,06	5	1,81	528,5	Atlantic
21/9/2013	5	2,24	3	0,89	147,9	European
7/6/2014	5	1,32	4	0,47	110,1	Mediterranean
17/7/2014	16	1,62	3	1,14	188,9	European

27/6/2015	8	1,89	3	4,12	734,8	Atlantic
30/6/2015	14	2,02	10	2,60	1578,9	European
14/7/2015	13	0,91	4	2,55	557,4	Subtropical
6/8/2015	11	1,65	2	2,36	275,7	Mediterranean
28/8/2015	14	2,01	3	0,80	142,9	Mediterranean
30/5/2016	10	4,76	1	1,67	90,5	European
10/6/2016	5	5,18	1	0,87	49,9	Atlantic
11/6/2016	4	2,87	1	0,12	6,9	Subtropical
16/6/2016	12	2,44	2	0,26	28,0	Mediterranean
26/7/2016	4	1,36	1	0,36	18,6	Atlantic
4/8/2016	6	4,86	4	0,70	160,0	Atlantic
15/8/2016	9	2,61	1	0,02	1,2	Atlantic
23/8/2016	7	1,82	5	1,45	424,1	European
4/9/2016	5	2,53	4	5,94	1656,5	European
25/9/2016	5	4,68	1	0,58	35,3	Atlantic
11/6/2017	13	2,14	13	3,77	2901,6	European
5/7/2017	4	0,84	3	0,32	52,6	European
11/7/2017	7	1,65	6	2,82	1056,2	Atlantic
26/7/2017	11	11,30	3	1,15	204,6	Subtropical
30/7/2017	6	3,86	6	0,84	295,8	Mediterranean
3/8/2017	8	4,00	2	1,12	135,0	Mediterranean
8/8/2017	4	4,0147	1	0,22	13,0	Mediterranean
19/8/2017	11	5,7091	2	2,12	257,5	Atlantic
22/8/2017	4	2,1958	3	1,24	214,5	Subtropical
26/8/2017	6	1,1014	3	0,43	75,6	Mediterranean

Table A2. Iberian HWE catalogue. Columns indicate (from left to right) the start dates, total duration (in days), mean extension, Iberian phase (in days), mean Iberian affected area, HWMIe and the type of regional Iberian HWE.